MASTERARBEIT / MASTER'S THESIS

Titel der Masterarbeit / Title of the Master's Thesis

Towards optical levitation of nanoparticles below 10^{-9} mbar

verfasst von / submitted by

Stefan Lindner BSc

angestrebter akademischer Grad / in partial fulfilment of the requirements for the degree of

Master of Science (MSc)

Wien, 2021 / Vienna, 2021

Studienkennzahl lt. Studienblatt / degree programme code as it appears on the student record sheet:	A 066 876
Studienrichtung lt. Studienblatt / degree programme as it appears on the student record sheet:	Master Physik Master's degree programme Physics
Betreut von / Supervisor:	Ass. Prof. Dr. Nikolai Kiesel
Mitbetreut von / Co-Supervisor:	Mario Ciampini PhD

Acknowledgments

I am very glad I decided to ask for an internship in the group of Nikolai Kiesel at the end of my bachelor degree here at the University of Vienna. I am equally I glad was able to stay in the group after my bachelor thesis was done through all of my masters. The continuous work has not only taught me innumerable things on the physics, technology and techniques present in such laboratories but it has also shown me what working as an experimental physicists really entails. There can be low lows when the n-th approach to a problem still yields the same disappointing result and there can be such sweet highs when a long running project finally shows the hoped for results. What has been made especially clear for me over the last three years is that I utterly enjoy it. Having to solve new problems on a daily basis and while doing so inadvertently learning new things is something that I have come to greatly value.

For these reasons and many others I am terribly glad that Nikolai Kiesel has kept me in his group and enabled me to write my master thesis with him. I value Nikolai not only for being the excellent physicist that he is, but also for being an extraordinarily kind and understanding person. Discussions with him always felt on eye level and his ability to ask the unexpected, sometimes inconvenient, but nonetheless always crucial questions at the right time is something that I would like to be able to do at some point in my career.
Next I want to thank Markus Aspelmeyer. His bottomless excitement towards this field of study and physics in general together with his vast knowledge of the topics at hand are probably the reason why I asked for an internship and the end of the first lecture I ever had with him. I am very grateful for the opportunity and the excellent environment he provides to learn about and participate in science.
Especially in the last year and half (having been trying for us all) Mario Ciampini has guided, supported and all together kept me from loosing my marbles at many, many occasions. Thanks for being available as readily as you are whenever I have a dumb question to ask, especially in the context of this thesis. I will never play Hanabi with you again though.
Next I want to deeply thank Jakob Rieser for being in the lab-infantry with me for the better part of the last three years. Thanks for the extremely fun times and bless your piezo-hands.
I thank Paul Juschitz who has fought the good fight with me for the last 6 months in the lab and shares at least one of my vices, which makes the visits to the balcony much more social than they used to be.

Wilfried Philip has been an integral part in the realization of this project and poured hours upon hours of coding and discussions into it. Thank you for your sturdiness throughout. And of course: Maxime, Uros, Lorenzo, Constanze and all the rest of the Aspelmeyer/Kiesel people for knowing so many things and being willing to share them with me through hours of discussion.

Outside the university I cannot thank Viktoria Kraxberger enough. You were the first line of defense for this thesis and the reason why there are any commas in it at all. You know what you are to me. Thank you.
Last but not least I want to thank Bastian Kremser for being the friend he is and I am looking forward to that cheeseburger.

Abstract

Levitated nanoparticles have been established as a promising platform for testing quantum physics on macroscopic scales. In this thesis, initial steps towards a new optical levitation setup were implemented, that will radically improve coherence times of levitated nanoparticles by enabling experiments in extreme ultra-high vacuum to reduce decoherence by gas collisions, and in a standing wave optical trap to minimize decoherence by photon scattering. As briefly outlined here, the experimental design is motivated by an envisioned experiment for matter-wave control with nanoparticles and aims to employ recent achievements in Heiseberg-limited position detection to a standing wave configuration.
To enable the levitation of nanoparticles at sufficiently high vacuum for such experiments, a major focus here is on the extension of the previously demonstrated particle loading through hollow core photonic crystal fibers to below 10^{-9} mbar. This poses two new challenges: On the one hand, previous alignment methods with a preloaded particle cannot be applied, on the other hand particle loading in XUHV cannot rely on friction from the surrounding gas. To address these issues, we have implemented a mobile hollow core fiber based optical trap and demonstrated particle loading at low vacuum using an optical trap that captures the particle when it is near the potential minimum. These solutions already integrated into the ultra-high vacuum chamber of the envisioned experiment and are expected to enable optical manipulation of nanoparticles in XUHV in the near future.

Zusammenfassung

Levitierte Nanopartikel haben sich als neue Plattform für das Testen der Quantenphysik auf makroskopischer Größenordnung etabliert. In dieser Masterarbeit werden die ersten Schritte in Richtung eines neues Levitationsexperiments gesetzt, das die Kohärenzzeit von levitierten Nanoteilchen erhöht. Dies wird bewerkstelligt durch die Verringerung von Dekohärenz durch Kollisionen mit Gasmolekülen und der Verwendung einer optischen Stehwelle zur Minimierung von Dekohärenz durch Streuung von Photonen. Wie kurz beschrieben wird, ist das Design des Experiments motiviert durch ein geplantes Setup zur Kontrolle von Materiewellen mit Nanoteilchen. Um dies zu umzusetzen, ist geplant die kürzlichen Erfolge im Bereich der Heisenberg-limitierten Detektion auf optische Stehwellen zu erweitern.
Um die Levitation von Nanoteilchen bei für derartige Experimente genügend hohem Vakuum zu ermöglichen, besteht der Fokus dieser Arbeit auf die Erweiterung des zuvor gezeigten Teilchen-Ladens durch Hohlfasern auf Drücke unter 10^{-9} mbar. Dies kommt mit zwei neuen Herausforderungen: Auf der einen Seite kann die zuvor verwendete Methode zur Ausrichtung der Hohlfaser, die ein schon geladenes Teilchen in der Falle benötigt

hat, nicht verwendet werden und andererseits kann Teilchen-Laden in extremes Ultrahochvakuum (XUHV) sich nicht auf Luftwiderstand vom umgebenden Gas verlassen. Um diese Probleme zu adressieren, implementieren wir eine neue mobile Hohlfaser-Falle und haben die Übergabe von einem Teilchen in eine optische Falle, die aktiviert wird wenn das Teilchen sich in ihrem Zentrum befindet, in moderaten Vakuumbedingungen gezeigt. Diese Lösungen sind direkt in eine Ultrahochvakuum-Kammer eingebaut und es wird erwartet, dass optische Manipulation von Nanoteilchen in näherer Zukunft bei XUHV-Bedingungen möglich wird.

Contents

List of Figures

List of acronyms

AMU	Atomic mass unit
AOM	Acousto optic modulator
BP	Bright-port
BS	Beam splitter
CCD	Charge coupled device
CNC	Computer numerical control
DM	Dichroic mirror
DP	Dark-port
FG	Frequency generator
FPGA	Field programmable gate array
FR	Faraday rotator
HCF	Hollow core fiber
HCPCF	Hollow core photonic crystal fiber
HV	High vacuum
HWP	Half-wave plate
LC	Loading chamber
LO	Local oscillator
LP	Linear polarized
LV	Low vacuum
MCF	Mode cleaning fiber
MMF	Multi-mode fiber
MSI	Michelson-Sagnac interferometer
MV	Medium vacuum
NA	Numerical aperture
OpAmp	Operational amplifier
PBS	Polarizing beam splitter
POT	Potentiometer
PSD	Power spectral density
QWP	Quarter-wave plate
RF	Radio frequency
SMF	Single-mode fiber
TEM	Transvere electromagnetic mode
TTL	Transistor transistor logic
UHV	Ultra high vacuum
WD	Working distance
XUHV	Extreme ultra high vacuum

Introduction

The advent of quantum mechanics in the early 20th century has introduced the scientific community to concepts such as superpositions and intrinsic uncertainties of observables, deemed strange or impossible in the classical world. These ideas were contained to the atomic and subatomic scales and when Erwin Schrödinger first devised his now famous feline-condemning Gedankenexperiment in 1935 [1], he argued that the theoretical existence of such a macroscopic quantum state displays the absurdity of the prevailing views on quantum mechanics. Since then, the idea of macroscopic objects in distinctly quantum mechanical superpositions has moved from the notepads of theoreticians towards the laboratories of the experimental community.

Kick-started by Davisson and Germa in their 1928 demonstration of electron diffraction on a nickel crystal [2], the field of matter-wave interferometry has since gained much traction and is tackling topics from metrology to questions in fundamental physics. Since the days of Germa the range of particle-masses that can be successfully interfered in such experiments has increased drastically. Pioneering experiments with complex molecules Markus Arndt performed the first matter-wave interference experiments with these objects in 1999 with C_{60} fullerenes [3]. In 2019 his group managed to observe interference fringes for molecules with masses of 10^4 amu in a 2 m long Talbot-Lau interferometer [4]. This constitutes the current mass-record in the field. Going to even larger masses is of great interest to the community as it could enable testing of theories on the quantum gravity interface [5] or further bound modified quantum theories as for instance collapse models [6].

Technological advancements in the control of levitated nanoparticles, together with their excellent isolation from the environment, make these objects strong contenders as a new platform for matter-wave experiments with masses above 10^8 amu. Especially the achievement of motional ground state cooling in an optical cavity [7] and in optical tweezers [8, 9] over the last two years, has enabled the preparation of these nanoparticles into quantum mechanically pure states. Novel and reestablished methods have been employed in proposals that aim for creating massive superpositoins of these nanoparticles [10, 11, 12, 13, 14].

However, the longevity of a quantum state and with it the maximum duration such a matter-wave protocol can take, is directly related to the amount of interaction the object has with its environment. These interactions are classified in decoherence theory [15]. For optically levitated nanoparticles the three main sources of decoherence are: **1)** recoil heating by the trapping beam. **2)** interaction with blackbody photons. **3)** scattering with background gas molecules. The latter immediately localizes any extended quantum

state and can only be reduced by decreasing the pressure at which the experiment takes place. This poses a serious challenge as most currently conducted levitation experiments are limited in pressure by the choice of mechanisms to load particles into the optical trap.

In this thesis we present the first experimental steps targeting interference phenomena with levitated nanoparticles of mass 10^9 amu. The main focus of this work will be put on the development of an updated hollow core photonic crystal fiber loading mechanism [16], that is designed for direct loading of particles into the ultra high vacuum conditions which is a requirement for the interference protocol. This thesis is structured into five chapters:

In the first chapter, we sketch the idea behind an interference experiment with optically controlled nanoparticle matter-waves. The corresponding timescales motivate the experimental setup build in this thesis and the required parameters.
The second chapter provids the necessary theoretical background for the experiment and will discuss topics such as optical forces on Rayleigh particles, feedback cooling as well as our advanced detection method.
The third and fourth chapters present the laboratory actualization of the hollow core fiber loading mechanism into a standing wave optical trap designed minimize decoherence effects.
We conclude by summarizing the main results.

1 Towards matter-wave experiments with levitated nanoparticles

Matter-wave interferometry is a rich branch in the field of quantum optics trying to answer questions as diverse as: does the Schrödinger equation hold for truly macroscopic systems? [17] Can we detect signatures of modified quantum theories as for instance collapse models? [6] Do these massive objects in distinctly quantum mechanical superpositions hint towards theories at the quantum gravity interface? [5]

This chapter will give an overview over the general idea of what constitutes a matter-wave experiment. From there we will outline such an experiment for levitated nanoparticles in a room temperature, tabletop environment. We discuss roadblocks that have to be overcome in order to make this experiment possible, such as the topic of environmental decoherence. Finally we give an outlook on what the work done in the context of this thesis provides for that.

1.1 Matter-wave interferometry

The idea, that similar to massless photons, all particles that are in motion have wavelike properties was born in Louis de Broglies' 1924 thesis [18]. He associates a "de Broglie" wavelength λ_{db} to these objects according to their mass m and velocity v in the following way (h beeing the Plank constant):

$$\lambda_{\mathrm{db}} = \frac{h}{mv} \tag{1}$$

The first experimental confirmation of de Broglies theory was brought by Davisson and Germa in 1928 [2]. In their experiment they fired a beam of slow moving electrons at a nickel crystal observing similar diffraction patterns as prior predicted by Bragg for X-rays. The wavelength calculated from the measured Bragg angles matched excellently with the de Broglie wavelength expected for electrons of the velocities used in the experiment. This constitutes the first laboratory observation of the wave-like nature of matter.
In the following decades wave effects of ever more massive particles were experimentally demonstrated. In 1991 the first successful atom interferometers by Pritchard [19] and shortly after by Kasevich and Chu [20] where reported. In 1999 the group of Anton Zeilinger performed the first matter-wave experiments with complex molecules [3]. They managed to interfere C_{60} fullerenes with a mass of $m = 720\,\mathrm{amu}$ ($1\mathrm{amu} = 1.67 \cdot 10^{-27}\,\mathrm{kg}$) through a nanomechanical diffraction grating. The complexity and mass of the interfered

bodies has since increased ever higher until the year 2019 where the group of Markus Arndt set the to-date mass record by interfering complex molecules of $m = 10^4$ amu in a 2 m long Talbot-Lau interferometer [4].

In the following we will try to break down the working principle of these type of matter-wave experiments to their basic components. While each of these previously mentioned experiments are undeniably more complex and have specialized components to fulfill their intended purpose Fig.(1) depicts a generic idea of such a translatory (particles in motion) matter-wave interferometer (MWI).

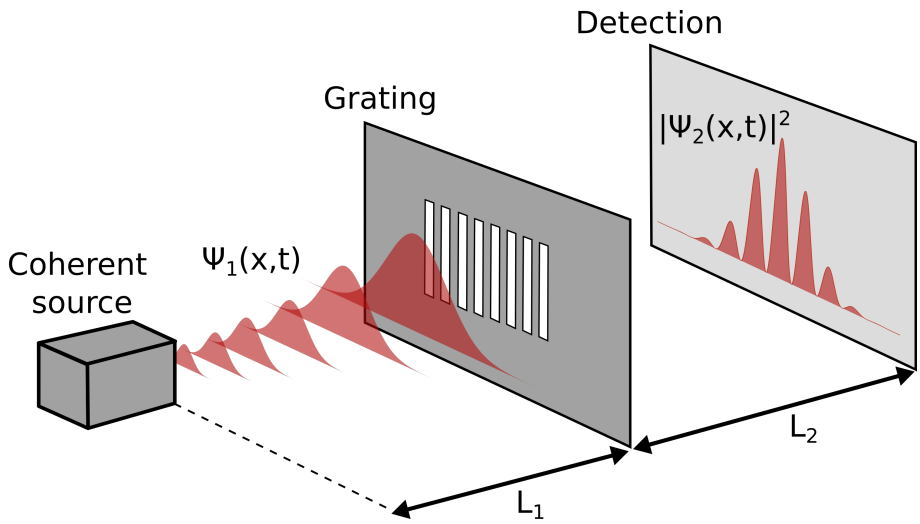

Figure 1: Schematic translatory matter-wave interferometer: A source emits a coherent beam of particles $\psi_1(x,t)$ that evolves and expands over a distance L_1 before being diffracted at an unspecified grating. After a distance L_2 behind this grating where the individual wavelets had time to interfere the interference fringes of the particles are measured at a detection.

In an initial step a coherent beam of particles is created. The wavefunctions $\psi_1(x,t)$ describing the particles in this beam are Gaussian wave packets. These packets expand in width on their way to the grating over a distance L_1, where they have to extends over multiple slits in the grating. This produces at least two localized maxima of the wavefunction with a well defined relative phase propagating forward. Over the distance L_2 these maxima will further expand and overlap creating an interference pattern. In a final step these patterns are measured at a detection of choice in a way that enables the resolution of the individual interference fringes.

Experiments following these broad steps in one way or another have produced the mass record on the observation of wave-like phenomena in matter. By upgrading these experiments further in the direction of improved beam sources, grating refinement and new imaging technology this limit can be raised even higher [4]. These schemes are however not infinitely scaleable and are expected to hit a hard limit towards masses in the order of

$m = 10^9$ amu [21]. To achieve interference of masses in this region or even beyond, other types of interferometers have to be considered.

Optically levitated nanoparticles have been in discussion for use in matter-wave experiments for some time now [10, 11, 12, 13, 14, 22]. The ability to precisely control these objects through manipulation of optical potentials and their excellent decoupling from the environment in high vacuum systems further incentives their usage for such applications. To understand how nanoparticles as comparatively heavy objects can be considered as contenders for matter-wave interferometry we turn to Fig.(2).

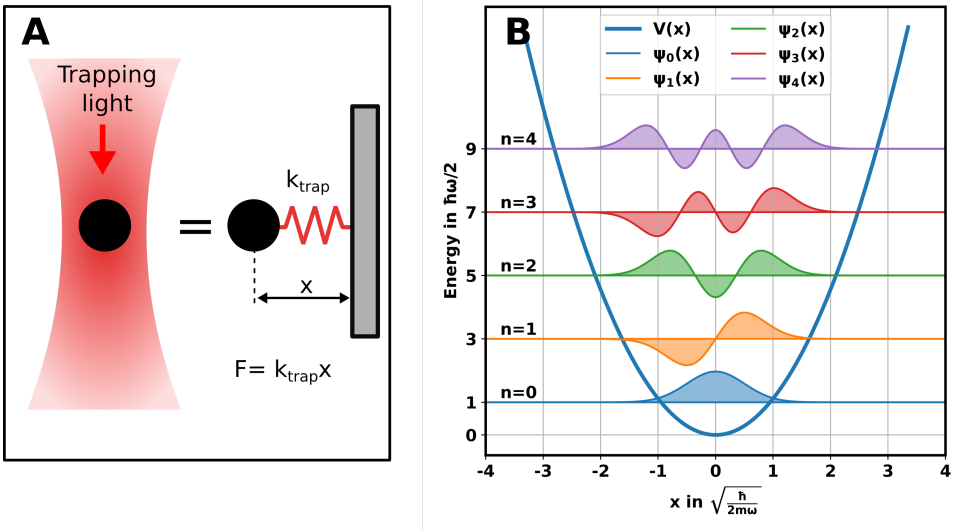

Figure 2: A) Levitated nanoparticles as harmonic oscillators: A dielectric nanoparticle optically trapped in a focused laser beam can be described as harmonic oscillator that experiences a restoring force F proportional to a spring constant k_{trap} and the particles displacement from the trap center x. **B) Quantum harmonic oscillators:** If enough motional energy is removed from such a levitated nanoparticle and it is well enough isolated from its environment it can be treated as quantum harmonic oscillator with discrete energy levels separated by the the energy $\hbar\omega$, where ω is the frequency of the oscillator. For each of the five depicted energylevels the corresponding wavefunctions ψ_n are shown. The distances on the x-axis is given in the oscillators zero point fluctuation $x_{\text{zpf}} = \sqrt{\frac{\hbar}{2m\omega}}$.

The left side of Fig.(2A) schematically depicts a dielectric nanoparticle confined in an optical trap formed by a focused light beam. For small displacements from the trap center, this system can be approximated as a harmonic oscillator with a spring constant k_{trap} proportional to the power of the trapping light and the mass of the oscillator m. If enough motional energy of this confined particle is removed through a feedback cooling mechanism, it can be treated as a quantum mechanical harmonic oscillator. The blue curve in Fig.(2B) shows the harmonic potential $V(x)$ created by the trapping laser the particle is confined in. A quantum harmonic oscillator has discrete energy levels separated by an

energy of $\hbar\omega$ where ω is the oscillation frequency of the particle in the trap. For the lowest five of these discrete energy states the corresponding wavefunctions ψ_n are depicted in Fig.(2B). Removing all the possible motional energy from this oscillator will prepare this particle in its groundstate ($n = 0$). The wavefunction describing a particle in this state is Gaussian and preparing a particle in this lowest energy state is a prerequisite for almost every proposed matter-wave interferometry scheme involving levitated nanoparticles [10, 14, 22].

The steps to observe matter-wave interference for nanoparticles have certain similarities to the generic matter-wave interferometer depicted in Fig.(1). After the initial state preparation the particle is released from its confining potential to make its wavepacket extension expand during a free evolution. After this free evolution the particle wavefunction interacts with some sort of non-linearity, e.g. an ultraviolet standing wave phase grating [22] or a x^2 measurement in a cavity [5] to create at least two spatially separated intensity maxima. After another free evolution the resulting fringes of the wavefunction are detected in a final step of the interferometer.

The important first step of preparing these nanoparticles into their motional groundstate has recently been achieved in three separate experiments [7, 8, 9] paving the way towards the realization of these matter-waves experiments. However currently envisioned proposals for these protocols rely on several hard to implement processes such as a big expansion of the wavepacket [11] or strong interactions [14] in addition to them being conceived for cryogenic temperatures.

In the next section we will briefly outline the idea of a matter-wave protocol that can be conducted at room temperature in a tabletop environment.

1.2 Optical micromanipulation for matter-wave interferometry

Over the last 18 months or so, a radically new approach to perform wavepacket control with levitated nanoparticles in non-linear potentials has been developed by our research group and fully worked out by Lukas Neumaier [23]. While the details of the envisioned scheme are outside of the scope of this thesis, we outline the general idea together with some experimental parameters as they give rise to environmental boundary conditions needing to be met in order to successfully control the wavepackets of these massive objects.

The protocol is designed for levitated silica nanoparticles in with a mass of $m = 10^9$ amu that are trapped in an $\lambda = 1550\,\mathrm{nm}$ optical standing wave. The scheme consists of three distinct steps separated by two times of free evolution, similar to the generic MWI depicted in Fig.(1).

In an initial step the particle is cooled close to its motional groundstate as done in [8]. Having reached this quantum mechanically pure and coherent state of the oscillator the first free fall time begins where the particles confining optical potential is turned off. During this free fall the wavepacket of the oscillator will increase in width. At the end of this free evolution the second step of the protocol in the form of the activation of a non-linear optical potential is instigated. The particle interacts with this potential for a short period of time compared to the timescales of the wavefunction dynamics ($\sim 5\,\mu\mathrm{s}$). This interaction creates fringes in the particles wavefunction in momentum space, similar to how a Gaussian wavepacket displays fringes upon reflection on a barrier from its forward and backward moving components interfering (see Fig.(3)). In the following free fall these fringes are mapped from momentum space into position space where they are detected through an instantaneous readout of the particle position through the trapping beam.

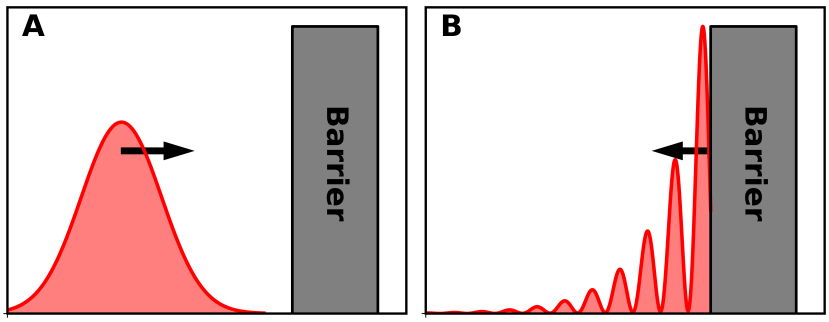

Figure 3: A) Wave packet reflected on a barrier: A right moving Gaussian wave packet approaches an impassable barrier. **B)** The front part of the wave packet is reflected and moves to the left while the back part is still moving towards the right. This makes the wavepacket interfere with itself and gives rise to fringes. In a similar manner the wave packet in the matter-wave protocol creates fringes from interacting with the non-linear potential.

A single protocol takes $\sim 20\,\mathrm{ms}$ from the first free fall time to the final detection of the particle and in order to resolve the fringes of the interference pattern the protocol will be performed several thousand times in one go. From the performed simulations a spacing between the fringes of the interference pattern of $> 0.1\,\mathrm{nm}$ is to be expected. This, together with the requirement of ground state cooling gives rise for the need of a very sensitive position detection of the particle.

The success of this proposed experiment heavily relies on the nanoparticle being able to freely evolve without any coherence destroying interaction during the whole $\sim 20\,\mathrm{ms}$ of the protocol. In order to quantify this in the form of bounds on experimental parameters the next chapter takes a brief look at theory of decoherence for levitated nanoparticles in the context of this matter-wave experiment.

1.3 Challenges and decoherence theory

For a levitated nanoparticle like the one envisioned for the experiment the dominant source of decoherence is the localization of the wavepacket through the photon recoil of the trapping beam [24, 25]. This is not an issue for the two periods of free fall as the particle does not interact with the trapping beam there, but it limits the time the particle can interact with the non-linear potential. The number of coherent oscillations a particle in an optical trap can perform takes the following form [26]:

$$N_{\mathrm{coh}} = \frac{5}{8\pi^3} \frac{\varepsilon + 2}{\varepsilon - 1} \frac{\lambda^3}{V} \tag{2}$$

Here ε is the particle polarizability, λ the wavelength of the trapping laser and V the volume of the particle. From this relation we see that the longer the wavelength, the more coherent oscillations are possible. By choosing $\lambda = 1550\,\mathrm{nm}$ we balance the need for a big N_{coh} with the availability of low intensity noise lasers. For this wavelength, a typical particle radius of $a = 71\,\mathrm{nm}$ and a particle polarizability of $\varepsilon = 2.1$ we get $N_{\mathrm{coh}} = 186$ for the number of coherent oscillations. The oscillation frequency of the particle in any optical potential is dependent on the optical power P of the beam creating the potential. This power P has to be chosen in such a way that the number of oscillations the particle performs during the interaction time of $\sim 5\,\mu\mathrm{s}$ is well below the number of coherent oscillations N_{coh}.

In addition to the decoherence due to photon recoil there are other, unavoidable forms of interactions that limit the eventual lifetime of any quantum state and set the environmental boundary conditions for the success of the experiment.
In the theory of environmental decoherence first introduced by Joos and Zed in 1985 [15], interactions with the environment are classified in two limiting cases: the short and long wavelength limit. These limits refer to the (de Broglie-) wavelength of the particles interacting with the quantum state in question. In the long wavelength limit the extension of the quantum state is much smaller than the wavelength of the interacting particle. Interactions of this type do not resolve the particle position perfectly, thus do not destroy the quantum state after a single event and usually describe interactions with thermal blackbody photons. Interactions in the short wavelength limit on the other hand happen with particles of wavelengths smaller than the extension of the wave-packet. These scattering events fully resolve the position of the object, lead to a loss coherence and destroy the quantum state. The scattering of gas molecules falls into this category. Here we will mostly discuss this latter case as these exchanges immediately disable the further manipulation of the quantum state.

This entails, that for most experimental runs no gas molecule is allowed to directly scatter on our evolving wave packet. The most straight forward way to suppress these interactions is to reduce the background pressure in the volume the experiment is conducted. To further quantify this, we take a look at the frequency of collision with background gas molecules, as this gives the maximal amount of time a particle has for a coherent evolution. From kinematic gas theory we get the mean free path Λ_{free} of the particle as [27]:

$$\Lambda_{\text{free}} = \frac{1}{4\sqrt{2}\pi}\frac{k_b T}{P a^2} \tag{3}$$

Here k_b is the Boltzmann constant, T the temperature of the gas and P the gas pressure. The average background gas velocity for a Boltzmann distributed gas reads $\tilde{v}_{\text{gas}} = \sqrt{\frac{2k_b T}{m_{\text{gas}}}}$ where m_{gas} is the mass of the background gas molecules. The scattering rate f_s is then given by the ratio of the mean free path and this velocity.

$$f_s = \frac{8\pi a^2 P}{\sqrt{k_b T m}} \tag{4}$$

Fig.(4) depicts the mean free time between two collisions of the nanoparticle with a gas molecule in different pressure regime.

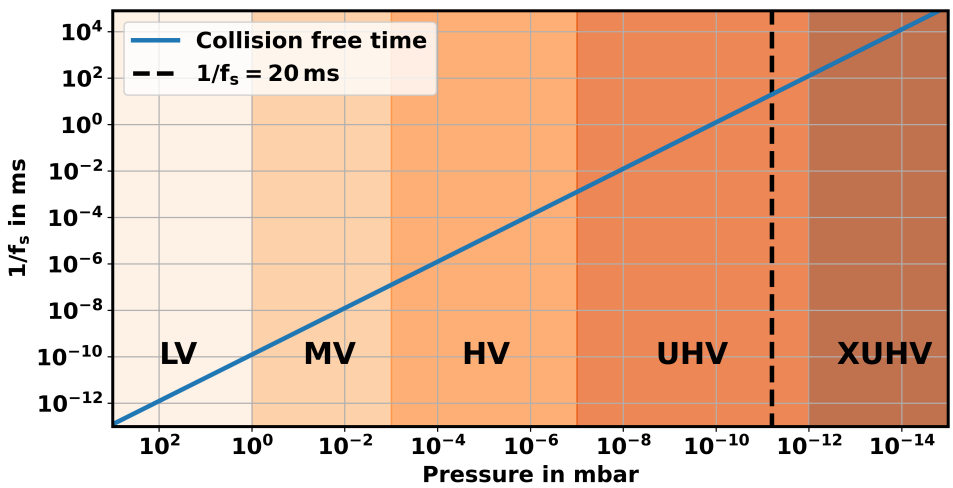

Figure 4: Mean free time of a nanoparticle: The blue line indicates the mean free time a levitated nanoparticle displays for varying gas pressures at an environmental temperature of $T = 300\,\text{K}$ and a particle radius of $a = 71\,\text{nm}$. The black dashed line displays the pressure required for a 20 ms collision free time, as required in the experiment described above. The differently colored regions show different pressure regimes defined as follows. Atmosphere down to 1 mbar: low vacuum (LV), 1 mbar to 10^{-3} mbar: medium vacuum (MV), $10^{-3} - 10^{-7}$ mbar: high vacuum (HV), below $10^{-7} - 10^{-12}$ mbar: ultra high vacuum (UHV) and below 10^{-12} mbar: extreme ultra high vacuum (XUHV) [27].

From this figure one can deduce that in order to be able to perform the proposed 20 ms long protocol we have to achieve levitation at pressures of around $p = 10^{-11}$ mbar, well within the ultra high vacuum (UHV) regime. In and of itself reaching these vacuum levels is possible with the correct choice of vacuum pumps, as for instance a combination of molecular turbo pumps, ion and non evaporative getter pumps (as in [28]) can, under optimal conditions, reach pressures down to 10^{-14} mbar. Getting particles into traps that reside at these very low pressures is on the other hand very challenging and has not been achieved yet.

1.4 Optical trapping in UHV

Since the first optical levitation experiments in vacuum performed by Ashkin in the 1970s [29, 30] technological advancements pushed the boundaries of achievable pressures for these types of experiments. Especially the first implementations of motional control of levitated nanoparticles in the Rayleigh regime [31, 32] have contributed to this. Previous to these feedback mechanisms the loss of particles for pressures $\ll 1\,\mathrm{mbar}$ was observed. Since then, many groups have conducted levitation experiments achieving UHV conditions at pressures of 10^{-7} to high 10^{-9} mbar [25, 33, 34, 35]. Looking back at Fig.(4) this translates into free-fall times between 1 and $100\,\mu$s.
The main obstacle preventing the achievement of lower pressures, and therefore longer undisturbed free fall times, is the contamination of the vacuum chamber walls, introduced by the particle loading mechanism. The contaminants on the inner surfaces of the chamber lead to an increased gas load and are not removable by the vacuum pumps.

The most commonly used method to load particles into optical traps, first implemented in [36] and since used in numerous experiments [7, 8, 9, 33, 34, 37] is to capture particles made airborne through an ultrasonic nebulizer. The sonicated particles are directed towards the vacuum chamber where they per chance fall into the optical trap. While easily implementable and very reliable, this method has several shortcomings in combination with UHV experiments.
As mentioned above, the base pressure of a vacuum system can be severely impacted by the cleanliness of the chamber in use. The aqueous particle solution in the nebulizer, together with the alcohol its diluted in, cover the inside of the vacuum chamber at each loading attempt. Baking the chamber at temperatures above 70° C would remove this material, but is impractical to impossible in practice, as this would entail a baking process after each particle loading instance. Another issue with the nebulizer loading scheme is that the successful trapping of particles for this method can only occur at low vacuum conditions, where the drag force exerted by the background gas on the particle is still high enough to slow the nanoparticles upon entering the trap. This means whenever there is need for a new particle the whole vacuum system has to be brought up to pressures close to atmosphere. If they are even still reachable, the subsequent pump-down can take up to days in time, to go down to base pressures in the UHV regime.

For these reasons, scientific groups around the world have been developing alternative schemes for loading particles into optical (and electrical) traps [38, 39, 40]. For more

details on these methods see [16].

In order to enable levitation in a pressure regime below 10^{-9} mbar we pursue the implementation of a loading mechanism using hollow core fibers (HCF). With it the chamber containing the optical trap is kept clean and at high vacuum conditions. This chamber is connected to a secondary chamber through a HCF. A light standing wave consisting of two counterpropagating laser beams through this fiber turns it into an optical conveyor belt that guides particles from the second (loading-) chamber to the primary chamber and directly into the optical trap. In his master thesis Jakob Rieser demonstrated the successful handover of levitated nanoparticles into an optical trap at pressures in the millibar regime [16]. I participated in these efforts as an intern and with this master thesis, I develop and introduce the technology to enable loading at 10^{-9} mbar based on HCF.

1.5 The experimental scope of this thesis

The experimental work done for this thesis is separated into two (partially interconnected) parts:
The initial part concerns the first steps towards an experimental implementation of the discussed protocol for matter-wave interference. This entails setting up an optical standing wave trap for dielectric nanoparticles in an UHV compatible vacuum chamber. A detection scheme for particles in this standing wave is implemented that has to meet two requirements: first, a high enough sensitivity to resolve the sub-nanometer spacing of the expected matter-wave fringes and second, a high enough collection efficiency of light scattered by particle to enable groundstate cooling. Finally two different feedback cooling methods, namely parametric feedback cooling and linear electric feedback cooling are set up, one for pre-cooling the particle motion in order to prevent particle loss at low pressure and the other one to actually cool the particle motion into its quantum groundstate.

The second part of the experimental work focuses on the improvement and UHV extension of the HCF loading mechanism. Specifically two big updates have to be made. The current method to align the HCF to the the optical trap, while accurate, is not UHV compatible. A new alignment procedure involving co-moving piezostages is devised, which does not impact the base pressure reachable by the vacuum system. The second update concerns the conception, testing and addition of an electronic triggering mechanism required for particle handovers from the hollow core fiber to the optical trap at pressures below the viscous flow regime.

2 Optics, optical forces and optomechanics

The goal of this work is to enable optical levitation of nanoparticles at pressures well within the UHV regime. To achieve this, a hollow core fiber assisted loading scheme is implemented. In this section a theoretical toolbox necessary for the understanding of the following chapters is presented.
Starting off with Gaussian optics and the optical forces making levitation of nanoparticles possible, this section will also outline the general dynamics of these particles. The last two sections will elaborate on the idea of feedback cooling and the enhanced particle detection scheme developed for this work.

2.1 Gaussian optics

The optical traps used to confine and control the dielectric nanoparticles in this work are created by the focusing of continuous wavelength laser beams. Most lasers including the ones used for this experiment, emit a fundamental transverse Gaussian (TEM00) mode. The following section will elaborate on the principles and properties of single sided Gaussian beams at first and subsequently on Gaussian beam standing waves.

Single sided Gaussian beams

The Gaussian beam is a special solution of the paraxial Helmholtz equation and takes the following form:

$$E(\boldsymbol{r}) = E_0 \frac{\omega_0}{\omega(z)} \exp\left[\frac{-r^2}{\omega(z)^2}\right] \exp\left[-ik\frac{r^2}{2R(z)}\right] \exp\left[-i\left(kz + \zeta(z)\right)\right] \tag{5}$$

With the terms from Eq.(6-9) making up the Gaussian beam parameters, r the radial coordinate, z the axial, $k = 2\pi/\lambda$ the wavevector, λ the wavelength and E_0 the beams constant field vector.

$$\omega(z) = \omega_0 \sqrt{1 + \left(\frac{z}{z_R}\right)^2} \qquad \text{Beam radius as distance z from } \omega_0 \tag{6}$$

$$R(z) = z\left(1 + \left(\frac{z_R}{z}\right)^2\right) \qquad \text{Wavefront curvature} \tag{7}$$

$$\zeta(z) = \arctan\left(\frac{z}{z_R}\right) \qquad \text{Gouy phase} \tag{8}$$

$$z_R = \frac{\pi\omega_0^2}{\lambda} \qquad \text{Rayleigh length} \tag{9}$$

$$\tag{10}$$

Here ω_0 is the smallest beam radius also called the waist and the Rayleigh length z_R denotes the axial position at which the beam waist ω_0 has increased by a factor of $\sqrt{2}$. The time averaged intensity of the Gaussian beam reads:

$$I(\boldsymbol{r}) = \frac{2P}{\pi\omega^2(z)} \exp\left(\frac{-2r^2}{\omega^2(z)}\right) \tag{11}$$

Here $P = \int dx\, dy I = \frac{1}{4} c\varepsilon_0 \pi \omega_0^2 E_0^2$ is the optical power of the beam [41]. Fig.(5) depicts the 2D-Intensity distribution of a single sided Gaussian beam propagating along the z-direction.

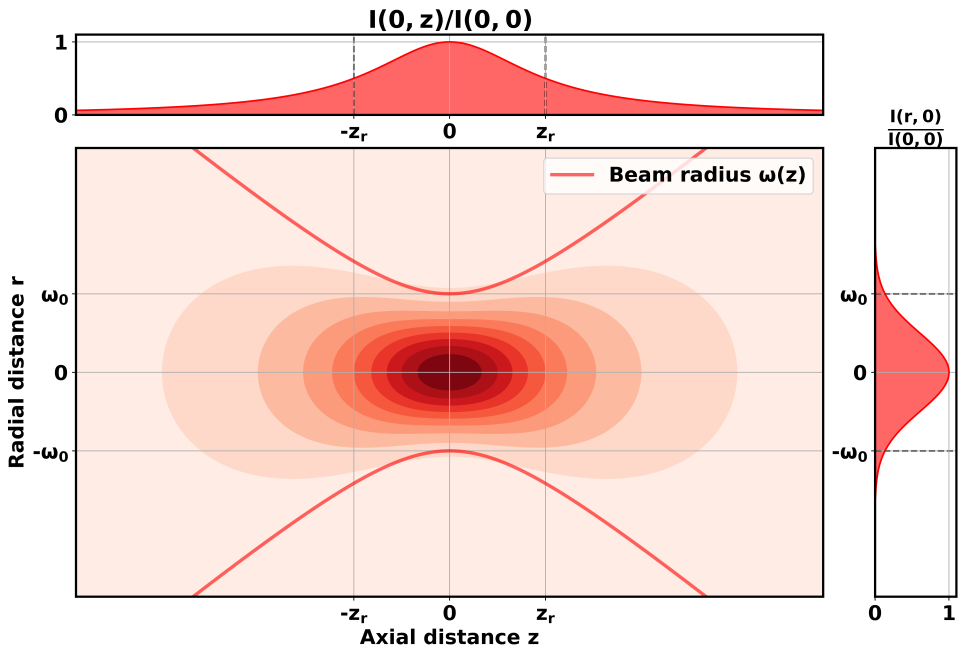

Figure 5: Single sided Gaussian intensity profile: The central graph shows the 2D intensity distribution of a normalized Gaussian beam. The plots on top and to the right show the intensity along the z- and r- axis. The red lines indicate the beam radius, where the intensity of the beam drops to $1/e^2$ of its axial value.

Finally we consider a situation where such a Gaussian beam is focused down through a lens with a focal length of f in the paraxial approximation. The relation between the waist before ω_0 and after ω_1 is the following.

$$\omega_1 = \frac{\lambda f}{\pi \omega_0} \tag{12}$$

As shown in [42] through the relations derived in [43] this expression and the paraxial approximation in general do not hold for tightly focused Gaussian beams. For these beams the paraxial approximation underestimates the beam waist and additionally does not resolve the difference in focusing for the two radial directions x and y due to polarization effects. These deviations from the paraxial approximation can be ignored for the content of this thesis as they only become relevant for focusing of fields through lenses of numerical apertures close to unity. The numerical aperture of a lens is defined as $\mathrm{NA} = n \sin\theta$ where n is the index of refraction of the surrounding medium and θ the angle of divergence a collimated beam displays after being refracted by that lens.

Gaussian standing waves

In the hollow core fiber loading mechanism as well as the optical trap Gaussian standing waves are a relevant concept. The standing waves in both cases are generated by superimposing two counter-propagating coherent Gaussian beams.

Consider two Gaussian waves $E_1(r,z)$ and $E_2(r,z)$ with equal wavelength λ, polarization vectors $\boldsymbol{p}$ and waists ω_0. The beams are propagating colinearly but their wavevectors point in opposite directions. The combined intensity of these beams is then calculated by:

$$I = \frac{c\varepsilon_0}{2}|E_1 + E_2|^2 \tag{13}$$

$$= \frac{c\varepsilon_0}{2}\left(|E_1|^2 + |E_2|^2 \; + \; E_1^* E_2 \; + \; E_1 E_2^*\right) \tag{14}$$

$$\tag{15}$$

Here the first two terms yield the respective intensities I_1 and I_2 similar to Eq.(11), whereas the last two terms are the interference terms which can be combined to the term in Eq.(16).

$$E_1^* E_2 + E_1 E_2^* = E_{01} E_{02} \frac{\omega_0^2}{\omega^2(z)} \exp\left(\frac{-2r^2}{\omega^2(z)}\right) \cos\left[2k\left(\frac{r^2}{2R(z)} + z\right)\right] \tag{16}$$

Combining the intensities I_1, I_2 with these previous expressions and denoting the relative intensity with $\chi = \frac{P_2}{P_1}$ one obtains.

$$I(r,z) = \frac{2P_1}{\pi\omega^2(z)} \exp\left(\frac{-2r^2}{\omega^2(z)}\right)\left(1 + \chi^2 + 2\chi\cos\left(2k\left(\frac{r^2}{2R(z)} + z\right)\right)\right) \tag{17}$$

For the case of the balanced standing wave meaning $\chi = 1$ this reduces to the following expression:

$$I(r,z) = \frac{8P}{\omega^2(z)} \exp\left(\frac{-2r^2}{\omega^2(z)}\right) \cos^2\left(k\left(\frac{r^2}{2R(z)} + z\right)\right) \tag{18}$$

Fig.(6) shows the intensity of a standing wave Gaussian beam for the case where $R(z) \gg r$.

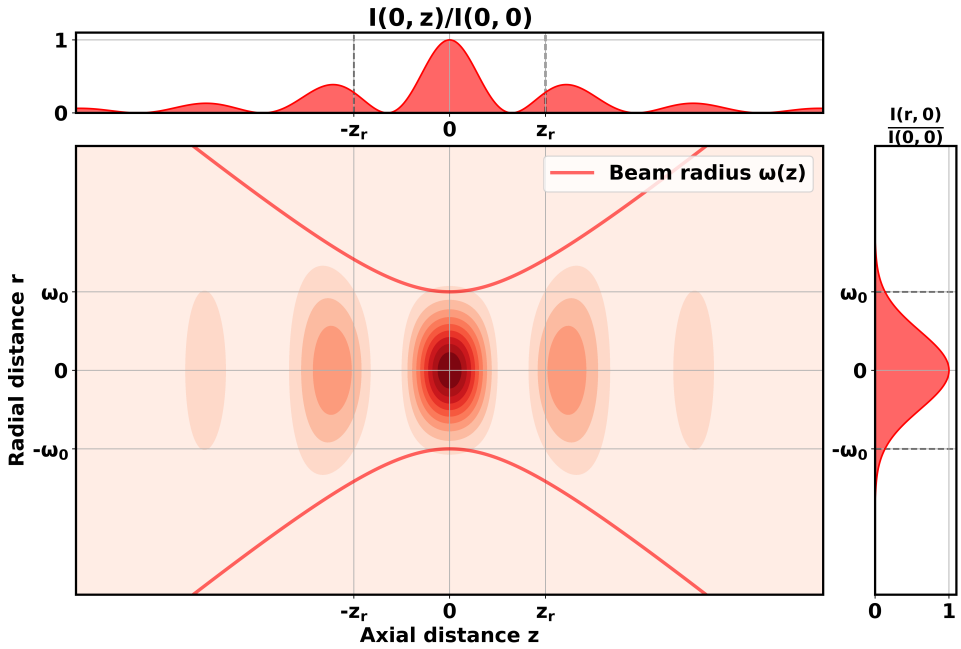

Figure 6: Standing wave Gaussian intensity profile: The central graph shows the 2D intensity distribution of a normalized standing wave Gaussian beam for the case where the wavefront curvature term is neglected. The upper plot shows the intensity distribution along the z axis and the right plot displays the intensity distribution along the radial axis.

2.2 Optical Forces

The basic principle of optical levitation are the forces acted on dielectric particles by a traveling electromagnetic wave. The following section will explore the origins and the effect of these forces acting on such a particle in the Rayleigh regime (particle radius $a \ll \lambda$).
A traveling electromagnetic wave of wavelength λ illuminates a dielectric nanoparticle and induces a point-like dipole oscillating at the frequency of the light field. The force consists of two parts: first the force acting on the charges of the dipole in a spatially inhomogeneous electric field and the Lorentz force acting on the moving dipole charges.
Following the derivation in [44] the expression for the force of a wave traveling in the z-direction on a nanoparticle of complex polarizability $\alpha = \alpha_0 \left(1 + i\frac{\alpha_0 k^3}{6\pi\varepsilon_0}\right)^{-1}$ reads:

$$\boldsymbol{F} = \boldsymbol{F}_{\text{scatt}} \ + \ \boldsymbol{F}_{\text{grad}} \tag{19}$$

$$= \frac{\alpha''}{2} I(\boldsymbol{r}) \boldsymbol{\nabla} \phi(\boldsymbol{r}) \ + \ \frac{\alpha'}{4} \boldsymbol{\nabla} I(\boldsymbol{r}) \tag{20}$$

With the wave vector $k = 2\pi/\lambda$, the dielectric constant of the nanoparticle ε, the speed of light c, the beam intensity $I(\boldsymbol{r})$, the fields real phase $\phi(\boldsymbol{r})$, the real part of the particle polarizabilty α', the imaginary part α'', $\alpha_0 = 4\pi a^3 \varepsilon_0 \frac{\varepsilon - 1}{\varepsilon + 2}$ and the vacuum permitivity ε_0.
As can be seen in Eq.(20) the force is made up of two contributions. The first term is the scattering force $\boldsymbol{F}_{\text{scatt}}$ and describes the absorption, reflection (scattering) or transmission of photons by the particle. Each absorbed photon impinges momentum of $\boldsymbol{p}_{\text{abs}} = \hbar \boldsymbol{k}$ (with $\hbar = h/2\pi$ the reduced Plank constant) and each reflected photon a momentum of $\boldsymbol{p}_{\text{ref}} = 2\hbar \boldsymbol{k}$. Thus the scattering force acts in the direction of propagation of the wave. The scattering force alone would therefore not be able to spatially confine the particle on its own.
The second part of the force is the so-called gradient force $\boldsymbol{F}_{\text{grad}}$ and is a conservative force pointing in the direction of the gradient of the electric field intensity. The gradient force enables the spacial confinement of the particle at the position z_{eq} where $\boldsymbol{F}_{\text{scatt}} + \boldsymbol{F}_{\text{grad}} = 0$. This condition is met at [41]:

$$z_{\text{eq}} = \frac{\alpha''}{\alpha'} z_R (k z_R - 1) \tag{21}$$

Optical potential and stablility criteria

The gradient force is a conservative force and can be written as the gradient of an optical potential U_{opt}.

$$\boldsymbol{F}_{\text{grad}}(\boldsymbol{r}) = -\boldsymbol{\nabla} U_{\text{opt}}(\boldsymbol{r}) \tag{22}$$

$$\tag{23}$$

And thus:

$$U_{\text{opt}}(\boldsymbol{r}) = \frac{\alpha}{c\varepsilon_0} I(\boldsymbol{r}) \tag{24}$$

The restoring force of a trapped nanosphere can, for small displacements, be linearly approximated. For the optical potential this approximation takes the form of a Taylor expansion up to the second order.

$$U(\boldsymbol{r}) \approx \sum_{i=0}^{2} \sum_{j=0}^{3} \frac{\partial^i U(\boldsymbol{r})}{\partial r_j^i}\bigg|_{r,z=0} r_j^i + \mathcal{O}(r_j^4) \tag{25}$$

The spring coefficient κ_i of this linear Hooke's law approximation is therefore the second term in this series $\kappa_i = \frac{\partial^2 U(\boldsymbol{r})}{\partial r_i^2}$. From this and the mass of the particle m one can deduce the oscillation frequency of the particle $\Omega_i = \sqrt{\frac{\kappa_i}{m}}$.

$$\Omega_i^2 = \frac{1}{m} \frac{\partial^2 U(\boldsymbol{r}, z)}{\partial x_i^2} \tag{26}$$

To ensure stable trapping of particles in optical potentials, two stability criteria have to be met [45, 46]. The first ensures that the restoring gradient force dominates over the scattering force in the direction of propagation of the beam. This is summarized in the parameter R and for the criterion to be met, the following relation has to hold.

$$R = \frac{\boldsymbol{F}_{\text{grad}} \boldsymbol{e}_z}{\boldsymbol{F}_{\text{scat}} \boldsymbol{e}_z} = \frac{3\sqrt{3}}{128\pi^5} \frac{\lambda^5}{a^3 \omega_0^2} \frac{\varepsilon + 2}{\varepsilon - 1} \gg 1 \tag{27}$$

The second criterion relates to the need of a sufficiently deep enough potential well (see Eq.(24)) to dominate over the kinetic energy of the Brownian particles of the background gas. For a particle surrounded by a gas of temperature T this stability criterion has the form of:

$$\exp\left(-\frac{U_{\text{opt}}}{k_b T}\right) \ll 10 \tag{28}$$

In most cases the trap is deemed stable if the potential at the trapping position is deeper than $10\,k_bT$ and is therefore not heated out of the trap by the Brownian noise of the background gas.

Combining these results with the single sided Gaussian beam and the standing wave Gaussian beam, we can now deduce the behavior of nanoparticles trapped in either case. For the following discussion we will always assume a beam of wavelength $\lambda = 1550\,\text{nm}$, an optical power of $P = 100\,\text{mW}$, a particle radius of $a = 75\,\text{nm}$ and a waist size of $\omega_0 = 800\,\text{nm}$ - these parameters are in the common range of previous experiments in the field.

Forces from a single sided Gaussian beam

Starting off with the intensity of a single side TEM00 mode, described in Eq.(11), we can deduce the forces acting on a nanoparticle through Eq.(20). Fig.(7) displays the forces acting in the radial and axial direction of a nanoparticle.

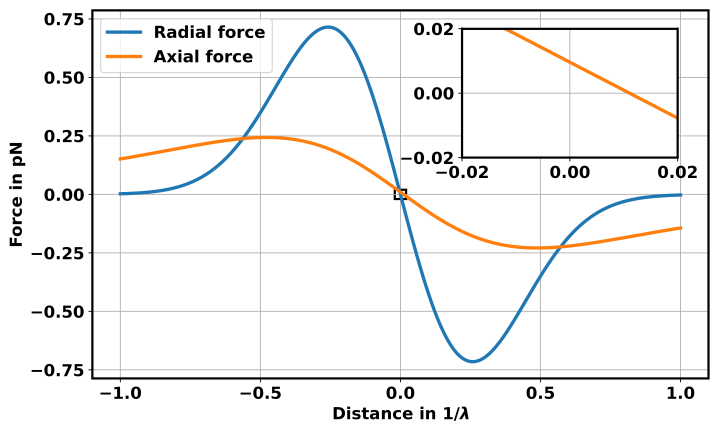

Figure 7: Forces from a single sided Gaussian beam: The force acting on a nanoparticle of radius $a = 75\,\text{nm}$, through a Gaussian beam of wavelength $\lambda = 1550\,\text{nm}$ and power $P = 100\,\text{mW}$ focused to a spot with a waist of $\omega_0 = 800\,\text{nm}$. The force in the radial and axial direction is plotted. As can be seen in the zoomed in area the force in the axial direction is not null at the origin but shifted towards the $+z$ direction due to the fact that the scattering force F_{scatt} acts in the direction of the traveling beam.

The force experienced in the radial direction exceeds the force in the axial direction due to the tighter confinement. Following from Eq.(21) the zero point of the force along the axial direction is offset by $z_{eq} = 0.017\,\lambda$ due to the scattering force pointing along the direction of propagation of the wave.

Inserting the optical potential calculated from Eq.(24) we get the following axial and radial frequencies for the trapped particle.

$$\Omega_r^2 = \frac{4P\alpha_0}{m\pi c\varepsilon_0}\frac{1}{\omega_0^4} \tag{29}$$

$$\Omega_z^2 = \frac{4P\alpha_0}{m\pi c\varepsilon_0}\frac{1}{\omega_0^2 z_R^2} \tag{30}$$

Calculating these frequencies for the same values as used above and assuming a silica particle of density $\rho = 2450\,\frac{\mathrm{kg}}{\mathrm{m}^3}$ and radius $a = 75\,\mathrm{nm}$ we get the following particle frequencies.

$$\Omega_r \approx 2\pi \cdot 92\,\mathrm{kHz}$$

$$\Omega_z \approx 2\pi \cdot 57\,\mathrm{kHz}$$

It can be seen that due to the difference in particle confinement along the axis a higher trapping frequency for the radial directions than for the axial one is displayed.

The stability criteria (Eq.(27 & 28)) are checked for the case of the single sided beam. Calculating the R parameter denoting the axial stability of the beam, for the parameters given, we get $R \approx 3.9$. This shows sufficient dominance of the gradient force over the scattering force.
The second criterion demanding a deep enough potential well is displayed in Fig.(8). Here the axial and radial profile of the optical potential in units of k_bT (with $T = 300\,\mathrm{K}$) is displayed. The red area is the region where this potential would not meet the $10\,k_bT$ criteria. It is clearly visible that the condition of Eq.(28) is easily met, especially for the center of the potential.

Forces from a Gaussian standing wave

The force acting on a levitated nanoparticle trapped in the central maximum of a standing wave gaussian beam is depicted in Fig.(9). Along the axis of propagation the force now has several points where its value is zero. Additionally, the force along the axis of propagation is now higher than the radial force due to the increased confinement of the standing wave maxima. To make the comparison between the single sided and the standing wave case more apparent, here the (single sided) power is set to $P_s = 50\,\mathrm{mW}$ as this sums up to a total power of $P_t = 100\,\mathrm{mW}$.
In comparison to the case of the single sided Gaussian beam there is no offset for the zero points of the axial force because the scattering term for the balanced standing wave is equal to zero.

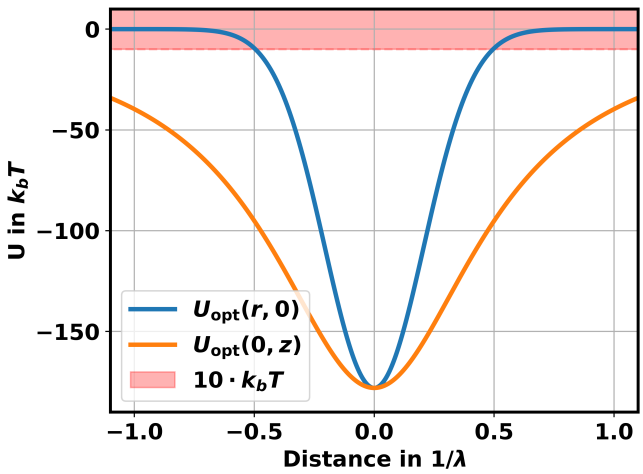

Figure 8: Stability criterion for a single sided Gaussian beam: The optical potential created by a Gaussian beam of wavelength $\lambda = 1550\,\text{nm}$ and power $P = 100\,\text{mW}$ that is focused down to $\omega_0 = 800\,\text{nm}$. The red region suggests a potential depth below $10\,k_bT$. This figure shows that these parameters give a sufficiently deep potential well according to Eq.(28).

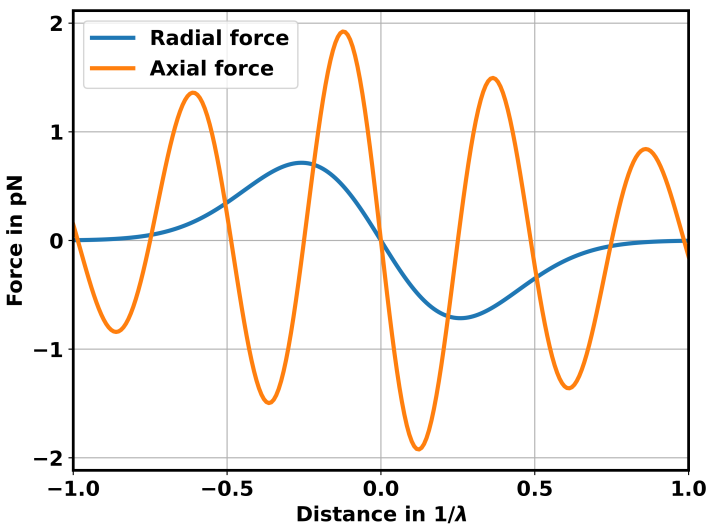

Figure 9: Forces from a Gaussian standing wave: The force acting on a nanoparticle of radius $a = 75\,\text{nm}$, by a balanced Gaussian standing wave with $\lambda = 1550\,\text{nm}$ and (total) power $P_t = 100\,\text{mW}$ focused to a spot with a waist of $\omega_0 = 800\,\text{nm}$. The force in the radial and axial direction is plotted.

Taking a look at the particle frequencies we get in a standing wave configuration the harmonic approximating gives the following expression for the axial and radial frequencies.

$$\Omega_{r,SW}^2 = \frac{16 P_s \alpha_0}{c\pi\varepsilon_0 m} \frac{1}{\omega_0^4} \tag{31}$$

$$\Omega_{z,SW}^2 = \frac{16 P_s \alpha_0}{c\pi\varepsilon_0 m} \frac{1}{\omega_0^2} \left(\frac{1}{z_R^2} + k^2 \right) \tag{32}$$

Inserting numbers into these equations gives us these frequencies:

$$\Omega_{r,SW} \approx 2\pi \cdot 131\,\mathrm{kHz}$$

$$\Omega_{z,SW} \approx 2\pi \cdot 430\,\mathrm{kHz}$$

As expected, the radial frequencies increase by a factor of $\sqrt{2}$ compared to the single sided case and the axial frequency even more due to the higher curvature of the confining potential along this direction.

The stability criteria for the Gaussian standing wave are calculated in the same manner as before. For the axial stability we see that for the case of a balanced standing wave the R parameter approaches infinity and thus the axial stability is always given.
The second stability criterion of Eq.(27) is checked for the standing wave potential in Fig.(10). Along with the central trapping position at the waists of the counter-propagating beams there are other stable trapping positions at the side maxima of the standing wave intensity separated by a distance of $\lambda/2$,

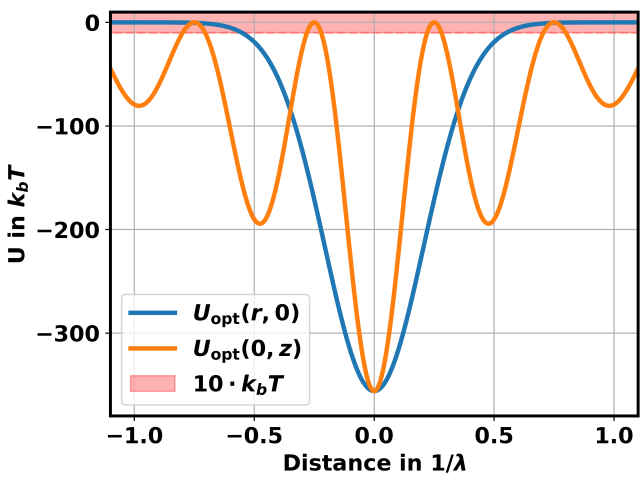

Figure 10: Stability criterion for a Gaussian standing wave: The optical potential created by a Gaussian beam standing wave of wavelength $\lambda = 1550\,\mathrm{nm}$ and (total) power $P_t = 100\,\mathrm{mW}$ that is focused down to $\omega_0 = 800\,\mathrm{nm}$. The red region suggests a potential depth below $10\,k_bT$. This figure shows that these parameters give a sufficiently deep potential well according to equation 28.

2.3 Particle dynamics

A particle confined in an optical trap at finite pressures experiences random kicks from background gas molecules making the description of its dynamics necessarily a stochastic one. This section gives a basic description of the dynamics of an optically trapped particle. At ambient pressures the dynamics of the particle are governed by the viscous force due to random collisions with the background gas. For small oscillations, the levitated nanoparticle behaves like a damped driven harmonic oscillator of frequency Ω_0 and its dynamics are governed by the following Langevin equation:

$$\ddot{x}(t) + \gamma\dot{x}(t) + \Omega_0^2 x(t) = \frac{1}{m} F_{\mathrm{th}}(t) \tag{33}$$

Here x denotes the particle trajectory, γ the damping rate and F_{th} is the thermal force introduced by the background gas. This stochastic force noise satisfies the condition in Eq.(34):

$$\langle F_{\mathrm{th}}(t) F_{\mathrm{th}}(t-\tau)\rangle = 2m\gamma k_b T \delta(\tau) \tag{34}$$

Where τ is some temporal delay and the δ-function with the argument τ signifies that the stochastic force noise is uncorrelated with itself at any other time.

The gas damping rate γ dependent on the local pressure p, is given by [47]:

$$\gamma = \frac{6\pi\eta a}{m} \frac{0.619}{K_n + 0.619} \left(1 + \frac{0.310\, K_n}{K_n^2 + 1.152\, K_n + 0.785}\right) \tag{35}$$

Where η is the viscosity of the gas, m the particle mass and $K_n = \Lambda_{\mathrm{free}}/a$ the Knudsen number given by the ratio of the mean free path of a background gas molecule and the particle radius a.

For the case of long mean free paths and thus $K_n \gg 1$, given at pressures $p < 10\,\mathrm{mbar}$, Eq.(35) simplifies to [48]:

$$\gamma = \frac{64}{3} \frac{a^2 p}{m \tilde{v}_{\mathrm{gas}}} \tag{36}$$

Here $\tilde{v}_{\text{gas}} = \sqrt{\frac{8RT}{\pi M_{\text{gas}}}}$ is the average background gas velocity, M_{gas} the molar mass of the gas and R the universal gas constant.
The most straight forward way to solve Eq.(33) is to switch to frequency space via a Fourier transform. This gives:

$$-\omega^2\tilde{x}(\omega) - i\gamma\omega\tilde{x}(\omega) + \Omega_0^2\tilde{x}(\omega) = \frac{1}{m}\tilde{F}_{\text{th}}(\omega) \tag{37}$$

Solving this expression for $\tilde{x}(\omega)$ results in:

$$\tilde{x}(\omega) = \frac{1}{m}\frac{\tilde{F}_{\text{th}}(\omega)}{\Omega_0^2 - \omega^2 - i\omega\gamma} \tag{38}$$

From this expression for the trajectory in frequency space we can deduce the power spectral density of the oscillator through the Wiener-Khinchim theorem. It links the autocorrelation function $\langle x(t) - x(t-\tau)\rangle$ to the power spectral density $S_{x,x}$ through the following expression (for the case where $\tau = 0$):

$$S_{x,x} = \langle|\tilde{x}(\omega)|^2\rangle \tag{39}$$

Now plugging in the expressions from Eq.(38) together with the condition of the force noise term F_{th} from Eq.(34) we get this final expression for the power spectral density (PSD) of the damped harmonic oscillator:

$$S_{x,x}(\omega) = \frac{2k_bT}{m\Omega_0^2}\frac{\Omega_0^2\gamma}{(\Omega_0^2 - \omega^2)^2 + \gamma^2\omega^2} \tag{40}$$

2.4 Feedback cooling

Laser noise, vibrations of the trap position [49] and internal heating of the trapped nanoparticles as described in [50, 51] are some mechanisms that heat the center of mass (CM) motion of a levitated particle. These effects or a mixture thereof, lead to the loss of trapped nanoparticles at pressures between $1 - 0.01\,\mathrm{mbar}$ as reported from different research groups and experiments [32, 34, 50, 52, 53].
To ensure stable trapping below these pressures, a feedback mechanism has to be employed that effectively reduces the energy of the particle. This section gives a short introduction into the dynamics of cooled levitated nanoparticles and the two feedback methods used in this experiment.

2.4.1 Feedback cooled particle dynamics

The previous section introduced the general description of the dynamics of optically levitated particles. Here we will discuss the updated dynamics for a particle experiencing feedback cooling.
Introducing an external feedback force F_{fb} modifies the Langevine equation to:

$$\ddot{x}(t) \; + \; \gamma\dot{x}(t) \; + \; \Omega_0^2 x(t) = \frac{1}{m}(F_{\mathrm{th}}(t) + F_{\mathrm{fb}}(t)) \tag{41}$$

Where F_{fb} is the feedback force parametrized as $F_{\mathrm{fb}} = m\gamma_{\mathrm{fb}}\dot{x} = mg\gamma\dot{x}$ introduced by the feedback signal and g the gain of the feedback. The feedback damping γ_{fb} is expressed as the feedback-gain g multiplied by the gas damping γ. Following the same steps as in chapter 2.3 we can now deduce the power spectral density of such a feedback cooled particle.

$$S_{x,x}(\omega) = \frac{2k_bT}{m\Omega_0^2}\frac{\Omega_0^2\gamma}{(\Omega_0^2-\omega^2)^2+\gamma^2\omega^2(1+g)^2} \tag{42}$$

This PSD of the cooled particle reduces to Eq.(40) for a gain of $g = 0$. Fig.(11) shows the PSD for a particle at resonance frequency of $\Omega_0 = 2\pi \cdot 300\,\mathrm{kHz}$ with a damping rate of $\gamma = 2\pi \cdot 15\,\mathrm{kHz}$ at temperature $T = 300\,\mathrm{K}$ for gains of $g = 0$ and $g = 25$.
Using the Wiener-Khinchim theorem at $\tau = 0$ it once more gives us an expression for the mean squared displacement $\langle x^2(t)\rangle$ of the particle.

$$\langle x^2(t)\rangle = \int d\omega S_{x,x}(\omega) = \frac{k_bT}{m\Omega_0^2}\frac{1}{1+g} \tag{43}$$

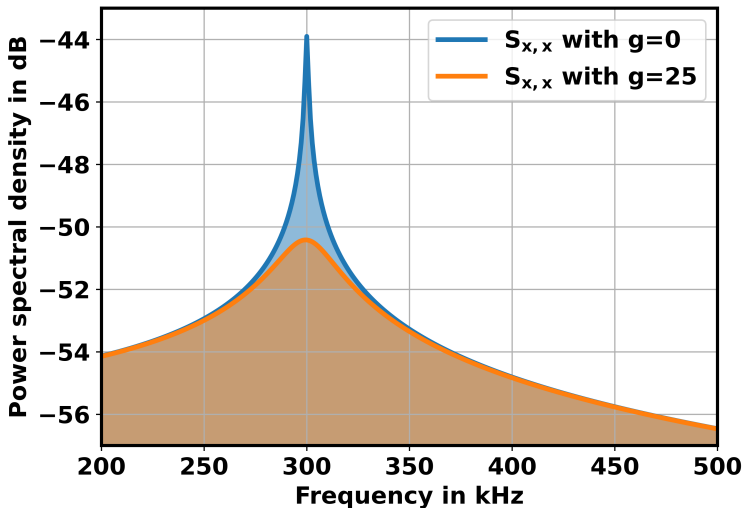

Figure 11: Power spectral density of a levitated particle: The PSD for a particle at resonance frequency of $\Omega_0 = 2\pi \cdot 300\,\mathrm{kHz}$, at a damping rate of $\gamma = 2\pi \cdot 1\,\mathrm{kHz}$, at temperature $T = 300\,\mathrm{K}$ for gains of $g = 0$ and $g = 10$. As can be seen the increase of the gain lowers the peak of the PSD and overall decreases the area under it.

The equipartition theorem with a temperature associated to the center of mass motion of the particle T_{CM} states the following:

$$k_b T_{\mathrm{CM}} = m\Omega_0^2 \langle x^2 \rangle \tag{44}$$

Inserting the result from Eq.(43) into this, we get an expression for the center of mass motion temperature dependent on the feedback gain g.

$$T_{\mathrm{CM}} = T\left(\frac{1}{1+g}\right) \tag{45}$$

Considering only this expression the misconception that an ever higher feedback gain leads to ever lower center of mass motion temperatures might arise. This cannot in fact be done because until now the aspect of detection imprecision was left out.

The signal recorded by any detection scheme suffers from imprecision and therefore a detection noise term $x_n(t)$ will be added to the real particle trajectory $x(t)$. This means that the feedback force F_{fb} does not only feed back on the actual particle motion but also on the detection noise of the system [8, 54]. Looking at one final adjustment of the equation of motion we get:

$$\ddot{x}(t) + \gamma\dot{x}(t) + \Omega_0^2 x(t) = \frac{1}{m}F_{\text{th}}(t) + g\gamma(\dot{x} + \dot{x}_n) \tag{46}$$

Switching to the Fourier plane and calculating the power spectral density we get the following expression:

$$S_{x_n,x_n}(\omega) = \frac{2k_bT}{m\Omega_0^2}\frac{\Omega_0^2\gamma}{(\Omega_0^2-\omega^2)^2+\gamma^2\omega^2(1+g)^2} + \frac{g^2\gamma^2\omega^2 S_{x_n,x_n}(\omega)}{(\Omega_0^2-\omega^2)^2+\gamma^2\omega^2(1+g)^2} \tag{47}$$

If we now assume that the power spectral density of the detection noise S_{x_n,x_n} is constant in frequency (as is in most cases) we can now re-derive the expression for temperature associated to the center of mass motion T_{CM} via the equipartition theorem:

$$T_{\text{CM}} = T\left(\frac{1}{1+g} + \frac{g^2}{1+g}\frac{\gamma S_{x_n,x_n}}{2}\right) \tag{48}$$

This expression now shows that for an imperfect (real) detection system, increasing the feedback gain indefinitely will in fact lead to heating of the particle after a certain optimal gain g_{opt}. This heating occurs because the mechanism begins to feed back the detection noise into the system. The optimal gain parameter can be calculated by finding the extrema of Eq.(48) with respect to g. This gives the following expression:

$$g_{\text{opt}} = \sqrt{\gamma^{-1}S_{x_n,x_n}^{-1} + 1} - 1 \tag{49}$$

Finally, if we want to know how one would see this power spectral density on a spectrum analyzer, one has to calculate $S_{x+x_n} = \langle|\tilde{x} + \tilde{x}_n|\rangle$. This expression reads:

$$S_{x+x_n}(\omega) = \frac{2k_bT}{m\Omega_0^2}\frac{\Omega_0^2\gamma}{(\Omega_0^2-\omega^2)^2+\gamma^2\omega^2(1+g)^2} + \frac{(\Omega_0^2-\omega^2)^2+\gamma^2\omega^2}{(\Omega_0^2-\omega^2)^2+\gamma^2\omega^2(1+g)^2}S_{x_n,x_n} \tag{50}$$

Fig.(12A-C) show the power spectral density S_{x+x_n} for a particle of resonance frequency of $\Omega_0 = 2\pi \cdot 300\,\text{kHz}$, damping rate of $\gamma = 2\pi \cdot 1\,\text{kHz}$, temperature $T = 300\,\text{K}$, for 3 different feedback gains. The dashed lines show the PSD $S_{x,x}$ of Eq.(42).

The gain chosen in Fig(12A) is small and thus the difference from the uncooled spectrum is a rather small one. In part B the gain chosen is the optimal gain from Eq.(49). There it can be seen that the actual cooled particle spectrum is almost exactly on the height of the detection noise. The displayed spectrum S_{x+x_n} is still above the detection noise to the left

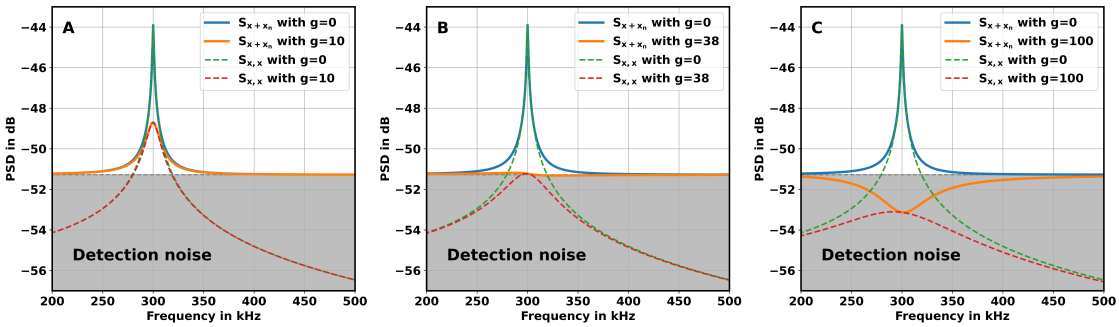

Figure 12: Real PSDs for different feedback gains: The PSDs for the case where the detection noise x_n is accounted for (solid line) and once without it (dashed line). The parameters for this trapped particle are a resonance frequency of $\Omega_0 = 2\pi \cdot 300\,\text{kHz}$ with a damping rate of $\gamma = 2\pi \cdot 15\,\text{kHz}$ and at temperature $T = 300\,\text{K}$. The grey area shows S_{x_n,x_n} the constant power spectral density of the detection noise. The case for $g = 0$ is shown in every graph. In **A** a low gain is chosen, in **B** the optimal gain calculated through Eq.(49) and in **C** a gain exceeding the optimal gain.

of the resonance frequency of the particle while to the right it already dips slightly below. In graph C the spectra for a feedback gain above the optimal gain g_{opt} are depicted. Here we see that the orange line depicting the read out spectrum S_{x+x_n} already dips below the detection noise. This effect is known as noise squashing [35, 54, 55]. As discussed above, at feedback gains of this height the particle is not cooled further but rather heated up again.

In our experiment two different feedback mechanisms are employed, namely parametric feedback cooling as performed in [41, 56] and linear electric feedback cooling as in [8, 9]. Here we note that the previous calculations were done for a linear feedback force $F_{\text{fb}} = mg\gamma\dot{x}$ as this is the more important type of feedback in our setup intended to prepare the particle into or close to its motional groundstate. Similar derivations can be done for parametric feedback as can be seen in [41].

2.4.2 Parametric feedback cooling

Fig.(13) depicts the schematic working principle of the parametric feedback cooling technique.

Fig.(13A) displays the schematic setup for parametric feedback cooling. A laser beam passing through an intensity modulator is focused down to create an optical trap where a particle is confined. The three-dimensional movement of the particle is detected. The signal for each axis is then frequency doubled by multiplying the trajectory of the particle $x(t)$ with its derivative $\dot{x}(t)$ and thereafter phase-shifted. The three separate signals are then summed up and sent to the modulator which in turn adjusts the laser intensity accordingly.

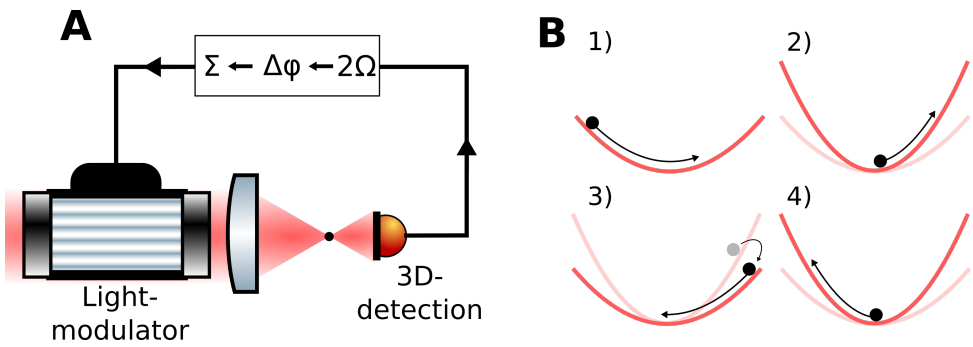

Figure 13: A) Parametric feedback scheme: The motion of a levitated nanoparticle is detected along three axis. The recorded signals are frequency doubled, phase shifted, summed up and sent to a light modulator that adjusts the trapping intensity accordingly. **B) One Parametric feedback cycle:** A full parametric feedback cycle is depicted. The modulator changes the steepness of the trap (in red) whenever the particle starts to climb the well and decreases the steepness when it oscillates back to the trap center. This will effectively decrease the particles motional energy.

In Fig.(13B) one feedback cycle is depicted. In 1) the particles moves down a shallow potential (low laser intensity). Once the particle enters the center of the trap in 2) the intensity is increased. This means the particle has to climb a steeper potential wall and therefore loses some of its kinetic energy. In 3) the particle reaches the maximal displacement where the potential is switched back to the shallow one. Thus the particle will not gain back the same kinetic energy it has spent to go up the potential wall. At this point the cycle repeats only in the opposite direction. Hence the increase and decrease of the signal happens at twice the oscillation frequency explaining the need for the frequency doubling. The result of this cycling is a loss of energy for the particle and a net cooling of its center of mass motion.

2.4.3 Linear feedback cooling

Additionally to the parametric feedback cooling that cools the motion of the nanoparticle in all three axes we employ linear cooling only along one axis of the particle motion. Instead of modulating the trapping light to reduce the motional energy of the particle, an external electric field acting directly at the particle is applied. Most nanoparticles carry a non-zero net charge and thus an electric field will result in a Coulomb force acting on the particle. Fig.(14) depicts the linear feedback scheme.

In Fig.(14A) the general linear cooling scheme for one axis is shown. A particle is levitated in an optical trap created by a focused light beam and the motion of the particle along the axis of propagation of the trapping beam is detected. From this signal detecting the particle position, the particle velocity is generated by derivation. This signal is then applied to an electrode and between it and another grounded electrode an electric field is

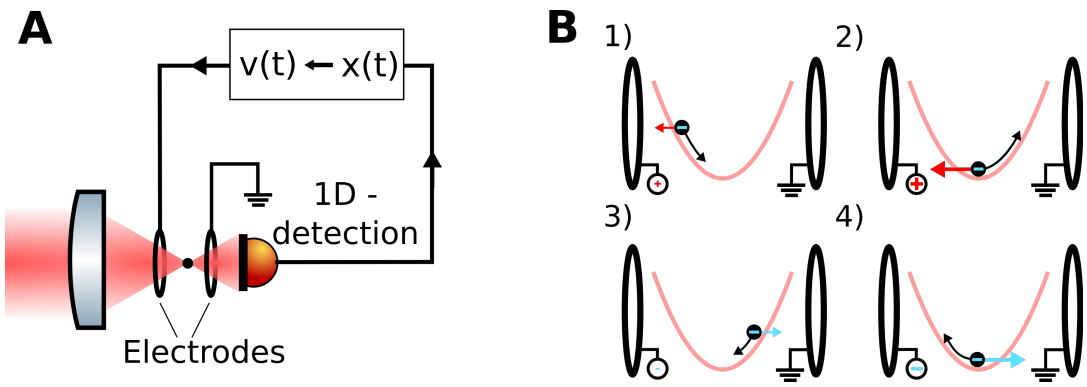

Figure 14: A) Linear feedback scheme: A general linear feedback scheme is depicted. A feedback signal proportional to the particle velocity is sent to an electrode along the detected axis of motion. Between it and a second grounded electrode an electric field is formed that acts on the net charges of the particle. **B) One linear feedback cycle:** In light red the optical trapping potential is depicted and within it the particle (with a net negative charge). The electrodes apply feedback on the position of the particle dependent on the velocity of the oscillator. This sinusoidal Coulomb force will lead to a "cold" damping of the particle motion and a net cooling.

created. This electric field induces a Coulomb force on the net charge of the nanoparticle proportional to the velocity. This velocity dependent force is also the reason this cooling method is often called cold damping [35, 57].

In Fig.(14B) one feedback cycle is depicted. The optical potential the particle is confined to is depicted as a light red parabola. In part 1) a net negative charged particle moves towards the trap center with a small velocity and thus a small positive voltage is applied to the left electrode. This results in a small Coulomb force acting on the particle (seen as a red arrow). The particle increases its velocity as it approaches the trap center in part 2) and with it the voltage is also increased. When the particle moves up the potential well its velocity as well as the Coulomb force is decreased. Upon reversing the direction of motion, the voltage on the left electrode switches its sign and the reverse process starts in part 3) of the figure. The repetition of this cycle will lead to an ever smaller variance in the particle position, with it a decrease in the motional energy and thus a cooling of this degree of freedom.

This second cooling mechanism will be employed after a pre-cooling phase performed through three-dimensional parametric feedback cooling and is used to cool the motion along the axial direction down to or close to the motional ground state of the particle.

2.5 Particle detection

The ability to cool an optically levitated particle down to its motional ground state is directly related to the amount of information about the particle trajectory that can be collected [58]. From Eq.(48) we also see that the cooling limit is highly dependent on the amount of detection noise inherent to the system. Decreasing detection noise and thereby increasing the information about the particle trajectory is thus essential to achieve ground state cooling. This section will elaborate on the methods and theory of the detection system we utilize in our experiment.

2.5.1 Dipole scattering

In order to efficiently detect the motion of an optically levitated particle, its scattered light field containing a position dependent phase is collected. In chapter 2.2 we established that a trapped particle acts as a induced point-dipole. The electric field of such a dipole at distance $R \gg \lambda$ reads [59]:

$$E_d(r,\theta) = \frac{k^2 \sin\theta}{4\pi\varepsilon_0} \frac{e^{ikr}}{r} \alpha E_0 \tag{51}$$

Where α is the polarizability of the particle and θ is the angle between the polarization vector of the the incident light field E_0 and the direction of propagation of the dipole-field. In order to detect this scattered light one has to figure out how much of it is scattered backwards and forwards into the Gaussian beam trapping the particle. This has previously been done for atoms in [60] and for levitated particles in [48]. In both cases the question was not how much light is back/forward-scattered but how much light is scattered into a (cavity-)mode that is orthogonal to the trapping mode. As Eq.(51) is not dependent on the polar direction of the incoming beam, this problem can be treated in the same way as is done in the two cavity cases.

The amount of light scattered back into these modes is defined by the overlap integral between the Gaussian trapping beam and the radiated field. The Gaussian beam (for $z \gg z_R$) can be approximated by:

$$E_g(\rho,z) = E_0 \frac{\omega_0}{\omega(z)} e^{\frac{-\rho^2}{\omega(z)^2}} e^{-ik\left(z+\frac{\rho^2}{2z}\right)} \tag{52}$$

The overlap integral is calculated at distance f from the focus of the Gaussian beam (ω_0) where the trapping beam has the waist $\omega_1 = \omega(f)$. At this distance we know that $R \gg \lambda$, so the far field approximation for the dipole allows the following simplification

$e^{ikr}/r = e^{ikz+ik\rho^2/(2z)}/z$. Further we are only interested in angles $\delta\theta$ around $\theta = \pi/2$, which are given by the numerical aperture (NA) of the trapping lens $\delta\theta_{\max} = \pm\arcsin(\mathrm{NA})$. So in order to account for the scattering into the angles defined by the NA we integrate $\sin(\theta)$ over the relevant angles giving $\int_{\mathrm{NA}} \sin(\theta) d\theta = \int_{-\delta\theta_{\max}}^{\delta\theta_{\max}} \cos(\delta\theta)\, d\delta\theta = 2\mathrm{NA}$. So the expression for the radiated field (far from the focus) into angles defined by the NA reads:

$$E_d(\rho, z) = \frac{k^2 \mathrm{NA}}{2\pi\varepsilon_0} \frac{e^{ik+\frac{ik\rho^2}{2z}}}{z} \alpha E_0 \tag{53}$$

Now defining the overlap integral through a plane perpendicular to the axis of propagation z we can write:

$$\frac{1}{E_0^2} \int_0^{2\pi} \int_0^{\infty} E_d E_g \rho \, d\rho \, d\varphi = \frac{k^2 \mathrm{NA} \alpha}{\varepsilon_0} \frac{\omega_0}{\omega(z) z} \int_0^{\infty} \rho e^{\frac{-\rho^2}{\omega^2(z)}} d\rho \tag{54}$$

$$= \frac{k^2 \alpha \omega_0}{2\varepsilon_0} \frac{\omega(z)}{z} \tag{55}$$

Using the relation from Eq.(56-58) and dividing the result in Eq.(55) by the effective mode area $A = \frac{\pi\omega_0}{2}$ we get the equation for our mode-matching factor β.

$$\omega_0 = \frac{2}{k\mathrm{NA}} \tag{56}$$

$$z_R = \frac{2}{k\mathrm{NA}^2} \tag{57}$$

$$\omega(z) \overset{z \gg z_R}{=} \omega_0 \frac{z}{z_R} = z\mathrm{NA} \tag{58}$$

This gives:

$$\beta = \frac{1}{A} \frac{1}{E_0^2} \int_0^{2\pi} \int_0^{\infty} E_d E_g \rho \, d\rho \, d\varphi \tag{59}$$

$$= \frac{\alpha k^2 \mathrm{NA}^3}{2\pi\varepsilon_0} \tag{60}$$

This factor β connects the amplitude of the field scattered back (or forward) $E_{\mathrm{b/f}}$ to the amplitude of the trapping beam in the following way:

$$E_{\mathrm{b/f}} = i\beta E_g \tag{61}$$

The imaginary unit i comes from the Gouy phase at great distance that we omitted in Eq.(52). The β parameter is the reflectance/transmittance of the nanoparticle back into the Gaussian trapping mode. As can already be seen in Eq.(51), the particle scatters its field equally in the forward and backwards direction thus β stays the same for both directions.

2.5.2 Detectable information

While the amount of photons scattered into the forward and backward direction is the same, from Tebbenjohanns et al. [61] we know that the amount of information scattered by the particle is not symmetric. From [62] we get that the probability density for a particle to scatter a photon in direction $\vec{k}_f = (\cos\varphi\sin\theta, \sin\varphi\sin\theta, \cos\varphi)$ is given by:

$$P(\vec{k}_f) = \frac{3}{8\pi}\left(\cos^2(\theta)\cos^2(\varphi) + \sin^2(\varphi)\right) \tag{62}$$

This probablity density is depicted Fig.(15A) (for a particle at $\vec{r} = 0$ trapped in a beam moving along the z axis). Here we see that the probability density is symmetric for the +z and -z direction. On the other hand, the information scattering into direction $\vec{k}_f$ is given through Eq.(63):

$$P^*(\vec{k}_f) = P(\vec{k}_f)(A - \cos\theta)^2 \tag{63}$$

Here A is a geometrical factor dependent on the NA of the lens focusing the trapping beam and can be calculated from the appendix in [61]. The probability density from Eq.(63) is displayed in Fig.(15B) and clearly shows a disparity concerning directions. Most of the information about the particle position is actually scattered backwards not forwards.
Fig.(16) displays the direct comparison of the probability-densities in the x-z and y-z plane. A zoom- in for the forward scattering is also included.
In order to quantitatively compare the amount of information with the amount of photons scattered, we calculate the the integral over P and P^* for the relevant angles and divide it by the total photons/information scattered [8]:

$$\eta_{\text{coll}}^{(*)} = \frac{\int_{\Omega_{\text{coll}}} P^{(*)}(\vec{k}_f)d\Omega}{\int_{4\pi} P^{(*)}(\vec{k}_f)d\Omega} \tag{64}$$

Here $d\Omega = \sin\theta d\theta d\varphi$ is the solid angle and Ω_{coll} the angles defined by the NA of the trapping lens.

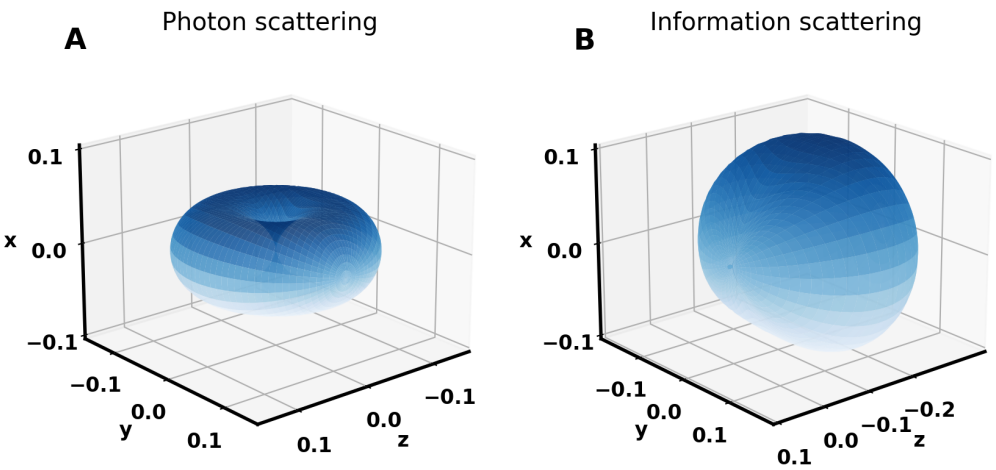

Figure 15: A) Photon scattering pattern: The probability density of a trapped nanoparticle scattering a photon into a given direction. The distribution is symmetric in z and y. **B) Information scattering pattern:** The probability density of not photons but information scattering in the z direction. There is a clear asymmetry in the directionality of the information and most of it is scattered backwards not forwards.

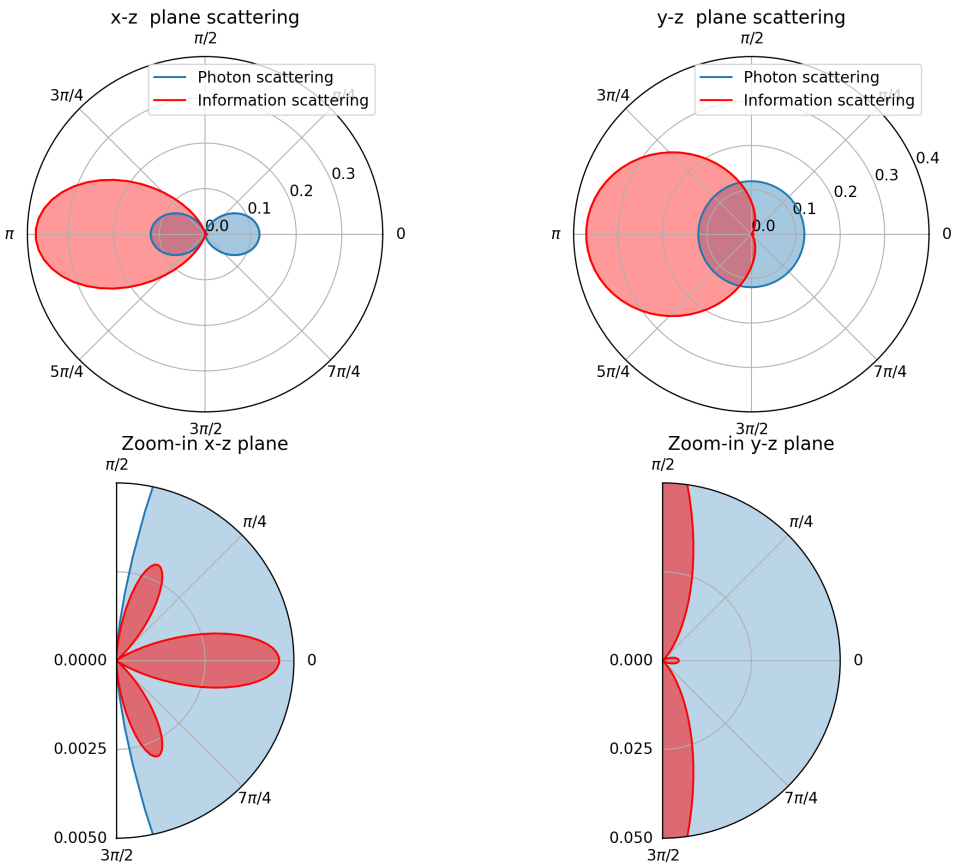

Figure 16: 2D photon and information scattering: The 2D patterns of the scattering of photons and information in the z direction for a dipole induced by a field polarized along x and traveling in the z direction.

For the case of NA = 0.6 at wavelength $\lambda = 1550\,\mathrm{nm}$ we get a photon collection efficiency of only $\eta_{\mathrm{coll}} \approx 0.14$ but an information collection efficiency of $\eta^*_{\mathrm{coll}} \approx 0.37$.

In the case of a standing wave trap, both beams can be efficiently collected and separated by the means of a Michelson-Sagnac interferometer.

2.5.3 Detection of a particle in a standing wave: Michelson-Sagnac interferometer

As we have seen in the last section most of the information radiated by the particles is scattered backwards not forward. Therefore it is beneficial to collect as much of this back-scattered light as possible, as is done in [8, 9, 63].
The fact that our experiment utilizes a standing wave optical trap makes copying the schemes of these experiments not feasible. In a double sided trap we would always also detect the forward scattered light that contains much less information about the particle position. So in order to filter the back-scattered light of the particle from the trapping light and the forward-scattered light we employ a Michelson-Sagnac interferometer. Such interferometers have been thought of previously by different groups on optomechanical systems such as membranes [64, 65] or levitated nanoparticles [66, 67].

Fig.(17) displays the general setup of a Michelson-Sagnac interferometer. Light enters into a 50/50 beamsplitter from mode a (further called the bright-port) of the interferometer and is split into mode c and d. At position R along the interferometer a particle is trapped in the standing wave intensity maximum between two high NA lenses (not included in Fig.(17)). The total length of the interferometer is denoted by L.
The reason for calling this a Michelson-Sagnac interferometer is apparent if one imagines a semitransparent mirror instead of a particle there. The Sagnac mode describes the light that is transmitted through the mirror and interferes back at the beamsplitter to exit from the port it entered. As we will see below, the Michelson mode is describing the part of the beam that is reflected at the mirror and interferes at the beamsplitter to exit through the other port (port B in Fig.(17), further called the dark-port).
The 50/50 beamsplitter transformation we are going to use for the calculation, are defined as follows:

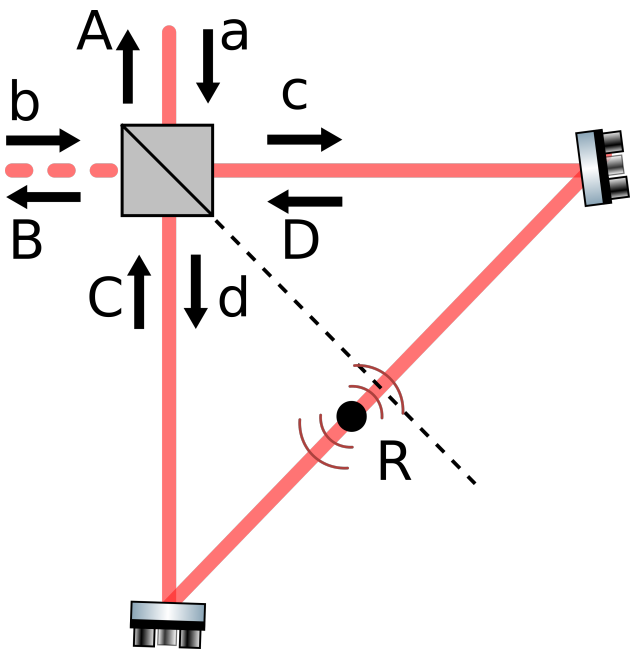

Figure 17: Michelson-Sagnac interferometer: This MS-interferometer of total length L is created by a beam entering through mode a. At position R along the beampath a levitated nanoparticle is trapped between two lenses (not included in this schematic). The letter $a - d$ and $A - D$ denote the modes entering and leaving the beamsplitter on the in-/outside of the interferometer.

$$c = \frac{a+b}{\sqrt{2}} \tag{65}$$

$$d = \frac{a-b}{\sqrt{2}} \tag{66}$$

$$A = \frac{D+C}{\sqrt{2}} \tag{67}$$

$$B = \frac{D-C}{\sqrt{2}} \tag{68}$$

To deduce what mode A and B look like we will propagate mode c and d through the interferometer. Upon entering, these modes can be described by:

$$c(z) = c_0 e^{ikz} e^{i\phi(z)} \tag{69}$$

$$d(L-z) = c_0 e^{ik(L-z)} e^{i\phi(L-z)} \tag{70}$$

$$\tag{71}$$

Here $\phi(z) = \zeta(z - L/2) = \arctan\left(\frac{z-L/2}{z_R}\right)$ is the Gouy phase in a shifted coordinate system.

When propagating through the interferometer, these modes interact with the particle which will scatter light as described in the previous section. The mode C and D consist of three modes each, namely the mode that has not interacted with the particle, the light that is forward scattered by the particle c_t/d_t and the light that is reflected of the particle c_r/d_r from the counterpropagating mode. We will denote the mode matching factor for the light transmitted as β_t and the one for the reflected part as β_r.
The mode C at the position L at the beamsplitter can be described in the following way:

$$C(L) = c(L)(1-l) + c_t(L) + c_r(L) \tag{72}$$
$$= c_0 e^{i(kL+\phi(L))}(1-l) + i\beta_t c_0 e^{i(kL+\phi(L))} + i\beta_r d_0 e^{2i(k(L-R)+\phi(L-R))} \tag{73}$$

Here l denotes the amount of the trapping beam that is scattered and not in the original mode c anymore. We can see that the transmitted part of the beam travels the length L, while the reflected part for this mode travels the length $2(L-R)$. This length is longer or shorter than the path L, depending on the particle postion R. The i in the reflected and transmitted part is the i stemming from the Gouy phase in Eq.(61). The same thoughts can be applied to the D mode:

$$D(L) = d_0 e^{i(kL+\phi(L))}(1-l) + i\beta_t d_0 e^{i(kL-\phi(L))} + i\beta_r c_0 e^{2i(kR+\phi(R))} \tag{74}$$

Now if we combine Eq.(73 & 74) via Eq.(68) we get an expression for the dark-port output of the interferometer.

$$B = \frac{1}{\sqrt{2}}\left(e^{i(kL+\phi(L))}\left((d_0-c_0)(1-l) + i\beta_t(d_0-c_0)\right) + \right. \tag{75}$$
$$\left. i\beta_r\left(c_0 e^{2i(kR+\phi(R))} - d_0 e^{2i(k(L-R)+\phi(L-R))}\right)\right) \tag{76}$$

From here we can plug in Eq.(65 & 66) for d_0 and c_0 and additionally substitute $R = L/2 + r$, where r is a small offset from the interferometer center position. This together with the fact that the Gouy-phase $\zeta(z)$ is antisymmetric gives the following result for the dark-port:

$$B = \frac{1}{2}e^{i(kL+\phi(L))}\left((l-1)b_0 - i\beta_t b_0\right) + \beta_r\left(2ib_0 cos(2(kr+\zeta(r))) + 2a_0\sin(2(kr+\zeta(r)))\right) \tag{77}$$

The same calculation for the bright-port gives the following result:

$$A = \frac{1}{2}e^{i(kL+\phi(L))}\left((1-l)a_0 + i\beta_t a_0\right) + \beta_r\left(2ib_0 sin(2(kr+\zeta(r))) + 2a_0\cos(2(kr+\zeta(r)))\right) \tag{78}$$

For no input at the dark-port ($b_0 = 0$) and the usage of $\lim_{z\to\infty} = \pi/2$ giving $\phi(L) \approx \pi/2$ these modes reduce to:

$$A = \frac{1}{2}a_0 e^{ikL}(i(1-l) - \beta_t) + a_0\beta_r\cos(2(kr+\zeta(r))) \tag{79}$$

$$B = -a_0\beta_r e^{ikL}\sin(2(kr+\zeta(r))) \tag{80}$$

What can be seen from this result is that in the case of no particle being present $\beta_{r/t} = 0$, the whole power leaves through the bright-port. Additionally, because of the separation of forward and backward scattered light through β_r and β_t it is now apparent that the only output at the dark-port stems from light scattered backwards by the particle. It has to be noted that the dark-port puts out no photons for the particle at the exact trap center, but a displacement of the particle yields a linear response through the backward scattered light.

2.5.4 Mode-matching of the dipole-field to a single mode fiber

As we have shown that there is a way to filter the back-scattered dipole radiation of the particle from the trapping light and create a particle position sensitive dark-port output we can now add one final signal to noise ratio increasing aspect to the detection scheme. The scattered dipole mode of the particle can be imaged to the mode of a single mode fiber. This yields two advantages: First, the mode matching with a local oscillator for subsequent homodyne detection is easily done in fibers and second, confocal filtering further suppresses stray photons without particle information from reaching the detection. This fiber based confocal dipole detection is theoretically described in [68] and applied in [8]. The following derivation will be a shortened version of the derivation for the confocal detection which can be seen in its entirety in [69].

The imaging system in question is depicted in Fig.(18). On the right side of the image in section 1, a particle radiates a dipole field $\boldsymbol{E}_1$ along the z direction. On the intersection to section 2 a lens of focal length f_1 collimates this field into the electric field $\boldsymbol{E}_2$, which is further focused at the border of section 3 through a lens of focal length f_3. The field $\boldsymbol{E}_3$ is then imaged onto the core of the fiber in the beam's focus.

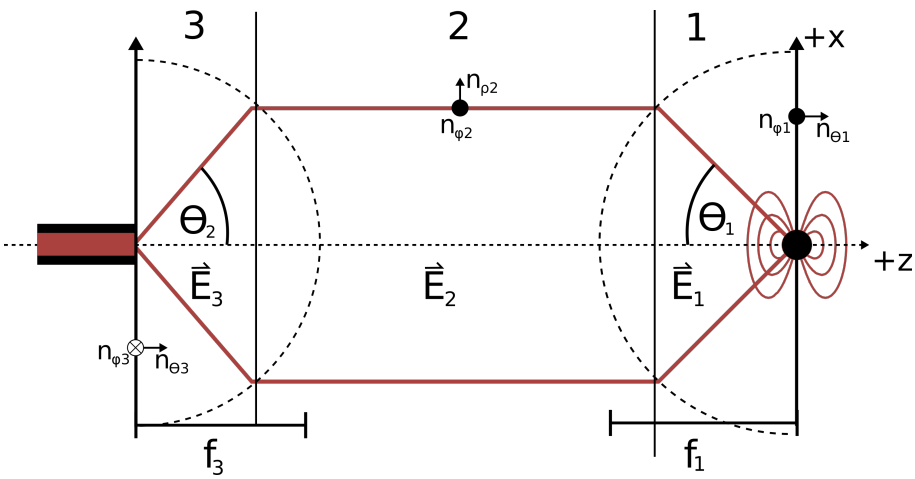

Figure 18: Confocal imaging system: The imaging system to map the dipole radiation of a levitated particle in section 1, onto a single mode fiber core in section 3. The system is defined by the magnification $M = f_3/f_1$ of the two lenses.

To figure out the optimal magnification $M = f_3/f_1$ we look at the photon collection efficiency of this system η_c which is the normalized mode overlap between the dipole field $\boldsymbol{E}_3$ and the principal mode of the single mode fiber $\boldsymbol{E}_{\text{fib}}$:

$$\eta_c(M) = \frac{|\int \boldsymbol{E}_3^*(\boldsymbol{r}_3, \boldsymbol{\delta r}) \boldsymbol{E}_{\text{fib}}^x(\boldsymbol{r}_3)\, dA_3|^2}{\int |\boldsymbol{E}_3^x(\boldsymbol{r}_3, \boldsymbol{\delta r} = 0)|^2\, dA_3 \cdot \int |\boldsymbol{E}_{\text{fib}}^x(\boldsymbol{r}_3)|^2\, dA_3} \tag{81}$$

In order to maximize this overlap for different magnification, we first have to get an expression for the dipole field in section $\boldsymbol{E}_3$. This derivation is only going to be schematic in nature. For the full derivation the references above are recommended.

The electric field at position $\boldsymbol{r}$ of such an induced dipole is given by [43]:

$$\boldsymbol{E}_1(\boldsymbol{r}, \boldsymbol{\delta r}) = \frac{\omega^2}{c\varepsilon_0} \boldsymbol{G}_\infty(\boldsymbol{r}, \boldsymbol{\delta r}) \cdot \boldsymbol{\mu} \tag{82}$$

Here $\boldsymbol{\delta r}$ is the dipole position, $\omega = 2\pi c/\lambda$ the angular frequency of light, $\boldsymbol{G}_\infty$ the dyadic Green's function in the far-field and $\boldsymbol{\mu}$ the particle's dipole moment $\boldsymbol{\mu} = \alpha \boldsymbol{E}$. This specific Green's function is given by:

$$\boldsymbol{G}_\infty(\boldsymbol{r}, \boldsymbol{\delta r}) = \frac{e^{ikR}}{4\pi R} \left(\mathbb{1} - \frac{\boldsymbol{RR}}{R^2} \right) \tag{83}$$

Where R is the absolute value of $\boldsymbol{R} = \boldsymbol{r} - \boldsymbol{\delta r}$ and $\boldsymbol{RR}$ denotes the outer product of these two vectors. switching to spherical coordinates this dyadic Green's function reads:

$$\boldsymbol{G}_\infty(\boldsymbol{r}, \boldsymbol{\delta r} = 0) = \frac{e^{ikr}}{4\pi r} \times \begin{pmatrix} 1 - \cos^2\varphi \sin^2\theta & -\sin\varphi\cos\theta\sin^2\theta & -\cos\varphi\sin\theta\cos\theta \\ -\sin\varphi\cos\varphi\sin^2\theta & 1 - \sin^2\varphi\sin^2\theta & -\sin\varphi\sin\theta\cos\theta \\ -\cos\varphi\sin\theta\cos\theta & -\sin\varphi\sin\theta\cos\theta & \sin^2\theta \end{pmatrix} \tag{84}$$

Plugging Eq.(84) into Eq.(82) gives the following expression (for a dipole oriented along $\boldsymbol{e}_x$):

$$\boldsymbol{E}_1(\boldsymbol{r}) = \frac{\omega^2 \mu_x}{4\pi c \varepsilon_0} \frac{\exp(i\boldsymbol{kr})}{r} \begin{pmatrix} 1 - \cos^2\varphi\sin^2\theta \\ -\sin\varphi\cos\theta\sin^2\theta \\ -\cos\varphi\sin\theta\cos\theta \end{pmatrix} \tag{85}$$

Here μ_x is the x-component of the dipole moment μ.

From there, unit mapping theory is used to first transform this field $\boldsymbol{E}_1$ after the refraction at the first lens from spherical coordinates to cylindrical coordinates. The collimated beam $\boldsymbol{E}_2$ described in cylindrical coordinates is refracted again (once more calculated through unit mapping theory) and the field is switched back to spherical coordinates. Finally utilizing angular spectrum representation the field is once more switched to cylindrical coordinates as the integration in Eq.(81) is calculated over the surface of a cylindrical fiber.
The dipole field $\boldsymbol{E}_3$ is then given by:

$$\boldsymbol{E}_3(\boldsymbol{r}, M) \;=\; C\mu_x \begin{pmatrix} \tilde{I}_{d0} + \tilde{I}_{d2}\cos(2\varphi_3) \\ \tilde{I}_{d2}\sin(2\varphi_3) \\ -2i\tilde{I}_{d1,2}\cos(\varphi_3) \end{pmatrix} \tag{86}$$

Where $C = ik^3\sqrt{n_1 n_3}\exp(if_1(k_1 - k_3 M))/(8\pi M\varepsilon_0)$ with n_i being the refractive indices of the media in section 1-3 and $k_i = n_i 2\pi/\lambda$ are the associated wavenumbers in the media (note: for us $n_i = 1$). The terms $\tilde{I}$ are integrals over Bessel functions and are defined as follows:

$$\tilde{I}_{d0} = \int_0^{\theta_1^{\max}} d\theta_1 f(\theta_1)(1+\cos(\theta_1)g(\theta_1))J_0\left(\frac{k_3\rho_3}{M}\sin\theta_1\right) \tag{87}$$

$$\tilde{I}_{d2} = \int_0^{\theta_1^{\max}} d\theta_1 f(\theta_1)(1-\cos(\theta_1)g(\theta_1))J_2\left(\frac{k_3\rho_3}{M}\sin\theta_1\right) \tag{88}$$

$$\tilde{I}_{d1,2} = \int_0^{\theta_1^{\max}} d\theta_1 f(\theta_1)\cos(\theta_1)\sin\theta_1 M^{-2}\, J_1\left(\frac{k_3\rho_3}{M}\sin\theta_1\right) \tag{89}$$

$$\tag{90}$$

And here in turn $f(\theta_1) = e^{ik_3z_3g(\theta_1)}\sqrt{\cos(\theta_1)/g(\theta_1)}\sin\theta_1$ and $g(\theta_1) = \sqrt{1-(\sin\theta_1/M)^2}$. J_i denotes the i-th order ordinary Bessel functions and $\theta_1^{\max}$ is the angle defined by the NA of the lens next to the dipole NA $= n_1\sin(\theta_1^{\max})$.

Now that we have the dipole mode defined we are only missing the fiber mode to evaluate Eq.(81). The fundamental fiber mode for a single mode fiber with core radius a is given by [70]:

$$\boldsymbol{E}^x_{\text{fib}}(\boldsymbol{r}, r) = \begin{cases} N\, J_0\left(\frac{u\rho}{a}\right) e^{i\beta z}\vec{n}_x & r \leq a \\ N\, \frac{J_0(u)}{K_0(w)} K_0\left(\frac{w\rho}{a}\right) e^{i\beta z}\vec{n}_x & r \geq a \end{cases} \tag{91}$$

Where N is a normalization constant, $u = \sqrt{n_{\text{co}}^2k^2 - \beta^2}$ and $w = a\sqrt{\beta^2 - n_{\text{cl}}^2k^2}$ are the transverse wave numbers with β the propagation constant, n_{co} and n_{cl} the refractive indices of the fiber core and the fiber cladding and K_l the l-th order modified Bessel function of the second kind. In order to find the transverse wave number one can use the fiber parameter $V^2 = u^2 + w^2 = 2\pi/\lambda a\text{NA}_{\text{fib}}$ with NA_{fib} the numerical aperture of the fiber.

Fig.(19A) shows the radial profile of the dipole field $\boldsymbol{E}_3$ of wavelength $\lambda = 1550\,\text{nm}$ for a trapping lens of NA $= 0.6$, a fiber mode with $\text{NA}_{\text{fib}} = 0.14$ and core radius $a = 4.1\,\mu\text{m}$. The magnification was set to $M = 6$ for this plot.

Now evaluate the integrals in Eq.(81) numerically for different magnifications M and get the graph from Fig.(19B). For this plot the same parameters as above were used and for different magnification the integral of the overlap (seen in graph A) is calculated. This means that the maximum collection efficiency for this imaging system is obtained for a magnification of $M \approx 4$ and yields a photon collection efficiency of $\eta = 0.68$.

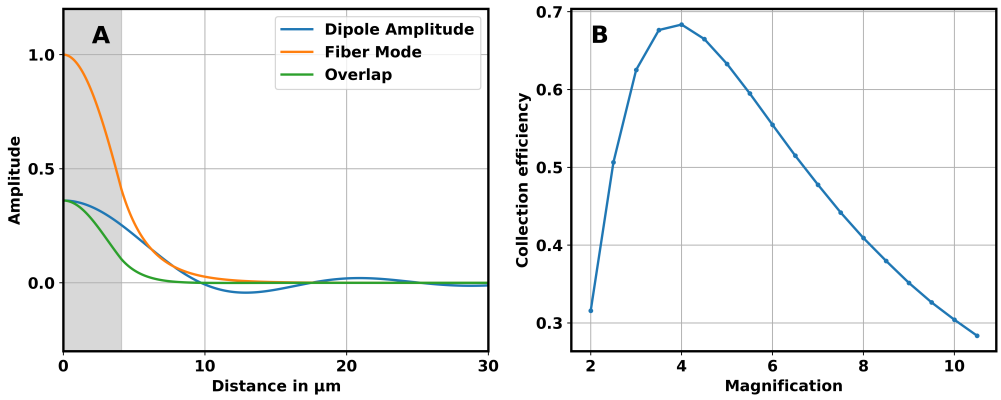

Figure 19: A) Modematching to a single-mode fiber: The amplitude of an imaged dipole $\boldsymbol{E}_3$ at the position of the collection fiber together with the amplitude of the fiber-mode itself and their overlap (all at $\varphi = 0$) is depicted. The fiber core is shown through the grey region. **B) Optimal magnification:** The photon collection efficiency for different magnifications at $\lambda = 1550\,\mathrm{nm}$ for a trapping lens with $\mathrm{NA} = 0.6$ into a single mode fiber of core radius $a = 4.1\,\mu\mathrm{m}$ with $\mathrm{NA}_{\mathrm{fib}} = 0.14$ is displayed. The maximum efficiency is found for a magnification of 4.

3 Optical trap in a Michelson-Sagnac interferometer

In this chapter of the thesis we will describe the first steps towards building a setup capable of producing interference patterns for levitated nanoparticles. The first section will give a general overview of the experimental layout and requirements, while the second section goes into more detail of the actual laboratory implementation, the individual components and a thorough description of a procedure on how to align the Sagnac interferometer the optical trap is located in.

3.1 Schematic setup

As discussed in section 1.2 the optical trap the levitated nanoparticles are confined in, consists of a standing wave beam. Fig.(20) depicts the schematics of the envisioned setup.

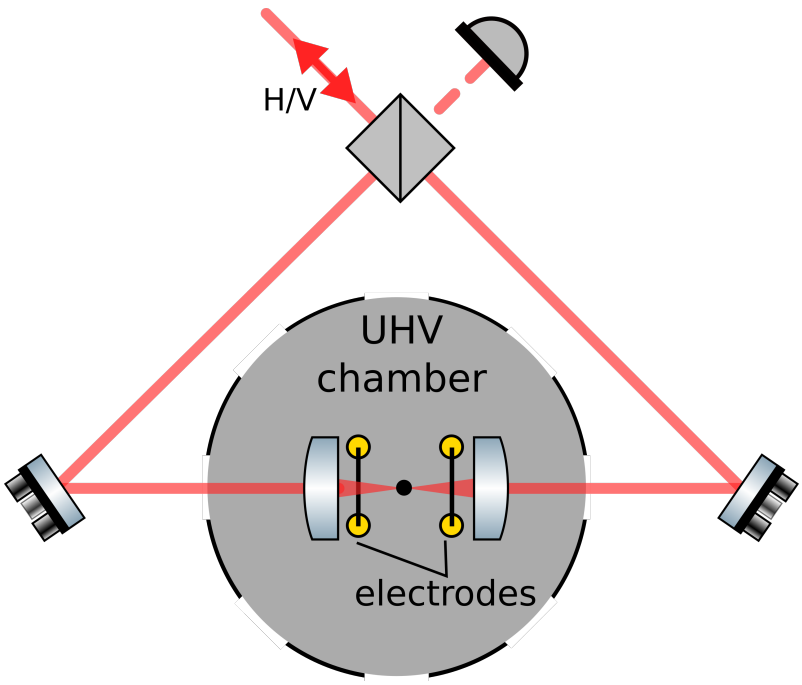

Figure 20: Schematic standing wave optical trap: The standing wave for the optical trap is created by splitting an incoming beam at a 50 : 50 BS. The two counter propagating beams are overlapped and guided into an UHV compatible vacuum chamber. In this chamber two high NA lenses focus the beams to create the optical trap. Two ring electrodes (in yellow) along the beampath are used to prepare the particle into the motional groundstate. The necessary detection efficiency is provided by a detection located at the dark-port of the beamsplitter (see section 2.5).

The optical trap in this experiment consists of two counter propagating $\lambda = 1550\,\mathrm{nm}$ beams focused down by two high numerical aperture (NA) lenses situated in an UHV compatible vacuum chamber. The two beams are created by a 50 : 50 beam splitter. This serves two purposes: first, overlapping the two beams forms the required standing

wave optical trap and second, the detection of the particle motion along the direction of the beam can be greatly enhanced through a Michelson-Sagnac dark-port detection as described in section 2.5.
A set of two ring electrodes (in yellow) located between the trapping-lenses is used to cool the axial motion of the particle down to its quantum ground state.
Additionally to the H-polarized beam that makes up the optical trap a second co-linear but orthogonally polarized beam can be added on top of first. This serves two purposes. On the one hand this second beam is used for parametric feedback cooling which is necessary to prevent particle losses below the viscous flow regime. On the other hand a fast switching from one polarization to the other will eventually allow to create a second, spatially shifted standing wave providing access to nonlinear components of the standing wave trap (see section 1.2).

3.2 Experimental setup

This section of the thesis will detail the steps taken to implement the setup envisioned for the experimental setup as described in section 1.2. For the sake of clarity we split the setup into three different parts: the beam-preparation where the necessary manipulation of the laser is performed to accommodate for the needed purposes, the optical trap where the actual trap within the vacuum chamber is described and the detection where the two different ways of detection are displayed.

Beam-preparation

Before the optical trap in the Sagnac interferometer can be formed, the laser light has to be manipulated in order to be able to perform all the needed tasks. In Fig.(21) this preparation steps are depicted.

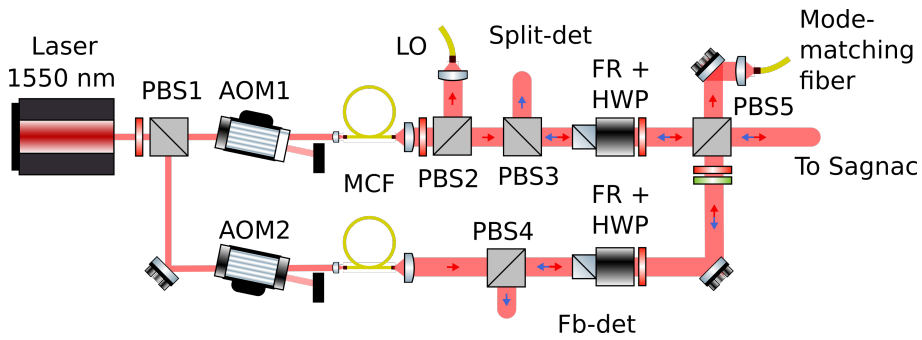

Figure 21: Beam preparation: A beam emitted by a 1550 nm laser source is split in a 80 : 20 ratio at a polarizing beam splitter (PBS1). The beams in the transmitted part (trapping arm) and the reflected arm (cooling arm) are impinged onto acousto-optic modulators (AOM1/2). The zeroth order diffraction is blocked on either side and the first orders are subsequently coupled into mode clearing fibers (MCF). A combination of Faraday rotators (FR) and half wave plates (HWP) is used to collect light that returns from the optical trap and is used for a split detection (PBS3) and feedback monitoring (PBS4). Finally the light in the trapping arm and the light from the cooling arm are recombined at PBS5 and directed towards the Sagnac interferometer.

A $\lambda = 1550\,\mathrm{nm}$ laser source (NKT "Koheras Adjustic") amplified by a fiber amplifier (NKT "Koheras BOOSTIK HP") serves as the light source in our experiment. This fiber amplifier emits a linearly polarized beam of waist $\omega_{01} = 1\,\mathrm{mm}$, that is split at the first polarizing beam splitter PBS1. The half wave plate before it (red rectangle in Fig.(21)) is used to set a splitting ratio of approximately 80% in transmitted horizontally polarized light and 20% in reflected vertically polarized light. The beam in the transmitted arm will later create the optical trap while the beam in the reflected arm is used for parametric feedback cooling. Thus the arms are henceforth called the trapping- and cooling-arm.
Starting in the trapping arm the beam passes through the first acousto-optic modulator (AOM1) which is driven at a center frequency of $\omega_{\mathrm{AO1}} = 2\pi \cdot 100\,\mathrm{MHz}$. This AOM is

utilized to switch between low and high trapping powers very quickly, which is needed for the triggering method discussed in chapter 4.3. The zeroth diffraction order of the AOM is blocked while the first order is further coupled to a single mode fiber. This single mode fiber (MCF for "mode cleaning fiber" in Fig.(21)) is used to restore a Gaussian beam shape as AOMs introduce ellipticities into a beam. The lens following the MCF is chosen in such a way, that the outgoing beam already has the right waist of $\omega_{02} = 1.7\,\mathrm{mm}$ to create the optical trap in the chamber. Thereafter a HWP and PBS2 are placed in such a way that they divert a small part of the beam for usage as a local oscillator signal in the homodyne detection of the particles motion. The next optical elements, namely PBS3, a Faraday rotator and one HWP are utilized to collect light that returns from the optical trap. Finally the H-polarized light transmits PBS5 towards the vacuum chamber.
Returning to the trapping arm where the V-polarized light is diffracted by AOM2 with a center frequency of $\omega_{\mathrm{AO2}} = 2\pi \cdot 100\,\mathrm{MHz}$. This AOM will further be used to modulate a more shallow optical trap on top of the main trap in order to cool the center of mass motion of the particle. The mode cleaning fiber, PBS4 the rotator and the HWP serve the exact same purpose as in the trapping arm with the one difference that the polarization coming back from the Sagnac interferometer is V.
At the position of PBS5 the two beams are recombined. By first coupling the trapping-arm into the mode cleaning fiber and then aligning the cooling-arm to the same fiber we assure that the two modes are well matched.
These two co-linear beams of equal size but orthogonal linear polarizations are thereafter sent towards the Michelson-Sagnac interferometer and the vacuum chamber.

Finally we take a look on the optics used to separate the forward and backward traveling beams through PBS2(3) the Faraday rotators and the HWPs (Fig.(22)): in the forward direction only H-polarized light transmits PBS3. This light is then turned by $+45°$ in the Faraday rotator to the "+"-state. From there the HWP can turn this polarization to any other linearly polarized state. Assuming the state after the HWP is set to H once again it will be transmitted by PBS5. When this horizontally polarized light returns from the Sagnac interferometer, it will transmit PBS5 and be rotated to the $|-\rangle$ state by the HWP. The Faraday rotator will once again turn it by $+45°$ which makes the beam end up in the V state before it returns to PBS3. There it is reflected to be used in a detection scheme.

Optical trap

Fig.(23) depicts the schematics of our optical trap within the Sagnac interferometer.
The two co-linear beams that were created in the beam preparation section are guided to the interferometer-constructing beamsplitter using two mirrors. The beamsplitter is set to a $50:50$ splitting ratio (for H-polarized light). Each beam is guided through the vacuum

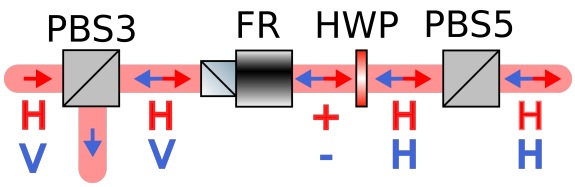

Figure 22: Beam separation by polarization: The polarization of the H-polarized light in the trapping-arm on its way to the setup in red and on its way back in blue. The V-polarized light is reflected at PBS3 to be used in the 3D split-detection.

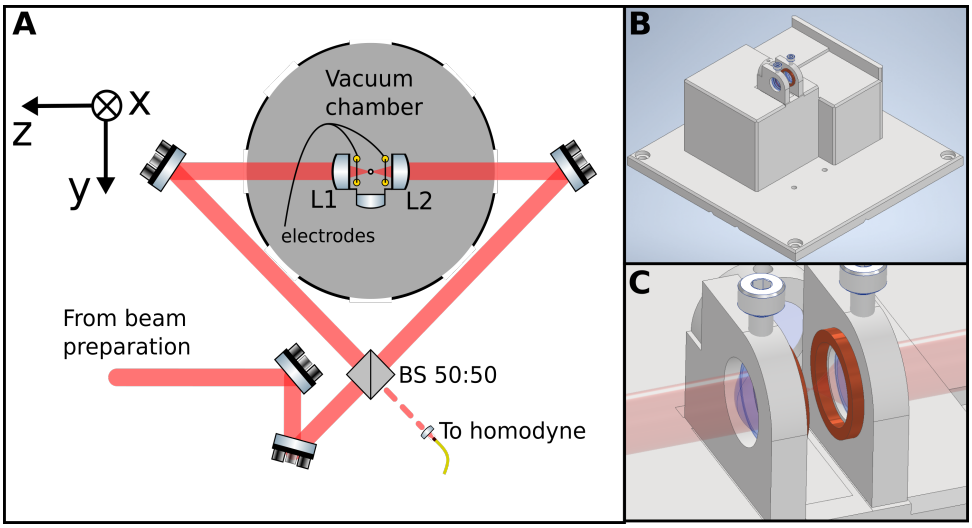

Figure 23: A) Schematics of the trap: The standing wave optical trap is created by splitting the incoming beam at a 50 : 50 beamsplitter. The counterpropagating beams are guided into the UHV compatible vacuum chamber where they are focused by two identical NA = 0.6 lenses. The dashed line indicates the dark-port of the interferometer for the advanced detection. A set of ring electrodes (here in yellow) are used for linear feedback cooling. These electrodes together with the lenses are mounted in a custom made lensholder. **B) Lensholder:** 3D model of the aluminum lensholder designed for the experiment. The lenses (in blue) are clamped into the holder through two screws on the top. **C) Zoom in:** Closer look onto the lensholder with a beam passing through it. The copper electrodes are also depicted.

chamber by use of another mirror. Inside the chamber two NA = 0.6 trapping lenses are mounted on a custom lensholder (see Fig.(23B & C)) separated by twice their focal lengths. Between those lenses the highly focused standing wave trap, where the particles are eventually confined, is formed. The incoming beam of waist $\omega_{01} = 1.7\,\mathrm{mm}$ is focused down to a trap waist of $\omega_{0t} = 1.15\,\mu\mathrm{m}$. These two NA = 0.6 trapping lenses are used for this first version of the experiment and will eventually be replaced by higher NA lenses. Also situated on the holder are two copper electrodes which are electrically isolated from the rest of the aluminum piece and are further utilized for the linear electric cooling.

Finally, situated at the dark-port, is the fiber for the confocal detection as described in chapter 2.5.3 and 2.5.4

The light exiting through the bright port is sent back to the beam preparation part where it is used for feedback monitoring and more importantly a 3D detection of the particle motion via split detection.

Detection

Finally, we will take a look at the two detection methods implemented in this setup, namely the split detection for the sensing of the particle motion along all three axis and the greatly enhanced back scattering detection in a homodyne scheme along the z-axis. Fig.(24) depicts the two detection schemes.

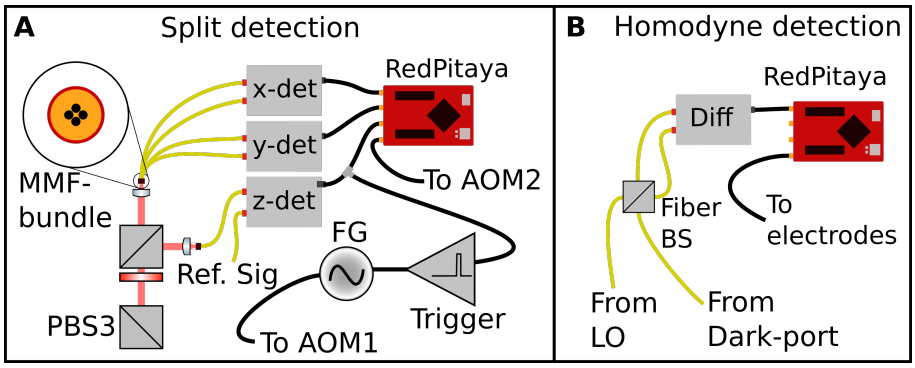

Figure 24: A) Split detection: The light reflected of PBS3 is split at another PBS to be used in the x,y and z split detection of the particle motion. The difference signals from all 3 detections are connected to (multiple) RedPitaya FPGAs (field programmable gate arrays) which are used to create a parametric feedback singal that is sent to AOM2 to modulate the cooling beam. An additional signal is sent towards an electrical trigger for fast switching of the trapping beam (see chapter 4.3). **B) Homodyne detection:** The in-fiber signals from both the local oscillator and the dark-port backscattering detection are mixed at a 50:50 fiber-beamsplitter. The output fibers are connected to a balanced photodetector. This difference voltage is used to create a linear feedback signal at a RedPitaya FPGA to perform feedback cooling via the electrodes located on the lensholder.

The H-polarized beam returning from the Sagnac bright-port is reflected by PBS3 (see Fig.(21)) to be used in the split detection. After PBS3 the beam is further split by a HWP and another PBS. The reflected part is coupled into a fiber which is connected to one port of a balance-photo diode. The other port of this diode is connected to a reference signal from the same laser that does not contain any light from the particle. The light transmitted by the beamsplitter is focused on a multimode fiberbundle (MMF-bundle) on which four fibers are combined in a cross like shape. The laser is impinged on this cross in such a way that all four fibers contain approximately the same amount of light. Now combining the top and the bottom fiber in one detector (x-detection) and the left and right fiber to the second one (y-detection) this gives the same result as a standard split detection performed through D-shaped mirrors. The difference signal from each photodetector is connected to a RedPitaya field programmable gate array (FPGA) that is used

as a phase lock loop (PLL) via the “PyRPL” package. The device creates a frequency doubled feedback signal as described in chapter 2.4.2 which is then summed up and fed back to the driver of AOM2 in order to modulate the trap. Additionally the difference signal from one of the detectors (in Fig.(24) z-deteciton) is also received by an electronic trigger that increases the intensity of the trapping laser upon the particle entry into the trap (see chapter 4.3).

The second part of Fig.(24) depicts the homodyne detection of the back scattered light for the greatly enhanced particle tracking along the axis of propagation of the trapping laser. The in-fiber signals from both local oscillator and dark-port enter a 50 : 50 fiber beamsplitter. Both of its outputs are further connected to a difference detector making up the homodyne detection. Depending on the phase relation between the local oscillator and the particle signal, either quadrature of the particle motion can be monitored. The output of the photodetector is once more connected to a RedPitaya which in turn creates the linear feedback voltage according to the particle signal from this homodyne detection. The electrical signal from the FPGA is directly connected to the electrodes inside the vacuum chamber to perform electric feedback. While the parametric feedback cooling is mainly performed to enable levitation at pressures below 10^{-3} mbar this linear feedback will be utilized to cool one of the motional degrees of freedom to a very low occupation or even the ground state.

3.3 Aligning the Sagnac interferometer

In chapter 2.5.3 the Michelson-Sagnac interferometer was established as a method to filter the light back-scattered by the particle from the rest of the trapping and cooling beam. There we treated the beamsplitter as a perfect 50 : 50 splitting device and also assumed that the beams in both directions are not distinguishable to ensure perfect interference at the light-/dark-port. In the real world application of this method there are several sources of imperfection that make the actual implementation stray from the optimized considerations and derivation done in the theory chapter.

Imperfect splitting of the beamsplitter, distortions of the wavefront, reflections on windows and optics, clipping of the beam and imperfect overlaps of the counterpropagating beams are the main contributions to this deviation. Left unchecked, these problems would amount to a substantial decrease in interference at the beamsplitter. This would henceforth give a less dark darkport, which in turn would decrease the signal to noise ratio in our axial detection of the particle motion. This section outlines the method to consistently align the Sagnac interferometer to maximize interference.

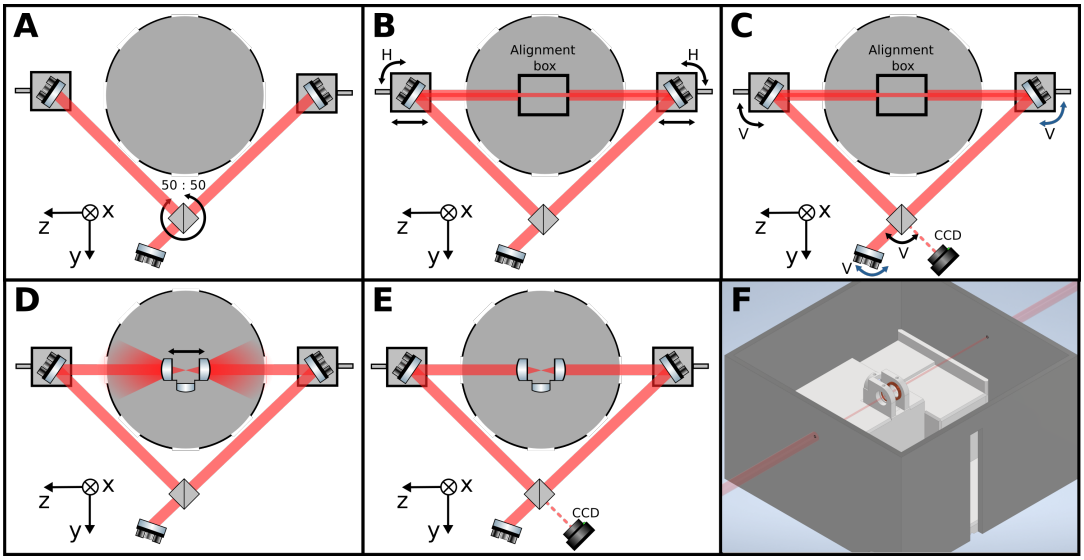

Figure 25: A)-E) Alignment procedure: The method devised to ensure maximal interference in the ports of the interferometer. **F) Alignment box:** A CNC-machined box to fit exactly over the lensholder (see Fig.(23B-C)). Two holes in its walls provide a straight line through the center position of the lenses.

Fig.(25A - E) depicts the individual steps performed to align the Sagnac interferometer. In the beginning of the process the lensholder from Fig.(23B - C) is already located in the vacuum chamber but the trapping lenses are not yet fixed to it. Fig.(25A) depicts the first step where the beam is pointed centrally to the beam splitter which is mounted on a five-axis stage to ensure enough degrees for the following alignment steps. By turning

the BS around the x-axis the splitting ratio is set to 50 : 50. Here it has to be noted that beam splitters do not have the same splitting ratios for all polarizations and here we align ours for H-polarized light. For the orthogonal polarization the splitting ratio was closer to 55 : 45. In both transmitted and reflected arms a mirror is placed on a translation stage that can move in the z-direction.

For step B a box was CNC-machined (see Fig.(23F)) to fit exactly over the lensholder in the vacuum chamber. The box has two 0.9 mm diameter holes in its side walls at the exact height and width where the center of the lenses will be located. Mounting this alignment box over the lensholder and placing a power measuring device behind the chamber allows deterministic alignment through the system. In step B the translation stages and horizontal tilting of the mirrors to the side of the chamber are used to roughly maximize the power transmitted through the box for both reflected and transmitted arm. This fixes the position of the mirrors in the Sagnac.

In step C for the transmitted arm the vertical tilting of the mirror before the beamsplitter together with the vertical tilt of the right mirror in the interferometer is used to find the vertical alignment through the box. For the reflected arm, the vertical tilt on the left mirror plus the tilting of the BS around the y-axis is used. As the first part of this alignment step slightly changes the position the beam hits the beamsplitter, this may result in a slight change in splitting ratio. If this is the case, the previous two steps have to be repeated iteratively. In most cases a single repeat suffices to regain the splitting ratio while keeping the alignment through the box. If the transmission through the box cannot be increased any more, the box can be removed and at that point a camera can be placed into the dark-port of the interferometer.

At this stage of the alignment the image produced by the camera will most likely still be a either a bright spot or a bright spot with interference fringes on it. By slightly tilting the mirrors to the side of the chamber thethe interference at the camera is maximized. Fig.(26A) depicts the darkport output after the initial alignment through the box and Fig.(26B) after the adjustment with the mirrors.

At this point the interferometer is aligned as well as it can be without the lenses, therefore in step D the lenses are mounted into the aluminum holder. We found that even though the working distance of our NA= 0.6 trapping lenses was specifically measured before the lensholder was designed and ordered, when the lenses were put into the holder, the beam passing through them was not collimated. The most likely source for this mismatch is due to the uncertainty of $\sim 150\,\mu$m for all distances in the CNC-machining process. In our specific case the beam would strongly diverge which implies that the lenses were too close together. The specific divergence angle θ_{div} is determined through two knife-edge waist measurements of the beam after the lenses. From the measured angle of $\theta_{\text{div}} = 0.81° \pm 0.02°$

we estimated the lenses to be too far apart by $\sim 300\,\mu$m through Gaussian beam propagation. In order to correct for this we placed shim rings between the lenses and the holder. These rings are available in different thicknesses down to $10\,\mu$m. By placing these rings into the holder the lenses are spaced further apart collimating the beams passing through both lenses.

From there the final step of the alignment depicted in Fig.(25E) is to check if the interferometer is still closed with the lenses in place. Usually a slight mismatch due to imperfect machining will be apparent. This can be eradicated by once again imaging the dark-port through the CCD camera and minimizing the intensity of the interference pattern. Fig.(26C) depicts the interference pattern attained after placing the lenses into the holder and Fig.(26D) after the adjustments were performed and the pattern is minimized. As can be seen the mode in Fig.(26C & D) is not perfectly Gaussian anymore. The imperfect interference pattern hints at missalignment either through the lenses or improper mounting of the lenses in the lensholder.

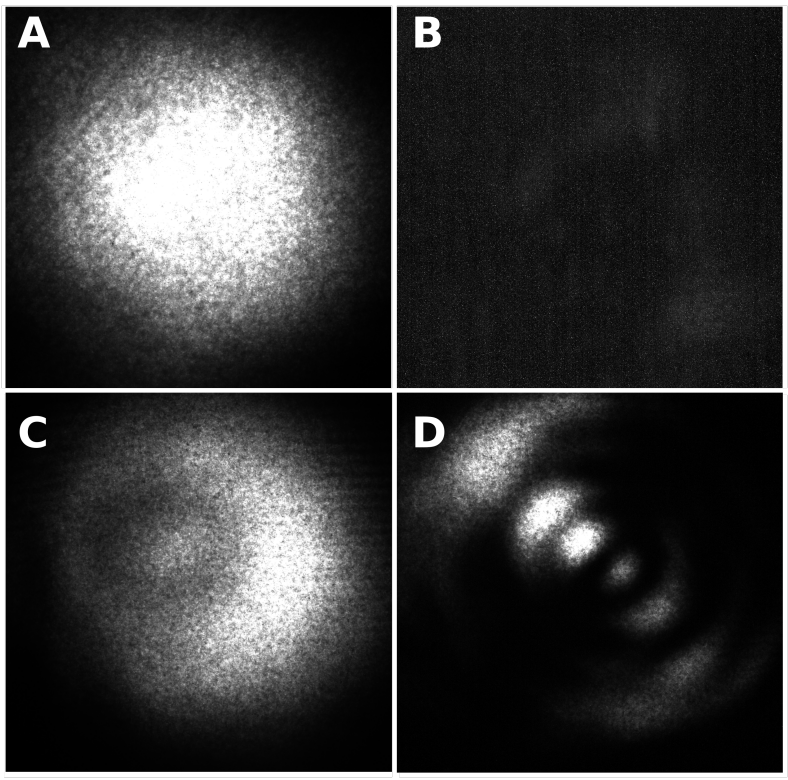

Figure 26: Visual impression of interferometer alignment A) Without lenses after alignment box: Image of the dark port intensity right after the final alignment through the box. **B) Without lenses after adjustment:** Image of the dark-port after slight adjustment with the mirrors to the side of the vacuum chamber. **C) With lenses:** Image of the dark-port mode after placing the trapping lenses into the holder. The mode is not uniform or Gaussian which hints at a missalignemnt of some sort. **C) With lenses after final optimization:** Image of the dark port after adjustments through the mirrors to the side of the vacuum chamber.

To quantify how well the interferometer is aligned the extinction ratio χ of the dark-port can be measured. We define this as the ratio between the power impinging on the BS P_{in} and the power measured in the dark-port P_{dp}. For a completely misaligned interferometer the extinction ratio is $\chi = 2$ as half of the input power leaves through the bright- and the other half through the dark-port. A perfect interferometer would have $\chi \to \infty$.
Here we measure the extinction ratio at two separate steps along the alignment process: once just before the lenses are placed into the chamber χ_1 and once at the very end of the alignment process χ_2. The first ratio χ_1 was measured right at the end of the first alignment without lenses:

$$\chi_1 = 98.4 \pm 5.2 \tag{92}$$

$$\tag{93}$$

An extinction ratio of ~ 100 is not very high. The origin of the excess light in the dark-port was found to be a back-reflection in the reflected arm of the interferometer, stemming from the right window of the vacuum chamber. When the reflected arm was blocked, the power in the dark-port dropped to almost zero while a blocked transmitted arm only decreased P_{dp} to less than a tenth of its original value. We conclude that this small fraction of light is the real dark-port power and most of the light detected is actually a reflection. From this we inferred the actual dark port intensity without the lenses in the holder:

$$\chi_1 = 2335 \pm 112 \tag{94}$$

$$\tag{95}$$

Once the lenses were inserted and the alignment procedure as described above was finalized the extinction ratio was measured again.

$$\chi_2 = 121.2 \pm 6.3 \tag{96}$$

To further infer what the actual power in the dark-port for this case was, a fiber was placed into the dark-port. By also placing a half-wave plate into one arm of the interferometer (and compensating for potential translations of the beam this might introduce) the interference at the beamsplitter can be actively suppressed. Doing this allows one to couple an almost Gaussian mode into the single-mode fiber. Once this light is coupled into the waveguide as well as possible, the wave plate is turned back to maximize the interference

and the power in the single mode fiber is measured. This way the relevant mode can be selected and measured. The extinction ratio χ_2 for this case reads:

$$\chi_2 = 3954 \pm 162 \tag{97}$$

The addition of this single mode fiber increased the extinction ratio substantially. Nonetheless as can be seen from the shape of the interference fringes in Fig.(26C & D) there is still room for improvements.

Discussion

Here we presented a setup capable of trapping a levitated nanoparticle in a standing wave optical trap located in an ultra high vacuum compatible chamber. Additionally the components and alignment of a greatly enhanced particle detection are presented. For a better understanding of its actual implementation Fig.(27) provides some visual impressions of the experiment.

We expect to need an increase in extinction ratio of another one or two orders of magnitude in order to perform a Heisenberg limited measurement of the particle position in the liking of [8].

Already at this stage we identify a few improvements concerning the Sagnac interferometer. Specifically the back-reflections by the current uncoated borosilicate windows mounted on a flange of the vacuum chamber. Exchanging these for wedged windows with an anti-reflectant (AR) coating for 1550 nm will undoubtedly improve the issue with the stray reflections. Additionally the current BS creating the Sagnac interferometer is an actual cube instead of a plate BS. It is still open for investigation whether this is a potential source of stray reflections.

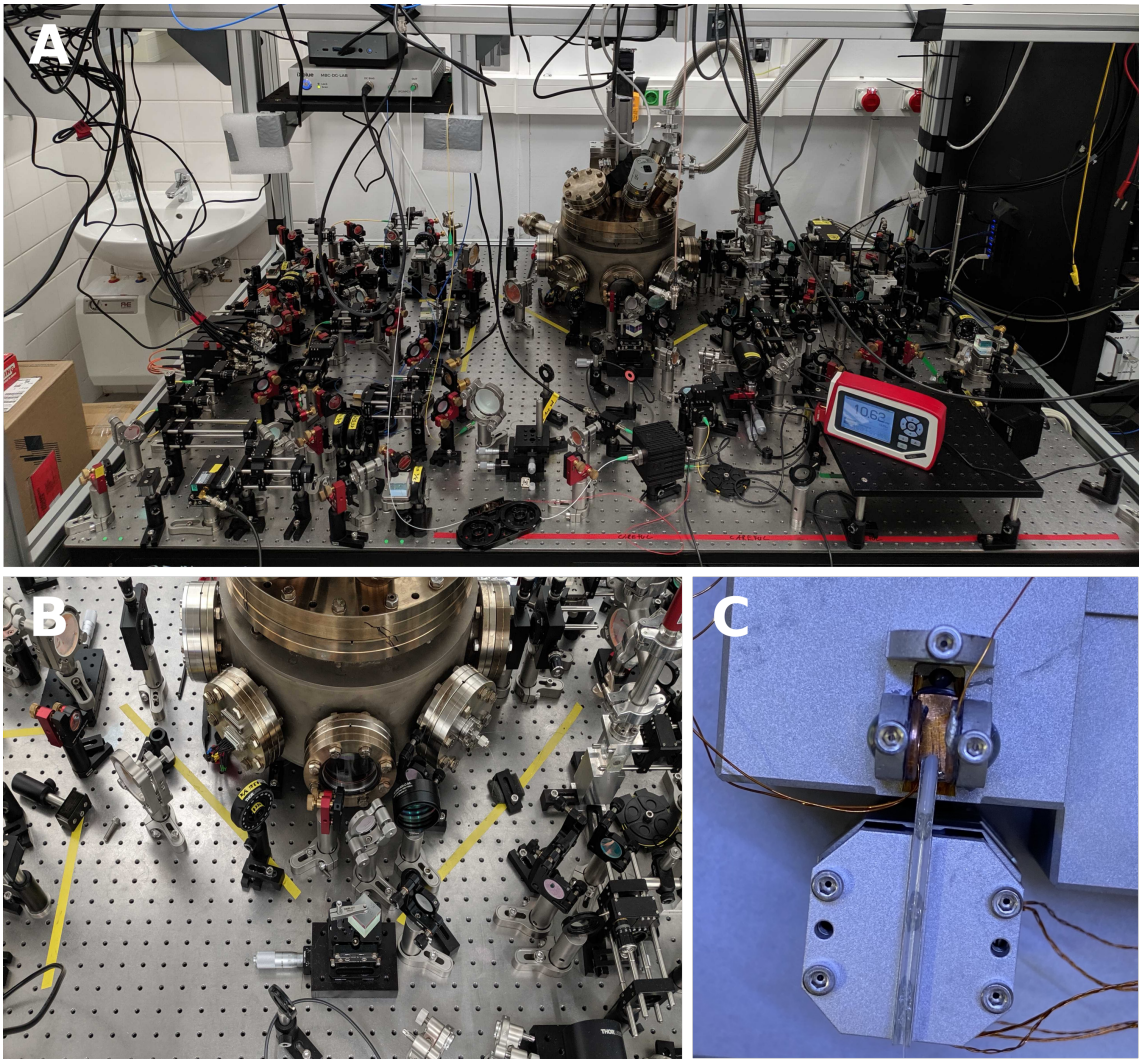

Figure 27: A) Entire optical setup: The complete setup on the optical table. In the center of the table the UHV chamber can be seen. **B) Sagnac interferometer:** A close-up of the Sagnac interferometer consisting of a cube beamsplitter and two mirrors is depicted. To the right the small loading chamber and very faintly the hollow core fiber and its feedthrough into the vacuum chamber can be seen. **C) Lensholder with piezostage and HCF:** A close up of the CNC-machined lensholder with the trapping lenses mounted and the cooling copper ring-electrodes glued to it is shown. Additionally the hollow core fiber on the three piezo stages which are highly relevant in the next chapter can be seen.

4 Hollow core fiber loading

In order to achieve UHV pressure levels and achieve coherence times on the order of several ms (see section 1.3), a new loading method is required. We have chosen to implement a particle loading scheme that uses hollow core fibers as particle conveyor belts. Previous work based on the groundwork of Philip Russel [71] and David Grass [42, 52] done by Jakob Rieser for his master thesis [16] saw successful transfers of nanoparticles from a hollow core fiber (HCF) conveyor belt to an optical trap at moderate vacuum conditions of $\sim 1\,\mathrm{mbar}$.
In this thesis we build up on the work in [16], extending the HCF transfer scheme to UHV. In particular we develop an alignment technique that does not require an a priori presence of a particle in the tweezer and an electric trigger. This chapter presents the general idea of HCF assisted loading and demonstrates how the updates to the scheme were developed and implemented.

4.1 HCF loading scheme

Hollow core photonic crystal fibers (HCPCF) or short hollow core fibers (HCF), in comparison to regular optical fibers, do not guide light on the principle of total internal refraction. Instead they do so, by a crystalline band-gap structure around the core that prevents light from leaking into the cladding [71, 72]. The fact that the light guiding region of these fibers is hollow, opens up the possibility to transport materials through them. This has previously been done to guide and trap ultra cold atoms [73, 74], move micrometer sized dielectric particles [75, 76] and transport and manipulate dielectric nanoparticels [42, 52]. In the latter reference a proposal to use a HCF as an optical conveyor belt to guide particles into optical traps at high vacuum conditions has already been made. In his master thesis Jakob Rieser demonstrated handovers of nanoparticles from the hollow core fiber conveyor belt to an optical tweezers at mild vacuum down to mbar pressures [16]. The schematic working principle of the particle deployment method is depicted in Fig.(28).

In this loading scheme a vacuum chamber (science chamber) containing the optical trap the nanoparticles are to be handed over to, is connected to a separate loading chamber through the hollow core fiber of length L. Connected to the loading chamber via a vacuum valve, an ultrasonic nebulizer is able to produce airborne particles. The hollow core fiber guides two counter-propagating beams of equal wavelength, creating a standing wave from one chamber to the other. Particles in the loading chamber coming from the nebulizer can be trapped in the intensity maxima of this standing wave and transported over long distances. While at each loading attempt the loading chamber will be sprayed with parti-

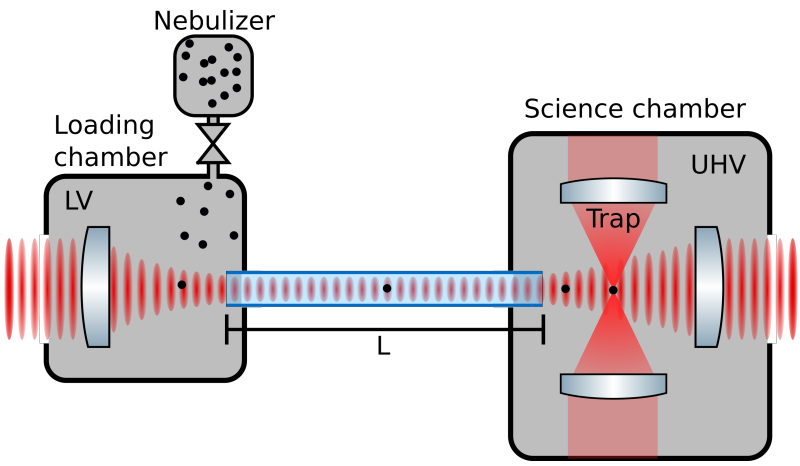

Figure 28: Hollow core fiber loading schematic: Two vacuum chambers are connected through a HCF guiding a standing wave. The science chamber with the optical trap is kept at UHV conditions, while the loading chamber is at a low vacuum pressures. A nebulizer connected to the loading chamber via a valve creates airborne particles. These particles are trapped in the standing wave intensity maxima and can be moved to the science chamber where they are deposited into the optical trap.

cles and has to go up to almost atmospheric pressures, the science chamber stays always clean and at high or even ultra high vacuum regimes.

As the fiber core is rather small in diameter (in the order of 10 μm) and the fiber can be rather long ($\sim$ 1-2 m) the eventual conductance from the high vacuum to the low vacuum chamber can be as small as $10^{-12}\,l/s$ [77] and thus does not impact the pressure ranges reachable for the science chamber.

Finally, mounting the end of the HCF located in the science chamber on a 3D translation stage, gives a precise control over where the particle is to be deposited, which is extremely relevant for aligning the whole scheme.

When operational, this loading technique provides a novel method allowing direct and deterministic loading of nanoparticles into optical traps without having to break the vacuum or contaminating the chamber. Therefore accessing loading to low UHV pressure regimes and with it collision free times of the particle going towards 10-100 ms.

4.1.1 Movable standing wave

In order to guide the nanoparticles from the loading chamber into the science chamber a method to move the intensity maximum of the standing wave deterministically is required. Here we present the method implemented in our setup:

The fundamental modes of light guided by hollow core photonic crystal fibers are well approximated with linearly polarized (LP_{mn}) modes [78]. Of these modes the fundamental and thus dominant one is the LP_{01} mode which has a 99% overlap with a TEM00 mode [79]. Thus the standing wave created by two counterpropagating beams guided into the

hollow core fiber can be approximated by the Gaussian standing wave intensity described in Eq.(17) or Eq.(18) in chapter 2.2. The high field seeking particles used in our experiments are trapped in the intensity maxima of this standing wave. In order to transport the particle along the fiber one of the two beams in the fiber has to be frequency-detuned with respect to the second beam. Looking at the interference term of the intensity distribution we get the following expression:

$$I \propto |e^{(i(kz-2\pi\nu t))} + e^{(i(kz-2\pi(\nu+\Delta)t))}|^2 \tag{98}$$

$$= 2\cos^2(kz + \pi\Delta t) \tag{99}$$

The particle will always follow the intensity maximum, i.e. where $kz + \pi\Delta t = 0$. For $\Delta = 0$ this will be at $z = 0$ but as soon as $\Delta \neq 0$ we get a time dependent position for the trap center $z = \frac{\pi\Delta t}{k}$ and a velocity of this maximum of:

$$v = \frac{dz}{dt} = \frac{\lambda\Delta}{2} \tag{100}$$

So depending on the frequency detuning the intensity maxima and thus the particle trapped within are moved along the fiber at varying speeds. A particle in a standing wave generated by a $\lambda = 1064\,\mathrm{nm}$ laser with one of the beams detuned by $\Delta = 10\,\mathrm{kHz}$ moves at a velocity of $v \approx 5\,\frac{\mathrm{mm}}{\mathrm{s}}$.
Fig.(29) depicts the schematic lab implementation of this movement. The detuning of one of the beams with respect to the second is accomplished through two acousto optic modulators, both of which are driven by the same RF power supply. Changing the driving frequency of one of the AOMs will lead to the required detuning to move the standing wave.

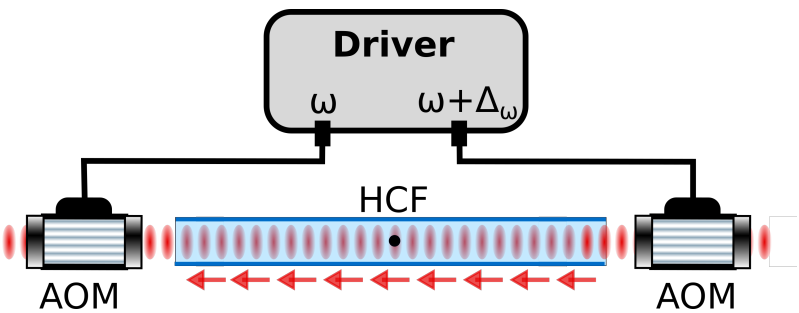

Figure 29: Movement of the standing wave: The two counter-propagating beams making up the standing wave inside the HCF pass through one acousto optic modulator (AOM) each. These modulators are driven by an RF signal generator that can frequency detune its outputs separately. The speed at which the standing wave moves is dependent on the value of $\Delta_\omega = 2\pi\Delta$.

4.2 HCF alignment procedure

Positioning the loading fiber well with respect to the optical trap is of utmost importance in order to successfully hand over particles. Misalignment by more than half the optical trap width can already mean that loading through the fiber is not achievable anymore. In order to clarify what optimal position means, Fig.(30) displays the schematics of the HCF and the standing wave optical trap.

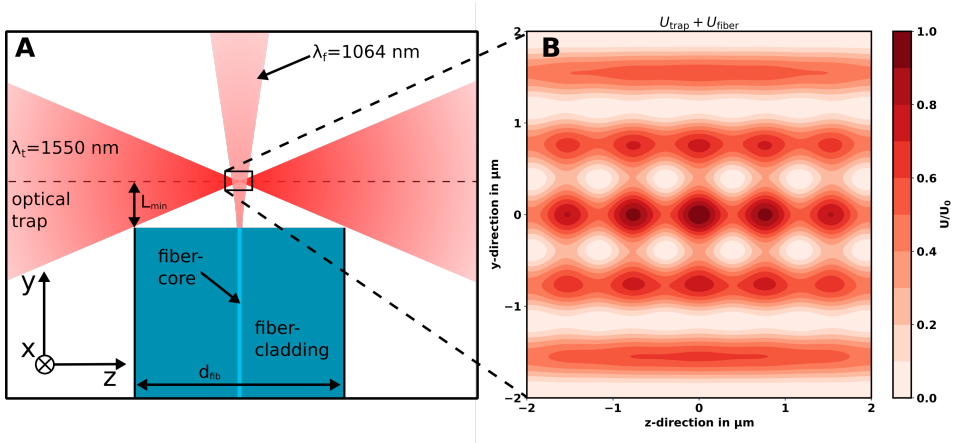

Figure 30: A) Optimal HCF position: The HCF (in blue) is positioned centrally with respect to the optical trap propagating along the z-direction. In the y-direction the closest position the fiber can approach the trap, without clipping the trapping beam, is determined by the divergence of the trap and the width of the hollow core fiber. **B) Overlapping standing waves:** At the position of the particle ($z = 0$, $y = 0$) the tweezer standing wave (along z with $\lambda_t = 1550\,\text{nm}$) and the hollow core standing wave (along y with $\lambda_f = 1064\,\text{nm}$) overlap. With the fiber at a distance of $L_{\text{min}} = 40\,\mu\text{m}$ the waist of the fiber trap at the tweezer standing wave actually spans over a range of ~ 40 intensity maxima.

Fig.(30A) shows a close up of the experiment. The HCF, shown in blue is positioned along the y direction. The $\lambda_f = 1064\,\text{nm}$ beams guided by it travel in the $\pm y$-direction and make up the standing wave of the optical conveyor belt. The $\lambda_t = 1550\,\text{nm}$ standing wave that the particle is to be handed over to consists of two beams traveling in the $\pm z$-direction. The optimal fiber positions for the x and z directions are determined through overlapping the waist of the optical trap with the center of the fiber core. In the y-direction, the trap geometry constraints the closest distance the fiber can be positioned to the waist of the trap before it starts to block the beam on either side (L_{min}). For our case of a fiber-(cladding) diameter $d_{\text{fib}} \approx 125\,\mu\text{m}$ and a trapping numerical aperture of NA $= 0.6$ this minimal distance is given by $L_{\text{min}} \approx 40\,\mu\text{m}$.

Fig.(30B) shows the two overlapping standing waves traveling along y and z. The depicted graph is for a tweezer standing wave power of $P_t = 0.1\,\text{W}$ and hollow core fiber standing wave power of $P_f = 2\,\text{W}$. The distance $L_{\text{min}} = 40\,\mu\text{m}$ between the fiber and the tweezer-waist makes the fiber-optical-trap expand substantially and at the position of the

tweezer-trap the waist of the 1064 nm beam already covers ~ 40 intensity maxima. It has to be noted that only the central intensity maxima of the tweezer trap are relevant because the depth of the potential falls off with a Lorentzian shape in the axial direction.

The method to align the HCF to the optical trap developed in [16] enables positioning of the fiber with accuracy of $\sim 1\,\mu$m to the tweezer. This is sufficient to successfully transfer the particle to the trap. The big downside of this positioning scheme and the reason why there is need for an updated method, is that in order to align the fiber, a particle already has to be trapped in the optical tweezer. This particle is illuminated by a modulated beam from the HCF. Radiation pressure induces momentum kicks of the particle and by maximizing the visible displacement originating from this interaction, one can position the fiber to the trapped particle and thus the trap itself. In order to load this first "alignment" particle, an ultrasonic nebulizer was used to get particles in an isopropanol solution airborne and into the chamber. As discussed in chapter 1.4 the usage of such nebulizers deeply impacts the base pressure reachable by the vacuum system through contamination of the chamber walls. These contaminants can not not be pumped by vacuum pumps making this alignment method not compatible with an experiment aiming for pressures in the UHV regime.

The method to align the HCF to the optical trap presented in this work does not rely on a particle being trapped initially and thus makes this procedure UHV compatible.

4.2.1 Two stage auto-alignment

Fig.(31) depicts the underlying idea that enables a clean procedure of aligning the fiber to the optical trap.
As in [16], the hollow core fiber inside the vacuum chamber is mounted on a 3D-translation stage seen in the figure to the left. The fiber emits a beam that is collimated by a fixed lens inside the vacuum chamber. A second lens on the outside of equal focal length focuses the beam down onto a second fiber, mounted on another 3D-translation stage. This fiber also emits a beam of light to create the standing wave required for the particle transport in and outside the HCF.
If the stage on the inside is now displaced in the z (or x) direction by d, the beam emitted by the HCF is redirected at the first lens and the second lens will focus it again at a different spot than before. As this imaging system is a $1:1$ system the displacement the focal spot has with respect to the optical axis is also d. If the second stage is now moved to this focal spot, the coupling in both fibers will be restored.
If these steps (movement of the inner stage - recovery of the outer stage) are done in small increments, so that the coupling into neither fiber gets too low, one has established a way

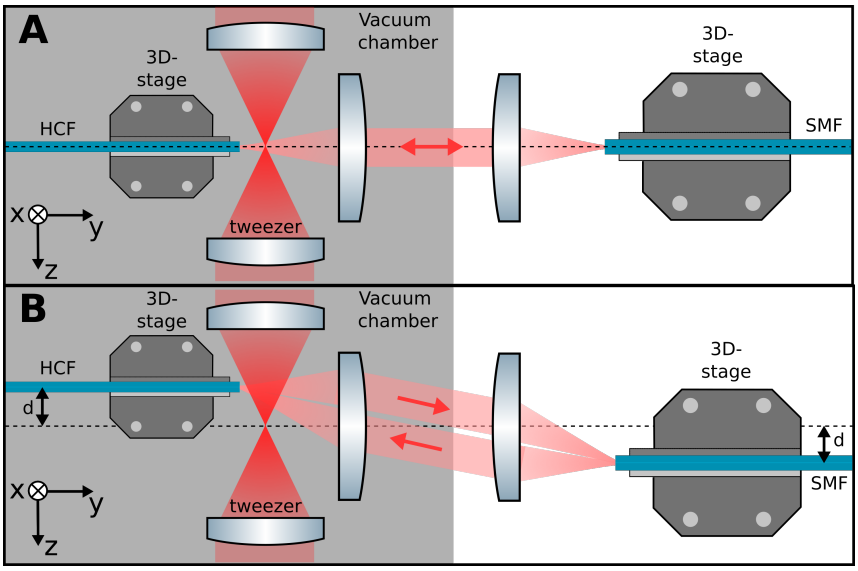

Figure 31: A) HCF alignment principle: The hollow core fiber (to the left) is mounted on a 3D - piezo translation stage. The light exiting the fiber is collimated on the first lens still inside the vacuum chamber (represented by the grey area). Outside the chamber a second lens (of equal focal length) is focusing the light onto another fiber (of similar mode field diameter) which again is located on a 3D-piezo translation stage. The double sided arrow in the middle signifies that the there is also a beam exiting from the fiber to the right creating the standing wave. **B)** The stage on the inside is displaced by d along the z direction. This creates an offset beam and a displacement in the image-plane of the second fiber. As this is a $1:1$ optical system, the beam coupling into the second fiber can be regained by moving the second stage by $-d$ in the z direction. The same thing applies for the beam emitted by the left fiber.

how to safely move the hollow core fiber without loosing coupling. This opens up two possible methods to align the fiber to the optical trap.

1. **Scan and shoot:** With the coupling into the HCF stable and thus the standing wave inside and in front of the fiber active while moving the stage it is easy to scan an area of possible correct positions with the piezo stage in the chamber. Previously, whenever the position of the fiber was changed, light from the outside had to be re-coupled into the HCF by hand. This meant that it was impossible to keep particles in the fiber during these movements. The updated alignment process starts by finding the correct distance to the trap in the y-direction, which can be determined by monitoring light scattered off the fiber through a camera when moving the fiber in and out of the tweezer standing wave. Once the HCF is in an acceptable position in the y-direction, it is loaded with particles and a search pattern (i.e. a square) is initiated. For each step a couple of particles are ejected from the fiber while the detection of the tweezer light is monitored. If a particle is to pass through

the trap, the detection will output a signal. The closer the particle passes through the intensity maximum of the trap, the bigger this signal will be. After shooting a couple of particles the stage is moved by a small increment and the previous step is repeated. This can initially be done in a fixed big pattern like a square with wide steps and once the general direction of the trap center is located, be repeated in smaller steps to increase the precision and pinpoint the trap center.

2. **Direct deposition:** As discussed in [42], a particle trapped on the outside of the hollow core fiber in combination with this fiber being mobile would make up the ideal way to position the particle to an optical trap. In the same work and in [16] particles are stably levitated extending $100 - 200\,\mu$m outside the hollow core fiber. Assuming the automatic alignment manages to hold the standing wave stable enough, the particle can be moved while it is levitated in front of the fiber. Movement of the particle through the optical trap will again be picked up by the detection. The closer the particle is to the trap center, the bigger the signal at the detection will be. This way the particle can directly be deposited into the optical trap once this maximum is found and the HCF is aligned for future loading attempts.

4.2.2 Automatic alignment algorithm

Having established that an automatic fiber alignment system will open up the possibility to align the HCF to the standing wave trap we have to address the fact that Fig.(31) is a simplification. While it is true that in a perfect $1:1$ system a displacement of one stage leads to the same displacement at the second stage, in an actual implementation the possibility for deviations from this optimal mapping is very real. Imperfection in the position readout, repeatability and precision of the translation stages make a calibration, monitoring and feedback system a requirement in order to position the stages correctly and keep the coupling stable. Here we present our envisioned method for the co-movement of the stages without destroying the standing wave. As the inner stage is moved in order to find the maximum of the $\lambda_t = 1550\,\text{nm}$ trap, all the recovering steps described in the following section concern the outer stage. The algorithm is applied in two steps: first a predicted recovering move reliant on a calibration done before the experimental run and second an automated algorithm for fine tuning. Wilfried Philip has successfully implemented the control software of the stages in the course of his bachelor thesis [80].

Movement according to recorded mapping

In an optimal system of these two stages for every one of the $i = 0, ..., N$ (x-y)-position (x_i^1, z_i^1) of the inner stage, there is an optimal position (x_i^2, z_i^2) of the outer stage to recover the most light into it. The light coupled into the HCF is monitored at a detector allowing a real-time check of the alignment of the stages. In order to find a mapping that relates

(x_i^1, z_i^1) to (x_i^2, z_i^2) a calibration measurement in 4 dimensions can be performed. The inner stage scans positions in a certain range in x and z and for each position (x_i^1, z_i^1) a separate scan of the outer stage is performed. In these outer scans the position of the intensity maximum (x_i^2, z_i^2) can be found. From here there are two possible options. Either this correspondence is directly used to relate one maximum to the other, or an approach using first differences in the manner described in [80] is used.
The latter method relates the first differences $(\Delta x_i = x_i - x_{i-1})$ of the inner stage maxima positions $(\Delta x_i^1, \Delta z_i^1)$ to the outer stage first differences $(\Delta x_i^2, \Delta z_i^2)$ through this linear system:

$$\begin{pmatrix} \Delta x_i^2 \\ \Delta z_i^2 \end{pmatrix} = \begin{pmatrix} a_{xx} & a_{xz} \\ a_{zx} & a_{zz} \end{pmatrix} \begin{pmatrix} \Delta x_i^1 \\ \Delta z_i^1 \end{pmatrix} \tag{101}$$

Solving this linear system and retrieving the entries of this matrix allows the prediction of the outer stage movement for any given inner stage positioning. In the optimal case this matrix $\boldsymbol{A}$ is the unity matrix which would signify a perfect $1:1$ correspondence from one stage to the other. Measurement uncertainties in the stage position, fluctuation in the laser intensity, a mismatch in the axis of the stages and non-linearities in the stage movements (jumps) will lead to the deviation from this optimal case. Any deviation from the perfect estimation will inevitably lead to the situation that the intensity after any predicted step of the outer stage will not maximize the power into the HCF perfectly. For this reason, an additional feedback step through a maximization algorithm is performed.

Automatic fine tuning algorithm

In order to re-couple the maximum amount of light into the fiber, the center of the fiber core has to overlap with the intensity maximum of the Gaussian mode of the incoming light-field. Fig.(32) displays the schematic working principle of one complete run of the recovering algorithm.
Graph A starts with the beam not perfectly aligned after the step performed through the mapping as described above. The fiber core is offset from the intensity maximum, indicated by the blue cross. The first step performed in graph B is a small movement of length δ along the -z-direction. Here the intensity is noted, and a step of length 2δ in the opposite direction (graph C) is performed. The intensity is once again recorded and compared to the one noted in graph B. As a zeroth order Gaussian beam only has one intensity maximum moving the stage in the direction of the higher recorded value will move the fiber core closer to the actual maximum. The movement in D is of arbitrary length but long enough to see an increase and decrease in the intensity. During this whole motion

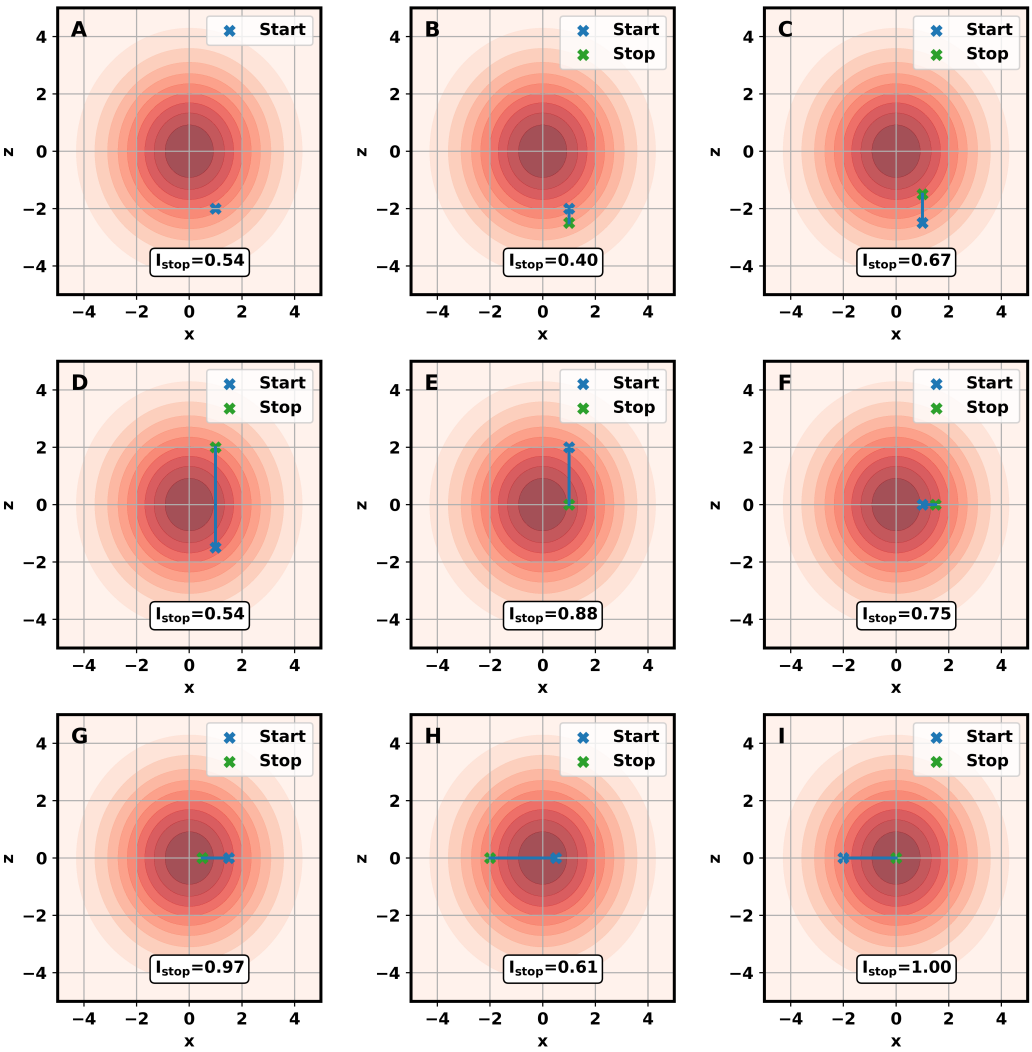

Figure 32: Alignment algorithm: Graphs **A)-I)** display one full cycle in the alignment algorithm. The Gaussian mode central to every graph represents the beam that has to remain coupled or has to be re-coupled into the fiber. The green and blue crosses signify the starting and stopping position for each step of the algorithm. Additionally on the bottom of each Graph I_{stop} the (normalized) intensity for the Gaussian mode is given. All the units are kept arbitrary.

the intensity is monitored and mapped to the position of the stage. After the movement is done, the stage positions itself to the location of the highest intensity (graph E). In the case of an optimal incoming Gaussian beam this means that the z-direction is now aligned. The scheme is repeated for the y-direction and after only two sets of movements the intensity maximum is reached again.

This algorithm gives a simple way to find the maximum of a function with no other local maximas, but of course in the actual implementation several details need further attention. The size of the checking step δ (done in graphs B, C, F and G) to determine in which

direction the intensity increases, is an essential parameter for the success of this method. For a perfect Gaussian intensity δ can be arbitrarily small and the algorithm will still find the maximum. In an actual intensity distribution created by a laser, picked up by a fiber and measured by a photodetector this does not apply. The signal recorded at the photodiode will have a noise contribution on it and if δ is too small the checking step might result in movement in the wrong direction. The same holds for the case when the fiber core is already close to the intensity maximum. There, the change of intensity is the smallest for a given movement in either direction, so the possibility for an error is likely. If, on the other hand the checking step δ is too big the risk of loosing excessive amounts of coupling into the HCF is very real.
To circumvent these problems a variable checking step width $\delta(I/I_{\max})$ dependent on the normalized intensity before each set of checking steps can be implemented. This way steps close to the maximum can be larger than the ones further away from it.
In an actual implementation, the initial step by the leading stage can not exceed a certain length for the same reason as before, as the standing wave intensity in the fiber would drop drastically. Finally in the real world application it usually takes more then 2 sets of steps to find the maximum. If the incoming Gaussian beam is not exactly circular and has a slight ellipitcity to it, the algorithm will zig-zag towards the maximum in more than two steps.

4.2.3 Experimental setup for the HCF alignemnt

Having established the principle of the HCF alignment, this section will give an overview of the experimental realization. Fig.(33) shows the scheme of the HCF loading setup.
A $\lambda_f = 1064\,\mathrm{nm}$ laser (Azurlight "ASL Fiber Laser" at power $P = 3\,\mathrm{W}$ as used in [81]) is split in a 50 : 50 ratio at a HWP-PBS combination. From here we go counterclockwise: The beam passes through AOM2 which is driven at a center-frequency of $\omega_{\mathrm{AO}_2} = 80\,\mathrm{MHz}$ with the zeroth order being blocked and the first order coupled into a single mode fiber. The other end of this $\sim 1\,\mathrm{m}$ fiber is mounted on a set of 3 linear piezo translation stages (Attocube "ESC3030"). The beam emitted by the fiber is then collimated by a lens, passes through a HWP and a 1 : 1 telescope. This telescope was omitted from the discussion in the previous section but changes nothing of the premise as the 1 : 1 imaging still holes. The telescope is used to control the collimation of the beam and helps coupling into the HCF. Using 2 mirrors, the beam is coupled into the HCF mounted on the second trio of piezo stages (Attocubes "ANPx/z101") located in the vacuum chamber. The lens used to focus the beam into the hollow core fiber is mounted in the same lensholder the two trapping lenses from Fig.(23) are held by. The hollow core fiber exits the vacuum chamber through a fiber-feedthrough and is mounted inside the loading chamber (L-C).

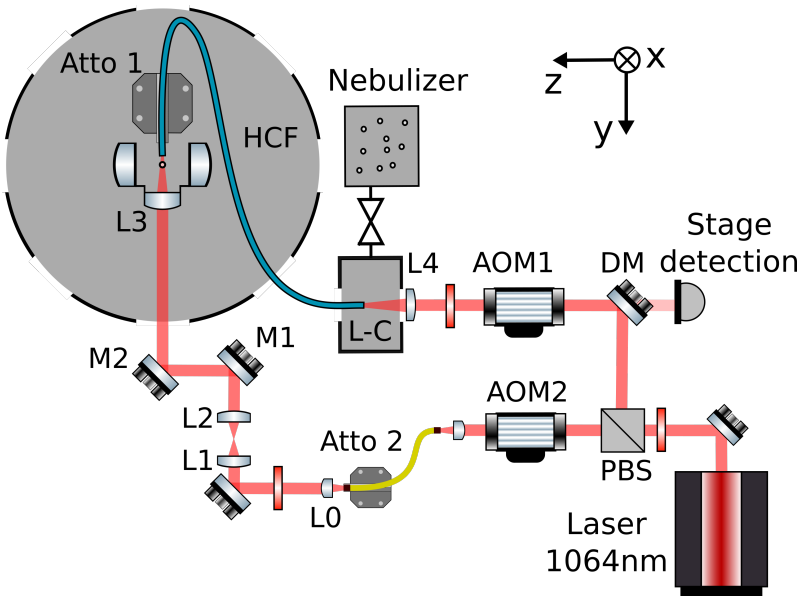

Figure 33: Hollow core fiber loading: The hollow core fiber conveyor belt is created by two counter-propagating beams from a $\lambda = 1064\,\text{nm}$ laser. The two beams are created by splitting at a PBS. Both beams pass through AOMs which enable to set the detuning needed to transport the nanoparticles. One of the beams is coupled into a single mode fiber which is mounted on a piezo translation stage (Atto 2). Together with a translation stage on the inside (Atto 1), to which the hollow core fiber is mounted to, this creates the alignment system discussed in the previous chapters. The intensity detection needed for the protocol is taken through a dichroic mirror (DM). The hollow core fiber itself is mounted in the loading chamber (L-C) which in term is connected to an ultrasonic nebulizer.

This loading chamber is connected to an ultrasonic nebulizer via a vacuum valve. The beam emitted by the hollow core fiber is then collimated by lens L4, passes through another HWP and AOM1 (also driven at $\omega_{\text{AO}_1} = 80\,\text{MHz}$) and is partially reflected by a dichroic mirror (DM) to close the loop at the PBS. The light transmitted through the dichroic mirror is used to track the amount of light coupled to the hollow core fiber, used for the alignment algorithm. The clockwise beam propagates along the same path but in the reverse direction.

With the concepts now explained, the next chapter provides the result of initial testing of the this system, realizations from it and the appropriate measures taken together with the resulting improvement.

4.2.4 Initial testing of the alignment procedure

Prior to the first tests with actual particles in the HCF, the working regime of the alignment procedure was tested to prevent the loss of particles in the fiber. These tests were conducted by performing scans of the mode exciting the single mode fiber on Atto 2 (seeFig.(33)) for various positions of Atto 1. For a fixed position of Atto 1 the fiber on

Atto 2 was moved in a square of approximately $20 \times 20\,\mu$m with a stepsize of $\sim 500\,$nm while recording the coupled power. Fig.(34) shows the recorded normalized intensity profile of one scan.

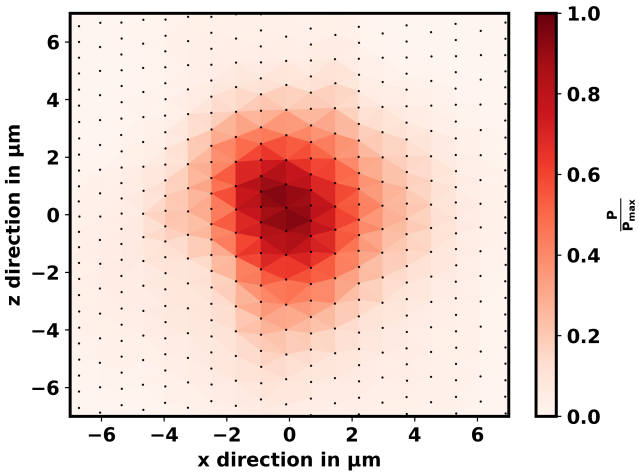

Figure 34: Initial scan of mode profile into the HCF: The Gaussian mode profile aquired by scanning the single mode fiber on Atto 2 while recording the light coupled into the HCF. Each black dot represents one data point and the red color indicates the recorded intensity.

As expected the intensity profile has the Gaussian shape of the beam exciting the single mode fiber. When fitting this with a Gaussian intensity profile we get a waist in the x-direction for $\omega_{0x} = 4.05 \pm 0.01\,\mu$m and in the z direction $\omega_{0x} = 4.89 \pm 0.14\,\mu$m. This is in acceptable agreement with the mode field diameter of mfd$= 6.6\,\mu$m of the hollow core fiber.

After this initial scan the position of Atto 1 was changed in $\sim 6\,\mu$m increments in the x direction and the scanning process from above was repeated. For each scan the maximally coupled intensity was recorded and is plotted in Fig.(35).

This plot displays an issue in implementation proposed in the previous chapter. The maximum intensity that can be coupled into the fiber, and thus also power the standing wave trapping the particles in it, is highly dependent on the position of the HCF and not uniform as envisioned. Here we will give an explanation for why this problem arises.

The angles accepted into the guiding mode of any fiber are defined by its numerical aperture. If either the beam is focused too strongly onto the fiber or the angle of incidence exceeds these angles, the amount of light that can be coupled into the fiber reduces. Fig.(36) depicts a ray transfer analysis of our optics system in place.

Two sets of beams emitted by the single mode fiber to the left are displayed. The black one shows the rays for a fiber located in the center of the setup while the red beam is

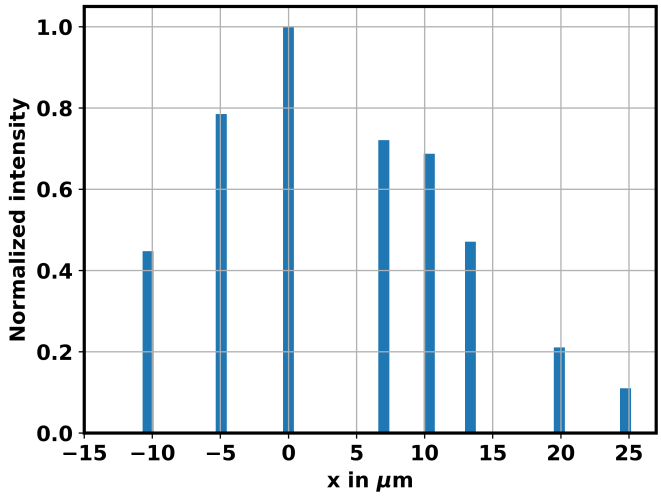

Figure 35: Maximal intensities for different Atto 1 positions: For different positions of Atto 1 along the x directions scans were repeated and the maximal coupled intensity (normalized to the intensity maximum from the scan in Fig.(34)) is depicted.

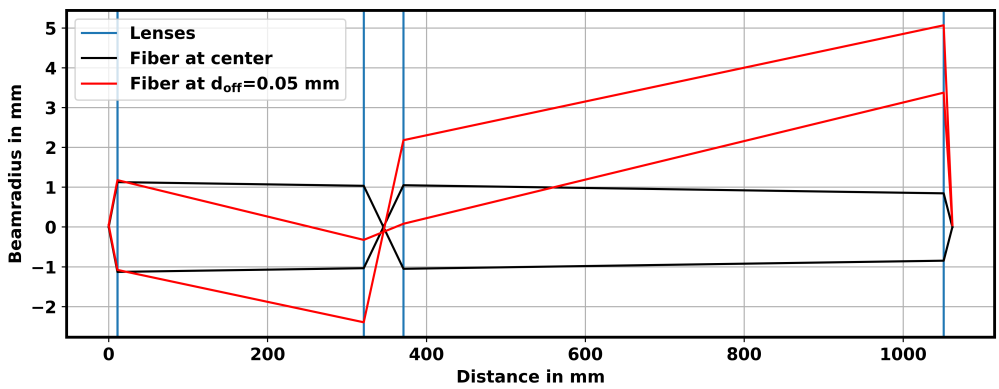

Figure 36: Ray transfer analysis: The (waist)rays emitted by single mode fiber (at position 0 along the x axis) are propagated through the optics system in place towards the HCF all the way to the right of the plot. The blue lines indicate the position of the lenses. Two sets of beams are displayed one (in black) for the fiber emitting the beam at zero displacement and the second (red) for a displacement of 50 μm.

emitted by a fiber that is displaced (along the y axis) by 50 μm. While the position of the focused red beam on the right is at the height of 50 μm as mentioned in chapter 4.2.1 the angle of incidence onto the HCF is extremely big and the coupling into the fiber will therefore decrease drastically.

To further visualize this, Fig.(37) depicts the angle of incidence at the HCF for different displacements of the single mode fiber.

For this graphic the ray transfer analysis from the previous figure has been repeated for different displacements of the SMF to gain the angle of incidence onto the HCF. The

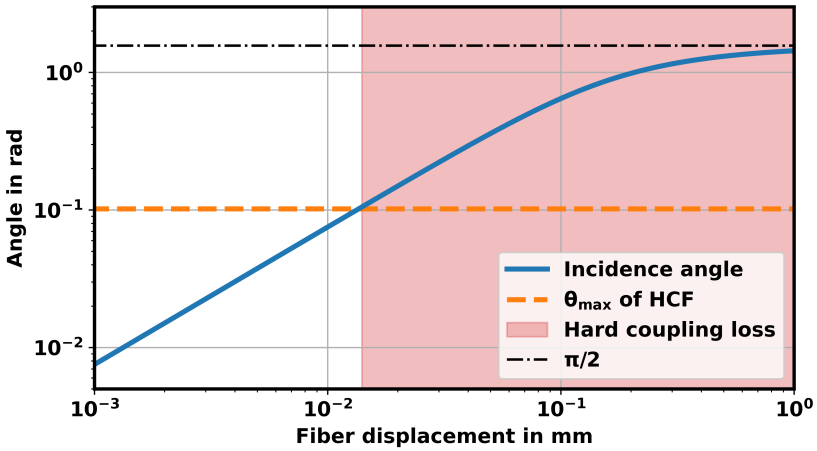

Figure 37: Allowed incidence angles: In blue the angle of incidence onto the HCF for different displacements of the single mode fiber is depicted. The orange dashed line shows the acceptance angle defined by the NA of the hollow core fiber. For displacements that result in a bigger angle of incidence than this, the coupling into the HCF will be severely impacted (red region).

dashed orange line shows the acceptance angle $\theta_{\max} = \arcsin(\mathrm{NA})$ of the hollow core fiber and the red area, starting at the intersection of the blue line and the dashed orange line, indicates the displacement regime where the angle of incidence starts to exceed $\theta_{\max}$. For our configuration this happens at a distance of $d_{\max} = 15\,\mu$m.
Looking back at Fig.(35) we can see that at a displacement of $\sim 15\,\mu$m from the (centrally aligned) zero position the maximal coupling already drops down to below half of its central value which fits well with the predictions from Fig.(37). Here it has to be noted that the values obtained for Fig.(35) will not exactly fit expected values because the normalization of the intensities did not take overall drifts of the laser power into account.

In order to overcome these problems the imaging system mapping the beam emitted by the SMF to the HCF has to be changed to a true 1 : 1 system. This is implemented by changing the arbitrarily placed 1 : 1 telescope in the beam path to a 4f configuration. In this setting the distance between the collimation lens L3 and L2 is exactly one focal length of L2 (denoted by f). L2 and L1 are separated by a distance of $2f$ and the distance between L1 and L0 is once again f. In this configuration the incidence angle of the beam from the SMF will (in theory) always be zero and thus re-coupling the maximum intensity should be possible for arbitrary displacements of the HCF.

After exchanging the lenses L1 and L2 for lenses of the appropriate focal length and position, the scans were re-done and the intensity distribution from Fig.(35) was repeated. Fig.(38) displays the updated intensities.

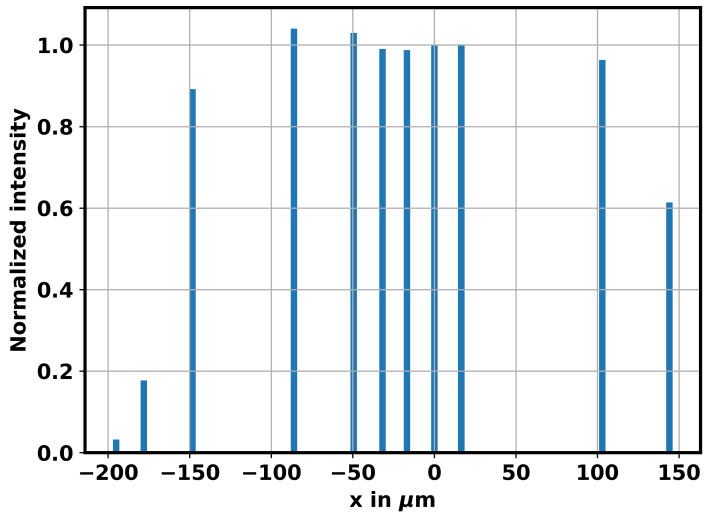

Figure 38: Maximal intensities for different Atto 1 positions in 4f configuration: The plot from Fig.(35) for the updated 4f optics system.

Here we see that the change in optics indeed resulted in wanted effect of an increased range of uniformity of coupled intensities, with respect to position of the HCF. After HCF displacements that are greater than 150 μm a sharp decrease is visible which implies that the built $4f$ system is not perfect. The most likely origin for this imperfection are not perfectly measured distances and a finite diameter of the lenses in the configuration. Nonetheless this increase in range is sufficient for our purpose. If bigger ranges have to be scanned a manual re-coupling through the mirrors outside the chamber can be performed.

4.2.5 Position mapping

With the increased range of possible scan positions the creation of the prediction mapping described in section 4.2.2 can now be performed. To do so Atto 1 (inner stage) was moved from its central position outwards in a spiral movement over a range of approximately $100 \times 100\,\mu$m. The resulting spiral with the (x_i^1, z_i^1) positions is shown in Fig.(39A). As can be seen there is a slight overlap of scan positions in the $+x$ direction which is attributed to the stages having different step sizes for different directions.
At each of the (x_i^1, z_i^1) position depicted in Fig.(39A) a scan by Atto 2 in the liking of Fig.(34) was performed and the center of the Gaussian intensity distribution was located through a two-dimensional fit. Fig.(39B) depicts the these (x_i^2, z_i^2) positions of Atto 2 with respect to each (x_i^1, z_i^1) Atto 1 positions along the spiral.
From these two sets of positions the first differences needed to calculate the matrix from Eq.(101) can be attained. Said matrix $\boldsymbol{A}$ is then acquired through a linear regression. The standard deviations corresponding to the matrix entries a_{ij} are summarized in the matrix $\boldsymbol{\sigma}$.

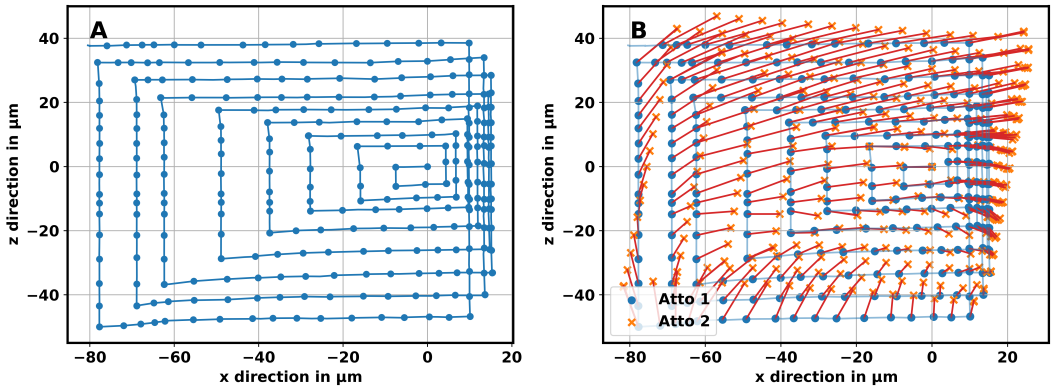

Figure 39: A) Stage 1 spiral: The spiral movement of Atto 1 performed to attain different scanning positions for Atto 2. **B) Mapping scans:** The position of Atto 2 where the intensity maximum was recovered for each Atto 1 position.

$$\boldsymbol{A} = \begin{pmatrix} 0.910 & 0.171 \\ -0.068 & 0.968 \end{pmatrix} \tag{102}$$

$$\boldsymbol{\sigma} = \begin{pmatrix} 0.015 & 0.005 \\ 0.007 & 0.020 \end{pmatrix} \tag{103}$$

Matrix $\boldsymbol{A}$ can be interpreted such that that a step of length $1\,\mu$m in the x-direction of Atto 1 results in $0.91\,\mu$m in the x-direction plus $-0.068\,\mu$m in the z-direction of Atto 2. As expected the matrix is not too far of the identity. The off diagonal elements suggest there is an angle between the movement axis of the translation stages.

4.2.6 Co-movement

Having retrieved the sensitivity matrix $\boldsymbol{A}$, the first test of the co-movement of the stages is started. In these first trials the stages were not moved simultaneously, but the inner stage (Atto 1) performed a leading step and the second outer stage (Atto 2) retrieves by first calculating the predicted step and then applying it. If the co-movement works correctly, the recorded intensity after every second step (recovery outer stage) should stay constant at the maximum coupling.

The motion of the inner stage was chosen to once again be a spiral depicted in Fig.(40A). The (recovering) motion performed by the outer stage is depicted in Fig.(40B) and the intensity recorded for every step is shown in Fig.(40C).
From Fig.(40B) one can immediately see that there are some issues with this process. The calculated mapping is linear and thus a spiral created by Atto 1 that does not overlap

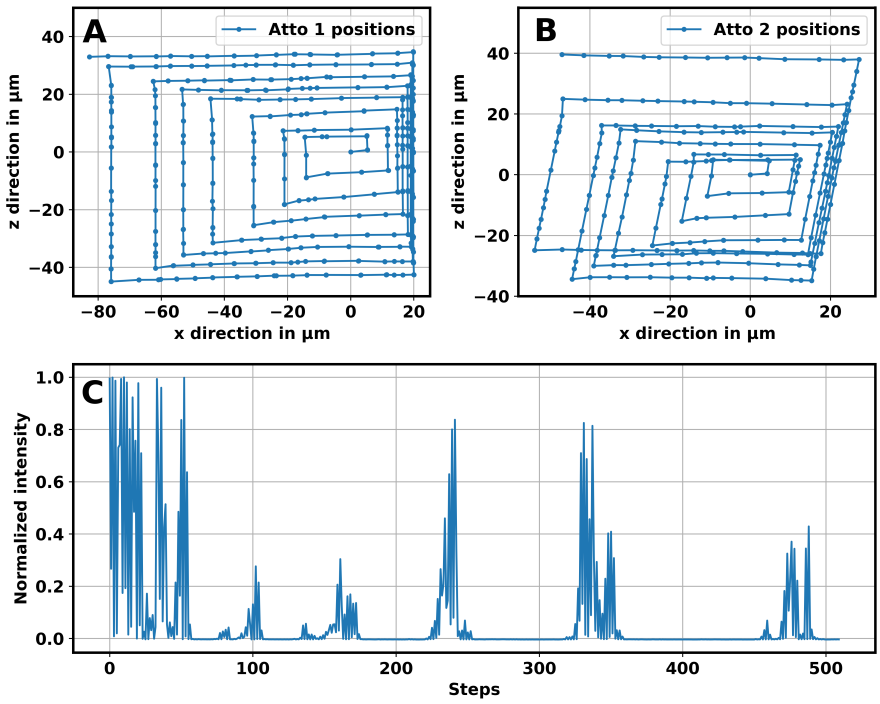

Figure 40: A) Spiral movement by Atto 1: The leading steps performed by the inner stage. **B) Recovering steps by Atto 2:** The movement of the outer stage according to the position mapping. It can be seen that this is not a clean motion as would be expected by the mapping being linear. **C) Recorded normalized intensity:** The intensity recorded along every step of this co-movement trial. It is visible that after the first couple of steps the intensity is lost and recovers for some steps to then decreases again.

(along the z-direction) should not yield any overlaps in the Atto 2 positions (also along z). The intensities displayed in Fig.(40C) further points towards an issue. For an optimal co-movement these normalized intensities should be high for all steps. Albeit not optimal, the first couple of steps performed by the stage match the predicted steps from the mapping closely. After ~ 70 steps the intensity is lost completely and then semi-periodically recovers for a brief window to fall off again shortly after.

To further showcase the problem at hand we look at Fig.(41A). In blue we see the positions that are predicted through the mapping dictated by the sensitivity matrix A from Eq.(102) applied on the Atto 1 positions. In orange we see the positions Atto 2 actually moved to (same as Fig.(40B)). For the central steps the positions overlap which explains why the intensity holds in the beginning but drops thereafter. This supports the claim that the movement commands sent to the stages do not lead to the expected positioning.

As to the semi-periodic recoveries of the intensity seen in Fig.(40C) we turn to Fig.(41B). The blue graph in this figure shows the differences between the predicted movement and the actual movement (in absolute values). The orange graph is the intensity recorded for each step. What can be seen here is that for the cases where the difference in these

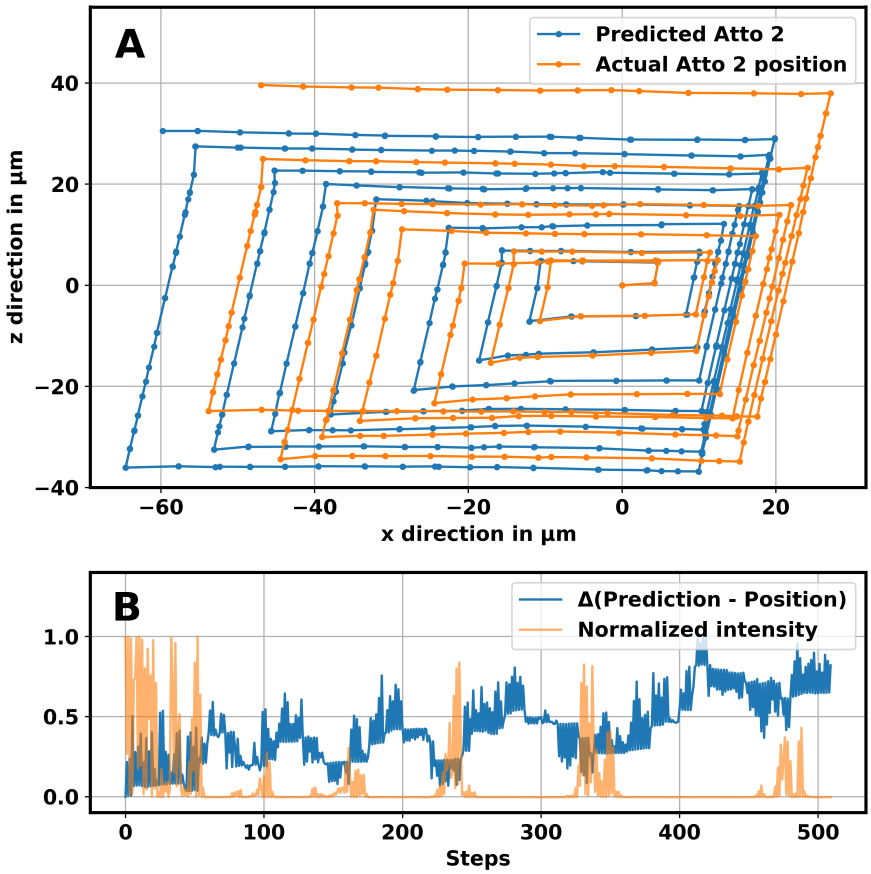

Figure 41: A) Discrepancy between the calculated predictions and the actual positions: In blue we display the predictions according to the mapping calculated through the sensitivity matrix $\boldsymbol{A}$ from Eq.(102) applied to the Atto 1 positions seen in Fig.(40A). In orange we see the actual positions Atto 2 moved to (same as Fig.(40B)). **B) Revivals of the intensities:** In blue we see the (normalized) differences between the calculated Atto 2 positions and the actual Atto 2 positions. In orange the intensity for every step is depicted (same as Fig.(40C))). When the differences between the predicted and actual positions are small the measured intensity slightly rises.

positions is small, the intensity slightly recovers which explains the revivals. While not being strong evidence, this could point towards the capability of the mapping to recover the intensity.

Next steps and potential improvements:

In order to be able to clearly argue for or against the ability of this mapping through first differences to recover the intensities as assumed, we have to find the problem in positioning. This issue is most likely found within the code for this leading and following movement. The control of the piezostages can at times be quite complex, due to a variety of different types of movements these devices can perform (see Wilfried Philips thesis [80]). Finding the correct mode of operation is often times a trial and error process. Once the

correct mode is found we can directly see how well the mapping holds the intensity over the movement and depending on this, we will determine the necessity of the recovering algorithm discussed in section 4.2.2.

A second previously discussed approach that will also be tested in the near future is the direct mapping discussed in section 4.2.2. As the calculation of the sensitivity matrix A already requires to find the direct mapping (see Fig.(39B)) this is a matter of writing a control algorithm that gradually moves through these optimal positions. A step wise intensity check in the manner of Fig.(40C) can be produced to confirm a constant coupling into the HCF. Once the basic principle of this is demonstrated with the wider step size of the scan from Fig.(39B)), a more narrow scan can be performed that will enable the movement to arbitrary positions within the scanned area, without the loss of coupling into the HCF.

Once the successful co-movement of the stages without loss of coupling is demonstrated, the first tests with nanoparticles in the HCF can commence. From there we use the "Scan and shoot" or the "Direct deposition" method to find the center of the standing wave target trap, completing the alignment of the hollow core fiber.

4.3 Electronic trigger

With the HCF aligned to the optical trap there is need for one additional update in the system. Namely a triggering mechanism to prevent the passage of the particle through the optical trap at pressures bellow the millibar regime.

4.3.1 Necessity for a triggering mechanism

As mentioned in section 2.2 the gradient force acting on a dielectric nanoparticle is a conservative force. Meaning in absence of any dissipative force, a particle will feel the same acceleration towards the trap center when entering the optical trap, as the deceleration towards the trap center upon leaving it. This is not a problem for the case of high gas pressures, as the drag exerted on the particle by the background gas upon entering the trap is enough to reduce the oscillator's kinetic energy to the point where the restoring force can keep it confined in the trap. This turns into a problem upon leaving the viscous flow regime, as the reduced gas damping is not enough to keep the particle inside the trap. In order to circumvent this problem we employ a triggering mechanism that only activates the optical trap we want to deliver the particle to, once the particle transverses its center. The tweezer is switched on and the particle is decelerated towards the trap center. Meaning that as long as the kinetic energy of the incoming particle does not exceed the height of the potential well the particle should be able to stay in the trap. Looking back at the stability criterion from Eq.(28) and the Fig.(8 & 10) one can see that a velocity of $v \approx 5\,\frac{\mathrm{mm}}{\mathrm{s}}$, results in a kinetic energy of $E_{\mathrm{kin}} \approx 0.01\,k_bT$. This is almost four orders of magnitude below the unstable regime in Fig.(8 & 10).
Fig.(42) shows the schematics of the three situations mentioned above. In Fig. (42A) the yellow background represents the presence of a background gas with gas damping γ. A particle with some initial velocity enters the optical potential and stays in the trap due to the damping provided by the gas. In part B there is no dissipative force present and the particle will just transverse the trap and leave it with the same velocity that it entered with. In part C the trap is only switched on once the particle arrives in the trap-center, thus feeling only an inward deceleration and therefore enable trapping.

4.3.2 Trigger principle

In order for the trigger to successfully keep the particle from shooting through the tweezer, the increase in trapping-intensity has to happen at a time the particle is positioned close to the trap center. To do so, the motion detection of the particle in the optical trap can be used in the following way:
If, in opposition to what has been shown in Fig.(42C), the trapping-intensity is not zero from the beginning but only very small, light will still reach the split detection. When

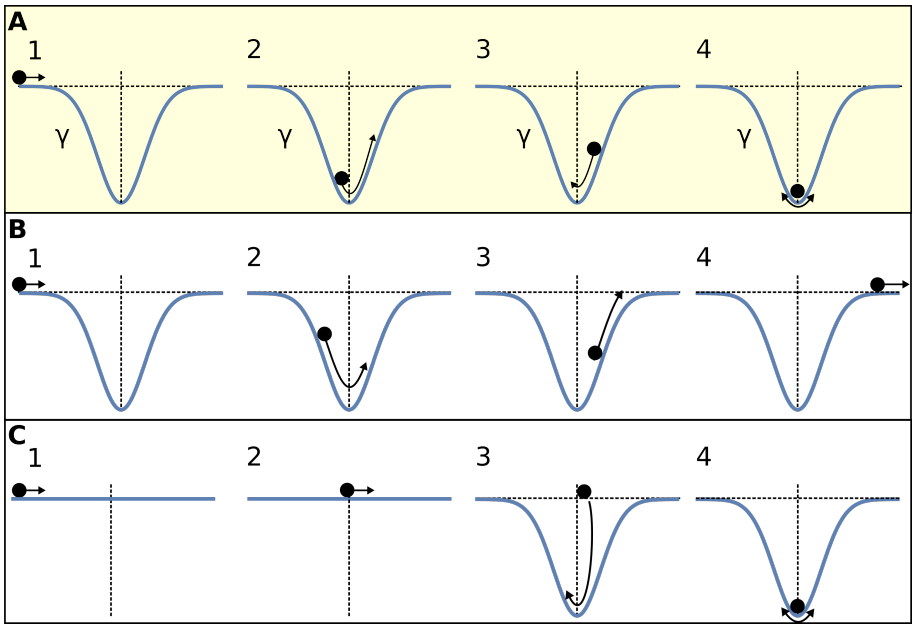

Figure 42: Handover cases: A) With background gas: A nanoparticle entering an optical trap with some initial velocity. The yellow shading signifies the presence of a background gas of damping γ. The gas damping introduces a friction term that dissipates the kinetic energy of the particle to a point where it is stably trapped in the optical potential. **B) No background gas:** No background gas is present and the particle is accelerated inwards towards the trap center with the same magnitude as it is decelerated inwards upon leaving the trap. Thus the particle keeps the initial velocity and is not confined by the trap. **C) With trigger mechanism:** The switching mechanism where the potential is only turned on once the particle transverses the trap center.

there is no particle in the optical trap, the detection signal will display a small voltage around zero with a variance given by the noisefloor of the detection. The moment the particle enters the shallow trap, it will begin to scatter more light into one, or the other half of the split detection. This in turn significantly increases signal variance. This increase can be used as a point in time at which (or shortly thereafter) the trap intensity has to be increased.

In order for an electronic circuit to notice this increase in variance, the following method to process the detection signal (schematically depicted in Fig.(43)) was devised.

With no particle in the trap, the signal recorded at the split detection has a very low voltage (orange line in graph A), which at first has to be amplified to more handy levels (blue signal). The time t_e is the time when the particle starts to scatter light from the trap into the detection. The signal is rectified (graph B). To smooth out the signal and get a clear increase at the time the variance rises, a lowpass-filter with a cutoff frequency of $\omega_{\text{cut}} \approx \Omega_z/50$, where Ω_z is the particle frequency in the axial direction, is applied (graph C). In the final step of the circuit a Schmidt-trigger or comparator with a tuneable setpoint is used to create the final TTL signal that is sent out to increase the trapping intensity.

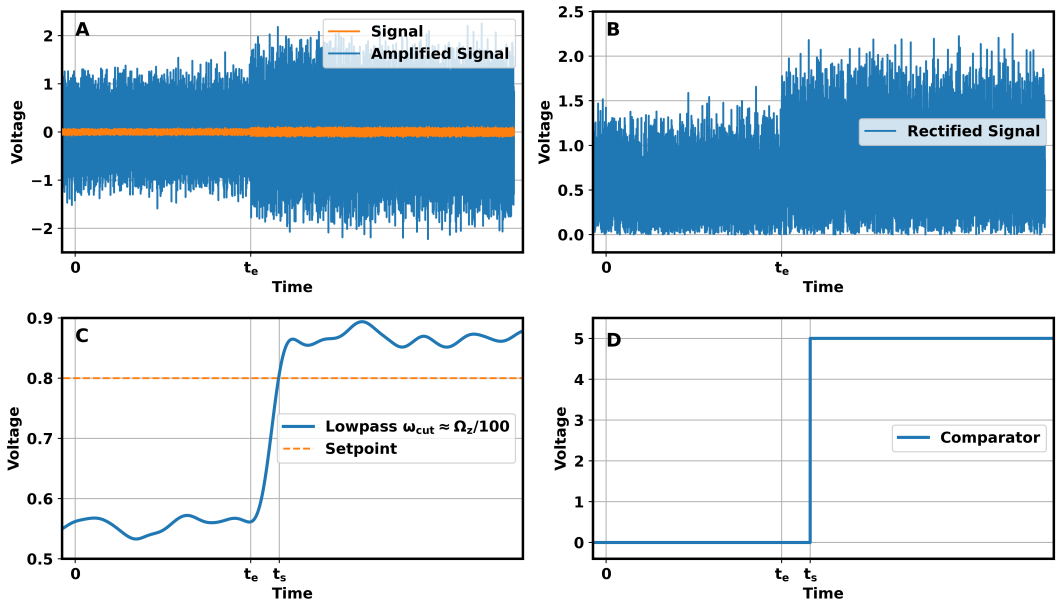

Figure 43: Trigger principle: Graphs **A)-D)** show the processing of a signal coming from the split detection to the trigger. The input signal has a small voltage which increases in variance at the "trap-entering" time t_e. In the first step the signal is amplified to simplify the following steps. The amplified signal is rectified, after which a lowpass-filter with a cutoff frequency in the range of $\omega_{\text{cut}} \approx \Omega_z/50$, where Ω_z is the particle frequency in the axial direction, is applied. Finally a comparator or Schmidt-trigger is applied to the filtered signal that gives out a TTL signal, given a certain setpoint is reached.

As can be seen in graph D, the time t_s at which the comparator "shoots" the high signal, is not the same as the entering time and has a certain delay $\delta_{\text{trig}} = t_e - t_s$. This delay is caused by different factors in the circuit design and will be discussed in the next section. Finally a short note on the choice of the cutoff frequency: a higher or lower cutoff could be chosen but at much higher cutoffs noise in the empty detection signal could make the trigger shoot randomly. In the same way a low cutoff frequency can make it difficult to choose the correct setpoint.

4.3.3 Circuit realization and testing

This section will discuss the realization of the circuit performing the signal-processing described in the previous chapter. Fig.(44) depicts the trigger circuit.
In a first step the small input signal V_{in} is amplified in the inverting operational amplifier circuit to the signal $V_1 = \frac{R_{\text{pot1}}}{R_1} V_{\text{in}}$. Next, this amplified signal passes through a rectifier as is described in [82]. In short, OP2 in combination with the two diodes acts as a one-way rectifier resulting in the voltage $V_2 = -V_1$ for the case of $V_1 \geq 0$ and to $V_2 = 0$ for the case of $V_2 \leq 0$. Ignoring the capacitance C making up the lowpass filter, the third operational amplifier is placed in as a regular amplifying circuit giving out $V_4 = -(V_1 + 2V_2)$. This

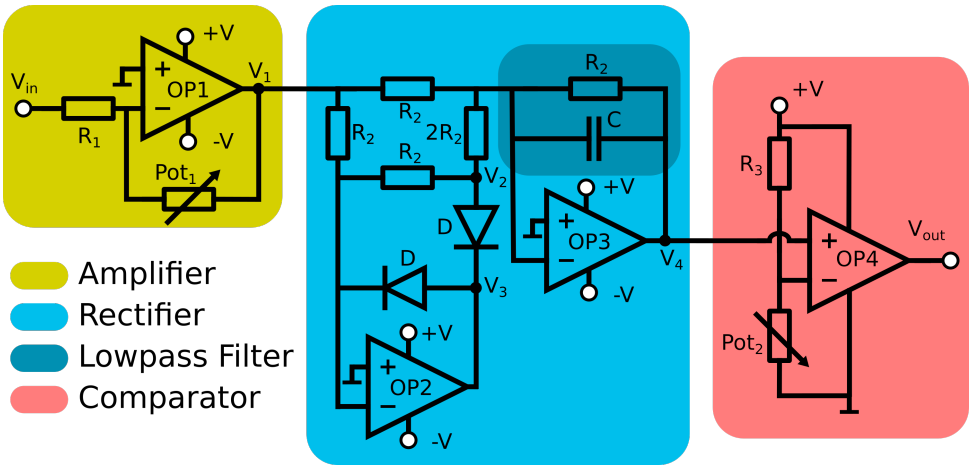

Figure 44: Trigger circuit: The trigger circuit consisting of the four steps discussed in the previous section. The input signal V_{in} is amplified in the first step by an inverting operational amplifier circuit. In the next step a rectifier consisting of two more operational amplifiers is implemented. By placing a resistor and a condenser in parallel to the second Op-Amp the output signal is lowpass filtered to the first order. In the final step a comparator consisting of a final Op-Amp is implemented. Its set-point is adjusted with another potentiometer. The output voltage $V_{\text{out}} = 0$ if the filtered signal does not rise above the setpoint. If it rises above the set value, the circuit outputs $V_{\text{out}} = +V$

gives:

$$V_4 = \begin{cases} V_1 & V_1 \geq 0 \\ -V_1 & V_1 \leq 0 \end{cases} \tag{104}$$

And thus rectifying the input signal. If now the capacitance C is added, V_4 is additionally first order lowpass filtered with a cutoff frequency of $\omega_{\text{cut}} = \frac{1}{R_2 C}$.
In the final step V_4 is connected to the last amplifier OP4 acting as a comparator. The ouput $V_{\text{out}} = 0$ as long as $V_4 \leq \frac{R_{\text{pot2}}}{R_3}(+V)$. If the voltage V_4 rises above this setpoint the output switches to $V_{\text{out}} = +V$ creating the desired output signal.

Functionality and internal delay testing

We initially tested the trigger with two different signals: a constructed "dummy-signal" and handover traces measured in the setup built for Jakob Riesers master thesis [16]. Fig.(45) shows the response of the trigger for these two types of test signals.
In Fig.(45A) a white noise signal followed by a sine like voltage with higher variance was chosen to test the circuit. With the setpoint at 15 mV the trigger gives out the expected 5 V signal once the variance switches above this value. In Fig.(45B) a recorded handover signal was chosen as test signal. This data of a transfer from hollow core fiber to an optical tweezer was performed at high pressures, with slow particle velocity and as can be seen, this data is already bandpass filtered. The particle falls into the trap at a $t_e = 1.3$ ms and

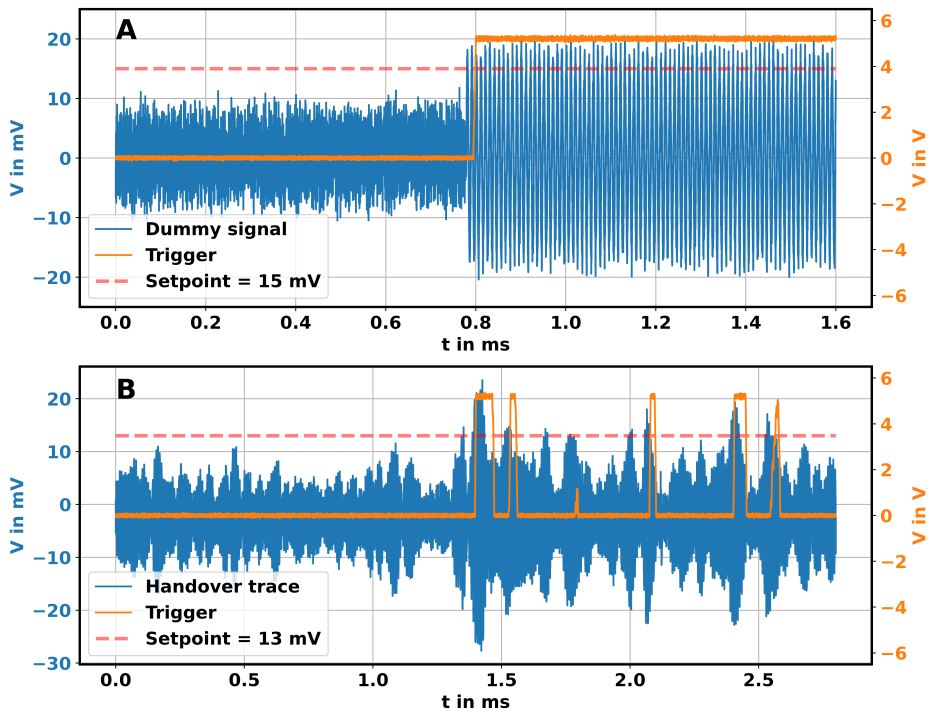

Figure 45: A) Dummy-signal: The "dummy-signal" made up of a white noise part with a low variance and a superposition of several sine-waves with a high variance was fed into the trigger. With a setpoint of 15 mV the response of the trigger is depicted. **B) Handover test signal:** An actual (bandpass-filtered) handover trace was fed into the trigger for testing. At about 1.3 ms the particle enters the trap here which is registered by the trigger.

the setpoint is fixed to 13 mV. Here it is visible that the output of the trigger falls back to 0 after a short time, as the variance decreases again.
Additionally to these test signals the functionality of the trigger was tested in a separate setup [16] with the following parameters: low laser power $P_1 = 200\,\mathrm{mW}$, high laser power $P_2 = 950\,\mathrm{mW}$ in an $\lambda = 1064\,\mathrm{nm}$ trap of waist $\omega_0 = 770\,\mathrm{nm}$. With the help of the trigger the lowest pressure at which handovers could be performed there was pushed from $p \approx 5\,\mathrm{mbar}$ to $p = 6.5 \cdot 10^{-2}\,\mathrm{mbar}$ which was the base pressure of the vacuum system in use.

The internal delay of the trigger was measured upon sending a rectangular signal into the circuit and monitoring the delay time after each component (differently colored regions in Fig.(44)). We found that almost all of the delay enters at the lowpass filter of first order. To precisely measure the delay of the whole circuit a rectangular signal of $f = 200\,\mathrm{kHz}$ was used as an input signal, a certain setpoint was defined and the time until the trigger rises is measured and reported in Fig.(46A) for three different cutoff frequencies.

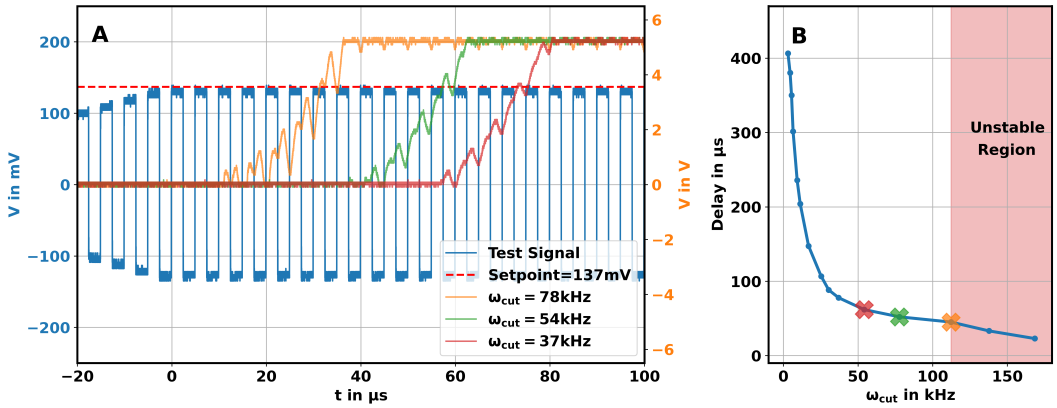

Figure 46: A) Trigger response: A rectangular input signal of 200 kHz frequency is fed into the trigger and the setpoint is fixed at 126 mV. The input signal variance is increased above the setpoint and the time until the trigger reaches its $5\,V$ output is measured for three different values of the cutoff frequency. **B) Internal delay:** The internal delay of the trigger for different cutoff frequencies. For cutoff frequencies in the "unstable regime" the averaging done by the lowpass filter of the trigger is so low, that the output is not stable anymore. The three colored crosses indicate the three trigger signals in graph **A**.

Fig.(46B) shows the internal delay for several cutoff frequencies. Here it is visible that a higher cutoff frequency results in a shorter internal delay. Increasing ω_{cut} ever higher to decrease the delay of the trigger is not possible: beyond a certain cutoff frequency the averaging done by the lowpass filter is not efficient anymore and the rectified signal is sent directly to the comparator. As this means random fluctuations are not smoothed anymore, the trigger will tend to output a signal when it is not supposed to. This behavior starts to appear for frequencies $\omega_{\text{cut}} > 110\,\text{kHz}$ and is indicated by the red region in graph B. This means, one has to find a sweet spot between short internal delays and stable trigger-outputs.

In order to figure out which delays are within the acceptable range to still perform a successful handover, we take a short look at the trapping geometry. In the optimal case the trigger raises the trap intensity in the exact moment the particle arrives in the trap center. If the trigger shoots too early and the particle is only on the outer edges of potential, it will feel the complete inwards acceleration and thus behave as if there was no trigger-mechanism at all. If the trigger shoots too late the particle will only see a reduced inwards deceleration, potentially too little to keep it in the trap. Assuming a trap waist of $\omega_{0t} = 1.15\,\mu\text{m}$ we can use the expression for the velocity of the particle in the standing wave, namely $v = \lambda\Delta/2$ to calculate the optimal delay, between the particle entering the trap and the power of the trap increasing, so that the nanoparticle is located closest to the trap center. Fig.(47) depicts these delay times for detunings from 1 Hz to 1 MHz.

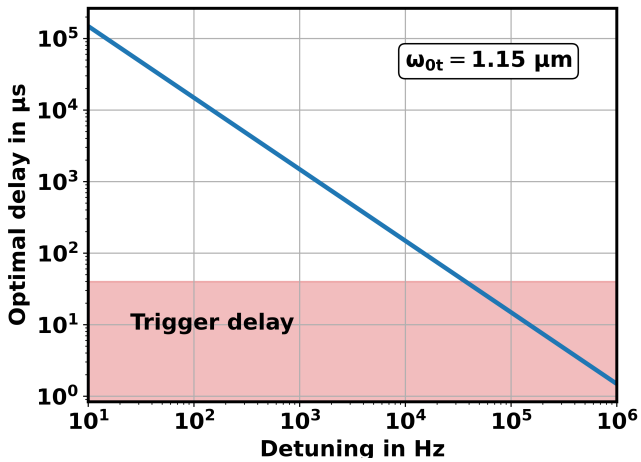

Figure 47: Optimal delay: The graph shows the optimal delay times between the particle being registered by the trigger and the trigger shooting/intensity increasing for a given detuning of the standing wave trap. These optimal times were calculated for a trap waist of $\omega_{0t} = 1.15\,\mu$m. The red area shows the minimal internal delay of the trigger and thus excludes optimal delays for detunings beyond $\sim 20\,$kHz.

From Fig.(46) we see that there is a minimal internal delay of the trigger circuit. Thus if a particle was to get to the trap center in a time shorter than this delay, the trap would not be able to snap at the optimal time. This is shown through the red area in Fig.(47) and means for this concrete case that handovers for detunings much bigger than $\Delta = 20\,$kHz will get less and less likely. At this point there is, however, no reason known why larger detunings should be necessary.

Integrating the trigger into the setup

Here we present the complete scheme to implement the trigger into the setup in order to not only control the increase in trapping power but also include timed parametric feedback cooling. Fig.(48) depicts the necessary components to accomplish these tasks.

Going through Fig.(48) from the left we see AOM1 and AOM2 (see Fig.(21)) creating the trapping and cooling beams. These two rays are recombined before the vacuum chamber with the experiment (here denoted by "setup"). The beams are monitored at a detector and its output signal is split in two. Starting with the line going into the trigger and ignoring the one going into the RedPitaya for now: when the particle enters the optical trap, the output signal of the detector shows an increase in variance. The output of the trigger signal is further sent into a TTL-input of a function generator which produces a stable 5 V when detecting a rising slope. In addition the signal can be arbitrarily delayed to optimize the timing according to the optimal delay. The signal is further sent to two switches. Switch 1 controls the magnitude of the RF-signal sent to AOM1 and switch 2 controls the RF-signal that is sent to AOM 2 to perform the parametric feedback cooling.

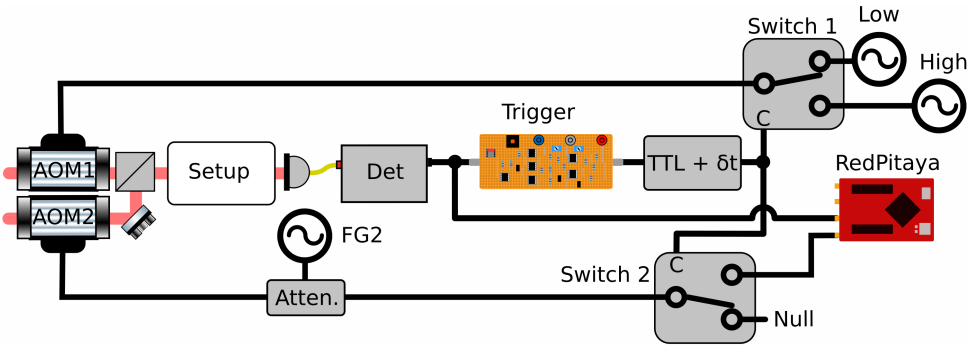

Figure 48: Trigger integration: In order to increase the intensity of the trapping beam, the acousto optic modulator (AOM 1) that creates the trapping beam is used. The increase in intensity is achieved by sending the signal from the trigger at first to a TTL-input of another function generator and then to an electronic switch 1. The switch will change the input of AOM 1 from low to high and by that increase the trap-depth. Additionally the TTL signal is sent to a second switch 2. This switch is used to start the modulation of the trapping intensity in order to cool the center of mass motion of the particle. The cooling signal itself is created by diverting a part of the detection into a "RedPitaya" FPGA. The ouput of switch 2 is sent into the modulation input of a variable attenuator which adjusts the RF signal driving AOM2 accordingly.

Upon a particle entering the trap the trigger shoots, creating the 5 V signal from the function generator. This in turn flips switch one, effectively increasing magnitude of the RF-signal being sent to AOM 1, and therefor increasing the trap depth. At switch 2 the flip will lead to the modulation created for the parametric feedback cooling in the RedPitaya to be sent to AOM 2.

4.4 A complete HCF loading recipe

The previous sections have established all the necessary components required to hand over a particle from a HCF into an optical trap located in a high or ultra high vacuum environment. Here a complete "recipe" from the situation where the HCF is not aligned to the optical trap, to a particle optically trapped at pressures in the UHV regime as we plan it is detailed. The process is divided into four steps:

1. **HCF pre-aligment:** The initial stage of pre-alignment is not performed through the methods described in section 4.2.1 but is performed by moving the HCF through the trap and monitoring the light scattered off it through a CCD camera sensitive at wavelengths around 1550 nm. This camera is placed on top of the vacuum chamber and looks down onto the experiment. The stage is moved along the $\pm x$ direction (for reference see Fig.(30)). By moving through the trapping beam in a constant velocity the approximate mid of this beam can be found through monitoring of the light scattered by the fibertip onto the CCD camera. Next the stage is moved in the $\pm z$ direction. At the left and right edges of this movement the fiber will once again pass through the trapping beam and scatter it. By middling between these positions an approximate center is located in the z-direction. Finally in the y-direction the fiber can approach the trap to the position just before light from the tweezer is scattered off it and the fiber would clip the beam. This concludes the initial positioning of the fiber.

2. **HCF alignment with co-moving stages:** The light from the reflected arm is re-coupled into the HCF using the mirrors and the telescope of the $4f$ configuration outside the chamber. Now the nebulizer is turned on and particles are slowly diffusing into the loading chamber by gently opening the vacuum valve. The detuning in one of the AOMs is turned to a typical value of $\Delta = 10\,\mathrm{kHz}$, giving particle velocities of $v = 5\,\mathrm{mm/s}$. Depending on the particle concentration in the isopropanol solution of the nebulizer, particles are pulled into the fiber at rates between 1-50 per minute. From here either the "scan and shoot" or the "direct deposition" method from chapter 4.2.1 can be used to scan an area around the pre-aligned position. Once the center of the trap is found the next step can commence.

3. **Initial high pressure handovers:** Having the fiber now positioned to the trap, the initial handover tests can commence. For the first handovers performed after a new alignment run, the vacuum system is not immediately at UHV conditions but in a regime where feedback cooling is not yet necessary ($> 10^{-1}\,\mathrm{mbar}$). Here the trigger and the connected electronics are switched on as described in the previous section

(see Fig.(48)). Setting a delay of the TTL-output according to the chosen detuning is necessary. At this point nanoparticles are once again diffused into the loading chamber from the nebulizer, the detuning is turned to the chosen value and the particles begin to be trapped in and move up the HCF. When the particle exits the HCF and moves into $\lambda = 1550\,\mathrm{nm}$ standing wave trap, the detection signal increases in variance, the trigger picks this up and the process described in the previous section sans the parametric feedback cooling activated by switch 2 takes place. If the handover is successful, the detuning in the HCF standing wave is reversed, the fiber is emptied of particles and the light through the fiber is either blocked or turned off. If on the other hand no particle was trapped, the TTL-output is reset and the next attempt is started.

4. **Low pressure handovers:** Once a particle is trapped in the $\lambda = 1550\,\mathrm{nm}$ standing wave and the HCF light is turned off, the parametric feedback cooling is started and the pressure in the chamber is reduced. A pumpdown from $10^{-2}\,\mathrm{mbar}$ to $< 10^{-9}\,\mathrm{mbar}$ will take up to days, which is why the alignment should not be altered anymore afterwards as this would require a redo of the previous steps. As the bakeout of the chamber happens even before the first step we expect no change in alignment during the pumpdown. Once the base pressure is reached, all the system parameters are fixed and the setup is ready for direct loading into UHV. The particle currently in the trap can be removed and the previous steps are repeated, with the adjustment that switch 2 is connected this time. Thus when a particle enters the trap, not only does the intensity increase but the parametric feedback is activated.

This method establishes a clean, and deterministic way to enable optical levitation in UHV conditions that additionally is also very fast, with the longest process being the particle traversing the HCF lasting for about 3 minutes.

5 Conclusion and outlook

During the course of this thesis, we have described initial steps in the implementation of a new experimental setup that is designed maximize the coherence times of levitated nanoparticles. Specifically, it aims to meet the requirements of an envisioned interference experiment with nanoparticles of mass 10^9 amu in a non-cryogenic tabletop environment. We focused in particular on two technical aspects that are highly relevant for enabling the experimental realization of this ambitious project:

1. **Standing wave trap and detection:** A $\lambda = 1550\,\text{nm}$ standing wave optical trap located in an ultra high vacuum compatible chamber was set up. Additionally a sophisticated detection scheme using a Sagnac interferometer to filter the high-information bearing photons, back-scattered by the particle, from the rest of the light, was conceived, set up and aligned. The extinction ratio of the interferometer was measured to be in order of $4 \cdot 10^3$. We estimate that an increase of this ratio by one or two orders of magnitude will enable groundstate cooling of the nanoparticle motion along the detected degree of freedom.

2. **Nanoparticle loading at UHV:** We use the already established method of loading nanoparticles into optical traps using hollow core fibers [16] and further extend it for usage in ultra high vacuum environments. Specifically we developed two new methods:

   (a) **HCF alignment:** In order to align the HCF to the target optical trap we devised a novel approach using co-moving piezo-stages. These circumvent the need for an a priori particle in the trap as was required in the previous version of the HCF-loading method and therefor extend its range of usage into the UHV regime.

   (b) **Electronic trigger:** A triggering mechanism increasing the optical trap depth upon a particle entering the standing wave trap was developed. This is required as at pressures below the viscous flow regime the drag force exerted onto the particle by the background gas is not strong enough to prevent it from traversing the trap upon handover from the HCF.

   Both of these methods are described in detail and preliminary results are presented.

Currently the co-movement of the piezo-stages is not yet fully operational. There is still a prevailing issue concerning the application of the calculated mapping. As of this moment, the plan as described in section 4.2.6 to either find the issue in the current mapping or roll back one step towards the direct mapping, is in motion. Once the basic functionality

of the motion according to either of the mappings is demonstrated, a finer map can be produced to enable the movement of the stages to arbitrary positions within the scanned areas, without the loss of coupling into the HCF.
The next step from there is to demonstrate the ability to find the $\lambda = 1550\,\mathrm{nm}$ trap through either the "Scan and shoot" or "Direct deposition" method. Being able to position the HCF correctly with respect to the optical trap will allow the first handover trials as described in the recipe presented in the last chapter of the thesis to commence.

Once this loading mechanism is completely operational and one can reliably transfer particles at ultra high vacuum conditions the big roadblock hindering the access to coherence times of the particle wavepacket going towards $10^2\,\mathrm{ms}$ is removed. From there on, the next challenges on the way towards the fully functioning matter-wave interferometry experiment for dielectric nanoparticles of masses above $10^9\,\mathrm{amu}$ can be approached.

References

[1] E. Schrödinger. Die gegenwärtige Situation in der Quantenmechanik. *Die Naturwissenschaften*, 23(48):807–812, 1935. doi: 10.1007/BF01491891.

[2] C. Davisson and L. Germer. Reflection of electrons by a crystal of nickel. pages 317–322, 1928.

[3] M. Arndt, O. Nairz, J. Vos-andreae, C. Keller, G. V. D. Zouw, and A. Zeilinger. Wave – particle duality of C 60 molecules. *Nature*, 401(October):680–682, 1999.

[4] Y. Y. Fein, P. Geyer, P. Zwick, F. Kiałka, S. Pedalino, M. Mayor, S. Gerlich, and M. Arndt. Quantum superposition of molecules beyond 25 kDa. *Nature Physics*, 15 (12):1242–1245, 2019. doi: 10.1038/s41567-019-0663-9.

[5] H. Pino, J. Prat-Camps, K. Sinha, B. P. Venkatesh, and O. . Romero-Isart. On-chip quantum interference of a superconducting microsphere. *Quantum Science and Technology*, 3(2), 2018. doi: 10.1088/2058-9565/aa9d15.

[6] A. Bassi, K. Lochan, S. Satin, T. P. Singh, and H. Ulbricht. Models of wave-function collapse, underlying theories, and experimental tests. *Reviews of Modern Physics*, 85 (2):471–527, 2013. doi: 10.1103/RevModPhys.85.471.

[7] U. Delić, M. Reisenbauer, K. Dare, D. Grass, V. Vuletić, N. Kiesel, and M. Aspelmeyer. Cooling of a levitated nanoparticle to the motional quantum ground state. *Science*, 367(6480):892–895, 2020. doi: 10.1126/science.aba3993.

[8] L. Magrini, P. Rosenzweig, C. Bach, A. Deutschmann-Olek, S. G. Hofer, S. Hong, N. Kiesel, A. Kugi, and M. Aspelmeyer. Optimal quantum control of mechanical motion at room temperature: ground-state cooling. 2020. URL `http://arxiv.org/abs/2012.15188`.

[9] F. Tebbenjohanns, M. L. Mattana, M. Rossi, M. Frimmer, and L. Novotny. Quantum control of a nanoparticle optically levitated in cryogenic free space. 2021. URL `http://arxiv.org/abs/2103.03853`.

[10] O. Romero-Isart, A. C. Pflanzer, F. Blaser, R. Kaltenbaek, N. Kiesel, M. Aspelmeyer, and J. I. Cirac. Large quantum superpositions and interference of massive nanometer-sized objects. *Physical Review Letters*, 107(2):2–5, 2011. doi: 10.1103/PhysRevLett.107.020405.

[11] R. Kaltenbaek, G. Hechenblaikner, N. Kiesel, O. Romero-Isart, K. C. Schwab, U. Johann, and M. Aspelmeyer. Macroscopic quantum resonators (MAQRO): Testing

quantum and gravitational physics with massive mechanical resonators. *Experimental Astronomy*, 34(2):123–164, 2012. doi: 10.1007/s10686-012-9292-3.

[12] M. Scala, M. S. Kim, G. W. Morley, P. F. Barker, and S. Bose. Matter-wave interferometry of a levitated thermal nano-oscillator induced and probed by a spin. *Physical Review Letters*, 111(18):2–6, 2013. doi: 10.1103/PhysRevLett.111.180403.

[13] J. Bateman, S. Nimmrichter, K. Hornberger, and H. Ulbricht. Near-field interferometry of a free-falling nanoparticle from a point-like source. *Nature Communications*, 5:1–5, 2014. doi: 10.1038/ncomms5788.

[14] O. Romero-Isart. Coherent inflation for large quantum superpositions of levitated microspheres. *New Journal of Physics*, 19(12):1–5, 2017. doi: 10.1088/1367-2630/aa99bf.

[15] E. Joos and H. D. Zeh. The emergence of classical properties through interaction with the environment. *Zeitschrift für Physik B Condensed Matter*, 59(2):223–243, 1985. doi: 10.1007/BF01725541.

[16] J. Rieser. *Towards Optical Levitation in UHV : Loading using Hollow-Core Photonic Crystal Fibers.* Master thesis, University of Vienna, 2020.

[17] S. Nimmrichter, K. Hornberger, P. Haslinger, and M. Arndt. Testing spontaneous localization theories with matter-wave interferometry. pages 8–12, 2018.

[18] L. V. de Broglie. *On the Theory of Quanta.* PhD thesis, 1924.

[19] D. W. Keith, C. R. Ekstrom, Q. A. Turchette, and D. E. Pritchard. An Interferometer for Atoms. *Physical Review Letters*, 66(21):2693–2697, 1991.

[20] M. Kasevich and S. Chu. Atomic Interferometry Using Stimulated Raman Transitions. *Physical Review Letters*, 67(2):2–5, 1991.

[21] S. Nimmrichter. *Macroscopic Matter-wave Interferometry.* Dissertation, Universtität Wien, 2013.

[22] R. Kaltenbaek, M. Aspelmeyer, P. F. Barker, A. Bassi, and Others. Macroscopic quantum resonators (MAQRO): 2015 update. *EPJ Quantum Technology*, 3(1):1–38, 2016. doi: 10.1140/epjqt/s40507-016-0043-7.

[23] L. Neumaier. Private communication, publication in preparation. 2021.

[24] T. P. Purdy, R. W. Peterson, and C. A. Regal. Observation of radiation pressure shot noise on a macroscopic object. *Science*, 339(6121):801–804, 2013. doi: 10.1126/science.1231282.

[25] V. Jain, J. Gieseler, C. Moritz, C. Dellago, R. Quidant, and L. Novotny. Direct Measurement of Photon Recoil from a Levitated Nanoparticle. *Physical Review Letters*, 116(24):1–5, 2016. doi: 10.1103/PhysRevLett.116.243601.

[26] D. E. Chang, C. A. Regal, S. B. Papp, D. J. Wilson, J. Ye, O. Painter, H. J. Kimble, and P. Zoller. Cavity opto-mechanics using an optically levitated nanosphere. *Proceedings of the National Academy of Sciences of the United States of America*, 107 (3):1005–1010, 2010. doi: 10.1073/pnas.0912969107.

[27] M. Wutz, H. Adam, W. Walcher, and K. Jousten. *Handbuch der Vakumtechnik*. vieweg, 7 edition, 2000. ISBN 9783322999481.

[28] P. Manini. Non Evaporable Getter (NEG) pumps: A route to UHV-XHV. *AIP Conference Proceedings*, 1149(August 2009):1138–1142, 2009. doi: 10.1063/1.3215608.

[29] A. Ashkin and J. M. Dziedzic. Optical levitation by radiation pressure. *Applied Physics Letters*, 19(8):283–285, 1971. doi: 10.1063/1.1653919.

[30] A. Ashkin and J. M. Dziedzic. Optical levitation in high vacuum. *Applied Physics Letters*, 28(6):333–335, 1976. doi: 10.1063/1.88748.

[31] J. Gieseler, B. Deutsch, R. Quidant, and L. Novotny. Subkelvin parametric feedback cooling of a laser-trapped nanoparticle. *Physical Review Letters*, 109(10):1–5, 2012. doi: 10.1103/PhysRevLett.109.103603.

[32] N. Kiesel, F. Blaser, U. Delić, D. Grass, R. Kaltenbaek, and M. Aspelmeyer. Cavity cooling of an optically levitated submicron particle. *Proceedings of the National Academy of Sciences of the United States of America*, 110(35):14180–14185, 2013. doi: 10.1073/pnas.1309167110.

[33] P. Asenbaum, S. Kuhn, S. Nimmrichter, U. Sezer, and M. Arndt. Cavity cooling of free silicon nanoparticles in high vacuum. *Nature Communications*, 4:1–7, 2013. doi: 10.1038/ncomms3743.

[34] G. Ranjit, M. Cunningham, K. Casey, and A. A. Geraci. Zeptonewton force sensing with nanospheres in an optical lattice. *Physical Review A*, 93(5):1–5, 2016. doi: 10.1103/PhysRevA.93.053801.

[35] F. Tebbenjohanns, M. Frimmer, A. Militaru, V. Jain, and L. Novotny. Cold Damping of an Optically Levitated Nanoparticle to Microkelvin Temperatures. *Physical Review Letters*, 122(22):223601, 2019. doi: 10.1103/PhysRevLett.122.223601.

[36] M. D. Summers, D. R. Burnham, and D. McGloin. Trapping solid aerosols with optical tweezers: A comparison between gas and liquid phase optical traps. *Optics Express*, 16(11):7739, 2008. doi: 10.1364/oe.16.007739.

[37] J. Vovrosh, M. Rashid, D. Hempston, J. Bateman, M. Paternostro, and H. Ulbricht. Parametric feedback cooling of levitated optomechanics in a parabolic mirror trap. *Journal of the Optical Society of America B*, 34(7):1421, 2017. doi: 10.1364/josab.34.001421.

[38] P. Mestres, J. Berthelot, M. Spasenović, J. Gieseler, L. Novotny, and R. Quidant. Cooling and manipulation of a levitated nanoparticle with an optical fiber trap. *Applied Physics Letters*, 107(15), 2015. doi: 10.1063/1.4933180.

[39] D. P. Atherton. *Sensitive Force Measurements With Optically Trapped Micro-Spheres in High Vacuum.* PhD thesis, University of Nevada, Reno, 2015.

[40] D. S. Bykov, P. Mestres, L. Dania, L. Schmöger, and T. E. Northup. Direct loading of nanoparticles under high vacuum into a Paul trap for levitodynamical experiments. *Applied Physics Letters*, 115(3):3–7, 2019. doi: 10.1063/1.5109645.

[41] J. Gieseler. *Dynamics of optically levitated nanoparticles in high vacuum.* PhD thesis, ICFO – The Institute of Photonic Sciences, 2014.

[42] D. Grass. *Levitated optomechanics in vacuum using hollow core photonic crystal fibers and optical cavities.* PhD thesis, 2018.

[43] L. Novotny and B. Hecht. *Principles of nano-optics*, volume 9781107005. 2009. ISBN 9780511794193. doi: 10.1017/CBO9780511794193.

[44] A. Jona and P. Zema. Light at work : The use of optical forces for particle manipulation , sorting , and analysis. pages 4813–4851, 2008. doi: 10.1002/elps.200800484.

[45] A. Ashkin, J. M. Dziedzic, J. E. Bjorkholm, and S. Chu. Observation of a single-beam gradient force optical trap for dielectric particles. In *Optical Angular Momentum*, volume 11, pages 196–198. 2016. ISBN 9781482269017. doi: 10.1364/ol.11.000288.

[46] Y. Harada. Radiation forces on a dielectric sphere in the Rayleigh scattering regime. *Optics communications*, 124(March):529–541, 1996.

[47] S. A. Beresnev, V. G. Chernyak, and G. A. Fomyagin. Motion of a spherical particle in a rarefied gas. Part 2. Drag and thermal polarization. *Journal of Fluid Mechanics*, 219(March 2014):405–421, 1990. doi: 10.1017/S0022112090003007.

[48] U. Delić. *Cavity cooling by coherent scattering of a levitated nanosphere in vacuum.* PhD thesis, 2019.

[49] M. Gehm, P. J. Isackson, and M. Blaber. Dynamics of noise-induced heating in atom trap. *Biochemistry*, 58(5), 1998. doi: 10.1021/bi00395a025.

[50] J. Millen, T. Deesuwan, P. Barker, and J. Anders. Nanoscale temperature measurements using non-equilibrium Brownian dynamics of a levitated nanosphere. *Nature Nanotechnology*, 9(6):425–429, 2014. doi: 10.1038/nnano.2014.82.

[51] E. Hebestreit, M. Frimmer, R. Reimann, C. Dellago, F. Ricci, and L. Novotny. Calibration and energy measurement of optically levitated nanoparticle sensors. *Review of Scientific Instruments*, 89(3), 2018. doi: 10.1063/1.5017119.

[52] D. Grass, J. Fesel, S. G. Hofer, N. Kiesel, and M. Aspelmeyer. Optical trapping and control of nanoparticles inside evacuated hollow core photonic crystal fibers. *Applied Physics Letters*, 108(22), 2016. doi: 10.1063/1.4953025.

[53] T. S. Monteiro, J. Millen, G. A. Pender, F. Marquardt, D. Chang, and P. F. Barker. Dynamics of levitated nanospheres: Towards the strong coupling regime. *New Journal of Physics*, 15, 2013. doi: 10.1088/1367-2630/15/1/015001.

[54] M. Poggio, C. L. Degen, H. J. Mamin, and D. Rugar. Feedback cooling of a cantilever's fundamental mode below 5 mK. *Physical Review Letters*, 99(1):1–4, 2007. doi: 10.1103/PhysRevLett.99.017201.

[55] T. W. Penny, A. Pontin, and P. F. Barker. Performance and limits of feedback cooling methods for levitated oscillators: a direct comparison. (1):1–11, 2021.

[56] J. Liao, M. Jost, M. Schaffner, and Others. FPGA Implementation of a Kalman-Based Motion Estimator for Levitated Nanoparticles. *IEEE Transactions on Instrumentation and Measurement*, 68(7):2374–2386, 2019. doi: 10.1109/TIM.2018.2879146.

[57] J. M. Courty, A. Heidmaim, and M. Pinard. Quantum limits of cold damping with optomechanical coupling. *European Physical Journal D*, 17(3):399–408, 2001. doi: 10.1007/s100530170014.

[58] M. Rossi, D. Mason, J. Chen, Y. Tsaturyan, and A. Schliesser. Measurement-based quantum control of mechanical motion. *Nature*, 563(7729):53–58, 2018. doi: 10.1038/s41586-018-0643-8.

[59] J. D. Jackson. Classical Electrodynamics, 1998.

[60] H. Tanji-Suzuki, I. D. Leroux, M. H. Schleier-Smith, M. Cetina, A. T. Grier, J. Simon, and V. Vuletić. Interaction between Atomic Ensembles and Optical Resonators. Classical Description. *Advances in Atomic, Molecular and Optical Physics*, 60(November 2011):201–237, 2011. doi: 10.1016/B978-0-12-385508-4.00004-8.

[61] F. Tebbenjohanns, M. Frimmer, and L. Novotny. Optimal position detection of a dipolar scatterer in a focused field. *Physical Review A*, 100(4):1–10, 2019. doi: 10.1103/PhysRevA.100.043821.

[62] T. Seberson and F. Robicheaux. Distribution of laser shot-noise energy delivered to a levitated nanoparticle. *Physical Review A*, 102(3):33505, 2020. doi: 10.1103/PhysRevA.102.033505.

[63] F. Tebbenjohanns, M. Frimmer, V. Jain, D. Windey, and L. Novotny. Motional Sideband Asymmetry of a Nanoparticle Optically Levitated in Free Space. *Physical Review Letters*, 124(1), 2020. doi: 10.1103/PhysRevLett.124.013603.

[64] K. Yamamoto, D. Friedrich, T. Westphal, S. Goßler, K. Danzmann, K. Somiya, S. L. Danilishin, and R. Schnabel. Quantum noise of a Michelson-Sagnac interferometer with a translucent mechanical oscillator. *Physical Review A - Atomic, Molecular, and Optical Physics*, 81(3):1–6, 2010. doi: 10.1103/PhysRevA.81.033849.

[65] D. Friedrich, H. Kaufer, T. Westphal, K. Yamamoto, A. Sawadsky, F. Ya Khalili, S. L. Danilishin, S. Goßler, K. Danzmann, and R. Schnabel. Laser interferometry with translucent and absorbing mechanical oscillators. *New Journal of Physics*, 13, 2011. doi: 10.1088/1367-2630/13/9/093017.

[66] M. A. Taylor, J. Knittel, M. T. Hsu, H. A. Bachor, and W. P. Bowen. Sagnac interferometer-enhanced particle tracking in optical tweezers. *Journal of Optics*, 13 (4), 2011. doi: 10.1088/2040-8978/13/4/044014.

[67] M. Reisenbauer. *Dissipative Optomechanics on a Levitated Microresonator*. Master thesis, 2018.

[68] A. N. Vamivakas, S. B. Ippolito, A. K. Swan, M. S. Ünlü, M. Dogan, E. R. Behringer, and B. B. Goldberg. Phase-sensitive detection of dipole radiation in a fiber-based high numerical aperture optical system. *Optics Letters*, 32(8):970, 2007. doi: 10.1364/ol.32.000970.

[69] C. Bach. *Detection of a levitated particle ' s mechanical motion close to the Heisenberg limit*. Masters thesis, 2021.

[70] J. A. Buck and I. Jacobs. Fundamentals of Optical Fibers . *Physics Today*, 1996. doi: 10.1063/1.2807510.

[71] P. S. J. Russell. Photonic-Crystal Fibers. *Journal of lightwave technology*, 24(12): 4729–4749, 2006.

[72] R. F. Cregan, B. J. Mangan, J. C. Knight, T. A. Birks, P. S. J. Russell, P. J. Roberts, and D. C. Allan. Single-mode photonic band gap guidance of light in air. *Science*, 285(5433):1537–1539, 1999. doi: 10.1126/science.285.5433.1537.

[73] T. Takekoshi and R. J. Knize. Optical guiding of atoms through a hollow-core photonic band-gap fiber. *Physical Review Letters*, 98(21):3–6, 2007. doi: 10.1103/PhysRevLett.98.210404.

[74] C. A. Christensen, S. Will, M. Saba, G. B. Jo, Y. I. Shin, W. Ketterle, and D. Pritchard. Trapping of ultracold atoms in a hollow-core photonic crystal fiber. *Physical Review A - Atomic, Molecular, and Optical Physics*, 78(3):1–4, 2008. doi: 10.1103/PhysRevA.78.033429.

[75] F. Benabid, J. C. Knight, and P. S. J. Russell. Particle guidance in hollow-core photonic crystal fiber. *Pacific Rim Conference on Lasers and Electro-Optics, CLEO - Technical Digest*, 10(21):48–49, 2002. doi: 10.1109/cleo.2002.1033416.

[76] O. A. Schmidt, T. G. Euser, and P. S. Russell. Mode-based microparticle conveyor belt in air-filled hollow-core photonic crystal fiber. *Optics Express*, 21(24):29383, 2013. doi: 10.1364/oe.21.029383.

[77] A. Ermolov, K. F. Mak, F. Tani, P. Hölzer, J. C. Travers, and P. S. J. Russell. Low loss hollow optical-waveguide connection from atmospheric pressure to ultra-high vacuum. *Applied Physics Letters*, 103(26), 2013. doi: 10.1063/1.4860947.

[78] E. A. Marcatili and R. A. Schmeltzer. Hollow Metallic and Dielectric Waveguides for Long Distance Optical Transmission and Lasers. *Bell System Technical Journal*, 43 (4):1783–1809, 1964. doi: 10.1002/j.1538-7305.1964.tb04108.x.

[79] R. Brüning, Y. Zhang, M. McLaren, M. Duparré, and A. Forbes. Overlap relation between free-space Laguerre Gaussian modes and step-index fiber modes. *Journal of the Optical Society of America A*, 32(9):1678, 2015. doi: 10.1364/josaa.32.001678.

[80] W. Philipp. *Trapping and Positioning of Nanoparticles in a UHV environment submitted.* Bachelor's thesis, 2011.

[81] M. Debiossac, D. Grass, J. J. Alonso, E. Lutz, and N. Kiesel. Thermodynamics of continuous non-Markovian feedback control. *Nature Communications*, 11(1):1–6, 2020. doi: 10.1038/s41467-020-15148-5.

[82] U. Tietze and C. Schenk. *Halbleiter-Schaltungstechnik.* 1999. ISBN 9783662119402. doi: 10.1007/978-3-662-11939-6.